INFORMATION TO USERS

This manuscript has been reproduced from the microfilm master. UMI films the text directly from the original or copy submitted. Thus, some thesis and dissertation copies are in typewriter face, while others may be from any type of computer printer.

The quality of this reproduction is dependent upon the quality of the copy submitted. Broken or indistinct print, colored or poor quality illustrations and photographs, print bleedthrough, substandard margins, and improper alignment can adversely affect reproduction.

In the unlikely event that the author did not send UMI a complete manuscript and there are missing pages, these will be noted. Also, if unauthorized copyright material had to be removed, a note will indicate the deletion.

Oversize materials (e.g., maps, drawings, charts) are reproduced by sectioning the original, beginning at the upper left-hand corner and continuing from left to right in equal sections with small overlaps.

Photographs included in the original manuscript have been reproduced xerographically in this copy. Higher quality 6" x 9" black and white photographic prints are available for any photographs or illustrations appearing in this copy for an additional charge. Contact UMI directly to order.

Bell & Howell Information and Learning
300 North Zeeb Road, Ann Arbor, MI 48106-1346 USA
800-521-0600

Université d'Ottawa · University of Ottawa

Bose-Einstein Condensation of Excitons

by Eric Benson

Thesis submitted to the
Faculty of Graduate Studies and Research
in partial fulfillment of the requirements
of the Doctorate in Physics

Department of Physics
University of Ottawa
150 Louis Pasteur
Ottawa, Ontario
K1N 6N5

© Eric Benson, 1999

National Library of Canada
Bibliothèque nationale du Canada

Acquisitions and Bibliographic Services
Acquisitions et services bibliographiques

395 Wellington Street
Ottawa ON K1A 0N4
Canada

395, rue Wellington
Ottawa ON K1A 0N4
Canada

Your file Votre référence

Our file Notre référence

The author has granted a non-exclusive licence allowing the National Library of Canada to reproduce, loan, distribute or sell copies of this thesis in microform, paper or electronic formats.

L'auteur a accordé une licence non exclusive permettant à la Bibliothèque nationale du Canada de reproduire, prêter, distribuer ou vendre des copies de cette thèse sous la forme de microfiche/film, de reproduction sur papier ou sur format électronique.

The author retains ownership of the copyright in this thesis. Neither the thesis nor substantial extracts from it may be printed or otherwise reproduced without the author's permission.

L'auteur conserve la propriété du droit d'auteur qui protège cette thèse. Ni la thèse ni des extraits substantiels de celle-ci ne doivent être imprimés ou autrement reproduits sans son autorisation.

0-612-48088-7

Canada

Abstract

Experimental results concerning ballistic excitonic transport in high quality cuprite single crystals are presented and discussed. The onset conditions of this anomalous transport, in the form of a packet propagating at near sound velocity, is compatible with theoretical predictions for Bose-Einstein condensation of n = 1 paraexcitons. Experiments involving the interaction between two packets reveal coherence properties, in agreement with an interpretation assuming an exciton Bose-Einstein condensate as the origin of the packet. The amplification of the packet by thermal excitons and the creation of a stationary condensate in the form of a filament are discussed in terms of radiationless exciton scattering induced by the condensate.

Sommaire

Les résultats d'expériences sur le transport balistique des excitons dans des monocristaux de cuprite de haute qualité sont présentés et discutés. Le transport anormal, sous forme de paquet qui se propage presque aussi rapidement que le son, est compatible avec les prévisions de la théorie Bose-Einstein sur les paraexcitons n = 1. Des expériences sur l'intéraction entre deux paquets révèlent l'existence de propriétés cohérentes conformes à une interprétation voulant qu'un condensat Bose-Einstein soit à l'origine du paquet excitonique. L'amplification du paquet provoquée par des excitons thermiques et la création d'un condensat stationnaire, sous forme d'un filament, sont traitées en termes de diffusion stimulée sans radiation induite par le condensat.

Acknowledgments

I would like to thank Emery Fortin and André Mysyrowicz for their prolonged support and cooperation in the development of this fascinating project. I also greatly appreciated the aide and camaraderie of several other students involved in the setup and/or execution of the experiments. Thanks to Isabelle Brousell, Simon Fafard, Geneviève Lafrenière, Mathieu Massé, Penka Matanska and Stephen Odoysk. And finally I must thank my parents Tom and Michelle, my brother Andrew and my wife Paula for helping me and enduring me over the last few hectic years.

Statement of Originality

All of the results presented in this thesis are from measurements completed at the University of Ottawa by the author. Some of the results printed in this thesis were published in the following papers:

Excitonic Superfluidity in Cu_2O, E. Fortin, E. Benson and A. Mysyrowicz, in *Bose-Einstein Condensation*, Cambridge University Press, pp465-469 (1995).

Soliton Propagation of Excitonic Packets and Superfluidity in Cu_2O, A. Mysyrowicz, E. Fortin, E. Benson, S. Fafard and E. Hanamura, *Solid State Communications* Vol. 92 number 12 pp957-961 (1994).

Study of Anomalous Excitonic Transport in Cu_2O, E. Benson, E. Fortin and A. Mysyrowicz, *Physica Status Solidi* Vol. 191 number 2, pp345-367 (1995).

Directed Beam of Excitons Produced by Stimulated Scattering, A. Mysyrowicz, E. Benson and E. Fortin, *Physical Review Letters* **77**, 896 (1996).

Anomalous Exciton Transport in Cu_2O: Excitonic Superfluidity or Phonon-Wind Effect?, E. Benson, E. Fortin and A. Mysyrowicz, *Solid State Communications* Vol. 101 number 5 pp313-317 (1997).

Coherent Non-linear Interaction Between Two Excitonic Bose-Einstein Condensates, E. Benson, E. Fortin, B. Prade and A. Mysyrowicz, *Europhysics Letters* **40**, 311 (1997).

And presented at the following conferences:

Excitonic Superfluidity in Cu_2O, A. Mysyrowicz, E. Fortin, S. Fafard, E. Benson, G. Lafrenière, invited talk at the CLEO/QELS conference in Baltimore, May 2-6 1993.

Excitonic Superfluidity in Cu_2O, E. Fortin, E. Benson and A. Mysyrowicz, International Workshop on Bose-Einstein Condensation, Levico Terme, Italy, May 31 -June 4 (1993).

Excitonic Superfluidity in Cu_2O, E. Fortin, S. Fafard, E. Benson, G. Lafrenière and A. Mysyrowicz, CAP conference in Vancouver, June 13 - 16 (1993).

Excitonic Superfluidity in Cu_2O, A. Mysyrowicz, E. Fortin, E. Hanamura, E. Benson, invited talk at the CLEO/QELS conference in Anaheim, May (1994).

Anomalous Excitonic Transport in Cu_2O, A. Mysyrowicz, E. Fortin, E. Benson, invited talk at the Workshop on Excitons, Berlin, Nov. (1994).

Study of Excitonic Superfluidity in Cu_2O, A. Mysyrowicz, E. Fortin, E. Benson, invited talk presented in Darwin, Australia and published in *Excitonic Processes in Condensed Matter* edited by Jai Singh, Proc. SPIE 2362 pp140-150 (1995).

Stimulated exciton emission in Cu_2O, E. Fortin, E. Benson and A. Mysyrowicz, EXCON, Prague (1996).

Invited talk in Coeur d'Alène, Idaho, Feb. (1998)

Invited talk at the CLEO/QELS conference in San Francisco, May (1998).

Superfluid Transport of Excitons in Cu_2O, presented in two invited talks at the start of the opening session of the annual meeting of the Electrochemical Society, Boston, Nov. (1998).

Contributed talk at the CAP conference in Fredericton N.B., June (1999)

Table of Contents

List of Figures

Introduction

Seventy years has passed since Einstein originally considered the quantum statistical properties of an ideal gas of non-interacting Bose particles. This work thus attempts to elucidate the current understanding of the phenomenon of Bose-Einstein condensation of excitons in the semiconducting crystal Cu_2O, and the spectacular related effects derived from the macroscopic occupation of a single quantum state.

Excitons in semiconductors constitute an interesting system of bosons with variable density obtained through optical excitation. Because of the low effective excitonic mass, the critical temperature T_c needed for their Bose-Einstein condensation (BEC) is relatively accessible, of the order of a few degrees K at a density of 10^{17} cm^{-3}. Paraexcitons in Cu_2O are particularly attractive candidates for BEC, because of their robust binding energy, their long lifetime and their negligible coupling to the radiation field. Indeed, the direct optical transition from the paraexciton state to the ground state is forbidden to all orders. Therefore, information on the statistical energy distribution of these particles cannot be easily studied by standard photoluminescence spectroscopy. However their long lifetime allows for their migration over long distances, and their subsequent non-optical detection.

We have observed a very peculiar regime of exciton migration in Cu_2O at low temperatures and high particle densities. This anomalous transport takes the form of a packet propagating ballistically at near the lattice sound velocity over distances which can reach several mm. This phenomenon has been attributed to excitonic superfluidity following Bose-Einstein condensation of paraexcitons.

We also present results from experiments designed to establish two specific properties expected from a BE condensate: Stimulated particle emission into a macroscopically filled quantum state and the emergence of a highly coherent state. As a dividend from these experiments we offer evidence of a stationary condensate in the form of a filament.

This work is divided into three main sections; the first deals with the theoretical considerations for BEC of excitons in Cu_2O, the second describes the experimental techniques and the third presents the experimental results along with our interpretations.

1 Theory

This chapter will present the theory behind Bose-Einstein condensation and some of its predictions. In addition the basic properties of the system in which condensation is experimentally realized will be explained along with the manifestations of several theoretical predictions as applied to the system. Briefly, the experimental system consists of excitonic particles in the semiconducting crystal Cu_2O.

1.1 Bose-Einstein Condensation

1.1.1 Bosonic particles

At low temperatures and high densities quantum effects become an important factor in the behaviour of particles. The type of interaction is governed by the particles wave function. Particles whose wave function is odd under particle exchange

$$\psi(\mathbf{r}_1, \mathbf{r}_2) = -\psi(\mathbf{r}_2, \mathbf{r}_1) \tag{1}$$

are called fermions, and those with even wave functions are labeled bosons.

$$\psi(\mathbf{r}_1, \mathbf{r}_2) = \psi(\mathbf{r}_2, \mathbf{r}_1) \tag{2}$$

Fermions are known to be half-integer spin particles, while bosons are integer spin particles. The symmetry of the particle wave functions leads to the two basic properties of fermions and bosons. Fermions are restricted from having more than one particle occupy a single quantum state, while the number of bosons in the same quantum state is unlimited. These properties lead to what is sometimes called a statistical repulsion between fermions, and a statistical attraction between bosons. This statistical effect becomes precipitous at high density and low temperature and is the root cause of a particular macroscopic phenomenon observed only in a system of bosons. The phenomenon proposed by A. Einstein and based on the particle statistics developed by N. Bose has been dubbed Bose-Einstein condensation in analogy with vapor condensing into a liquid. But the new state resulting from BEC is quite different from the three states of matter the we normally deal with in our everyday lives, some of its traits defy common sense, but are simply consequences of the particle wave function symmetry and the macroscopic occupation of a single state.

1.1.2 Ideal Bose Gas

An ideal Bose gas is a system of bosons where quantum statistics are the dominant factor in the behaviour of the particles but where particle interactions are negligible. The ideal Bose gas model closely resembles the experimentally observed exciton system to be introduced later. Predictions about the basic properties of an ideal quantum gas can be made when carefully examining the equations of state. To derive the equations of state for an ideal Bose gas, we must start with the boson partition function $\mathcal{Z}$, in the Grand Canonical Ensemble.

$$\mathcal{Z}(z,V,T) = \sum_{N=0}^{\infty} z^N e^{-\beta \sum \varepsilon_p f_p} = \prod_{\mathbf{p}} \left[\sum_{f_p} (z e^{-\beta \varepsilon_p})^{f_p} \right] \tag{3}$$

where N is the total number of particles, V is the volume, T is the temperature, $f_{\mathbf{p}}$ is the occupation number of a state with energy $\varepsilon_{\mathbf{p}}$, $\mathbf{p}$ is the momentum, β is equal to $1/k_B T$ and z is the fugacity. The fugacity of a gas is its *"tendency to flee"* and is related to the chemical potential, μ of the gas ($z = e^{\beta\mu}$). The total number of particles is limited by the condition $\Sigma f_{\mathbf{p}} = N$, since the sum of the occupation numbers must give the total number of particles. For bosons $f_{\mathbf{p}}$ is any positive integer since there can be an unlimited number of particles in any state. Therefore the sum over $f_{\mathbf{p}}$ in Eq. (3) is a geometric series ($\sum_{s=0}^{\infty} r^s = 1/(1-r)$, $0 < r < 1$) reducing the partition function for bosons to

$$\mathcal{Z}(z,V,T) = \prod_{\mathbf{p}} \frac{1}{1 - z e^{-\beta \varepsilon_p}}$$

The equations of state are

$$\frac{PV}{k_B T} = \log \mathcal{Z}(z,V,T) = -\sum_{\mathbf{p}} \log(1 - z e^{-\beta \varepsilon_p}) \tag{4}$$

$$N = z \frac{\partial}{\partial z} \log \mathcal{Z}(z,V,T) = \sum_{\mathbf{p}} \frac{z e^{-\beta \varepsilon_p}}{1 - z e^{-\beta \varepsilon_p}} \tag{5}$$

In the limit as $V \to \infty$ the possible values of $\mathbf{p}$ form a continuum and the sum over $\mathbf{p}$ in Eqs. (4) and (5) is replaced by an integration such that $\Sigma_{\mathbf{p}} \to V \cdot (2s+1)/h^3 \int d^3p$ where s is the particle spin and h is Planck's constant. The prefactor $V \cdot (2s+1)/h^3$ is due to the fact that allowable values of $\mathbf{p}$ form a cubic lattice in momentum space with a lattice constant

$2\pi\hbar/(L(2s+1))$ where $L = V^{1/3}$, which approaches 0 as $V\to\infty$. Thus, as $V\to\infty$, a volume element of size d^3p in momentum space contains $(V(2s+1)/h^3)d^3p$ lattice points (or momentum states). Rewriting Eqs. (4) and (5):

$$\frac{P}{k_B T} = -\frac{4\pi\cdot(2s+1)}{h^3}\int_0^\infty dp\, p^2 \log(1 - ze^{-\beta p^2/2m}) - \frac{1}{V}\log(1-z) \tag{6}$$

$$n = \frac{4\pi\cdot(2s+1)}{h^3}\int_0^\infty dp\, p^2 \frac{1}{z^{-1}e^{\beta p^2/2m} - 1} + \frac{1}{V}\frac{z}{1-z} \tag{7}$$

Here we see that the ground state term has been split off from the sum before converting to an integral. This is an important and necessary step when dealing with bosons since the ground state term may be as important as the entire sum. Integrating Eq. (6) and (7) we get the following two equations which describe the relation between pressure, P, density, n, temperature, T and fugacity, z, for an ideal Bose gas:

$$\frac{P}{kT} = \frac{(2s+1)}{\lambda^3} g_{5/2}(z) - \frac{1}{V}\log(1-z) \tag{8}$$

$$n = \frac{(2s+1)}{\lambda^3} g_{3/2}(z) + \frac{1}{V}\frac{z}{1-z} \tag{9}$$

where $\lambda = \sqrt{2\pi\hbar^2 / mk_B T}$ is the thermal wavelength. The function $g_n(z)$ is defined as the sum $g_n(z) \equiv \sum_{l=1}^{\infty} z^l / l^n$.

The average occupation number as a function of temperature for bosons in an ideal gas can also be calculated using the partition function

$$< f_p >= -\frac{1}{\beta}\frac{\partial}{\partial \varepsilon_p}\log \mathcal{Z} = \frac{ze^{-\beta\varepsilon_p}}{1 - ze^{-\beta\varepsilon_p}} \tag{10}$$

For the ground state ($\varepsilon_p = 0$) the average occupation number $<f_0>$, is simply $z/(1-z)$, therefore we can rewrite Eq. (9) as

$$\frac{< f_0 >}{V} = n - \frac{(2s+1)}{\lambda^3} g_{3/2}(z) \tag{11}$$

where $g_{3/2}(z)$ is a monotonically increasing function over the range $0 \le z \le 1$ with a maximum of $\cong 2.612$ for $z = 1$. Equation (11) implies that there is a finite fraction of particles occupying the ground state when the density and temperature are such that

$$n > \frac{(2s+1)}{\lambda^3} g_{3/2}(1) \tag{12}$$

This macroscopic occupation of the ground state is termed Bose-Einstein condensation and is a change of phase to what is sometimes called a fourth state of matter, which unlike other phase changes is not due to particle interactions but due to the symmetry of the wave function. From Eq. (12) we can now define a critical density above which particles in the ground state of an ideal Bose gas at a fixed temperature will condense into a new phase.

$$n_c = 2.612 \cdot (2s+1) \cdot \left(\frac{mk_B}{2\pi\hbar^2}\right)^{3/2} T^{3/2} \tag{13}$$

The group of particles in the ground state forms an entity called the condensate. The fraction of total particles in the condensate at a temperature given by λ can be found by dividing both sides of Eq. (11) by the density n, giving

$$\frac{< f_o >}{N} = 1 - \frac{(2s+1)}{n\lambda^3} g_{3/2}(z) \tag{14}$$

We now replace $g_{3/2}(z)$ by $g_{3/2}(1)$ since for the condensed fraction to be non-zero, $z \to 1$. Using Eq. (12) for fixed n, $g_{3/2}(1) = n\lambda_c^3/(2s+1)$ where λ_c is calculated at the critical temperature T_c and substituting this result into Eq. (14) we obtain

$$\frac{< f_o >}{N} = \begin{cases} 1 - \left(\dfrac{T}{T_c}\right)^{3/2} & T \le T_c \\ 0 & T \ge T_c \end{cases} \tag{15}$$

Equation 15 is represented graphically in Fig. 1, and it can be seen that a finite fraction of particles are in the ground state for $T < T_c$. It can also be shown by evaluating terms of the summation in Eq. (5) as $V \to \infty$ that $<f_{\mathbf{p}}>/N$ is always zero for $\mathbf{p} \neq 0$. Therefore, for $T > T_c$, no energy level is occupied by a finite fraction of all the particles, and the particles are said to be "spread thinly" over all levels. For $T < T_c$, a finite fraction of particles $1 - (T/T_c)^{3/2}$ occupies the level $\mathbf{p} = 0$ while the rest of the particles are spread

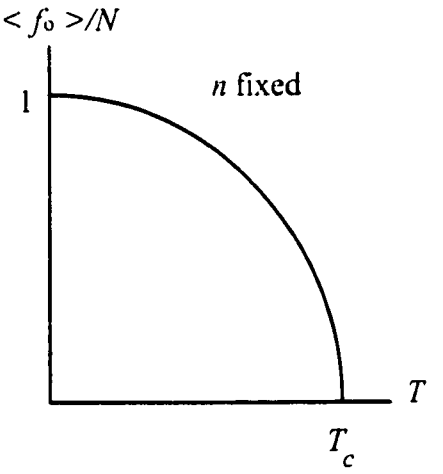

Fig. 1 Average occupation of the ground state as a function of temperature.

thinly over all the excited states.

The pressure in the condensate can be found using Eq. (8) instead of (9) as a starting point. The last term of Eq. (8) can be ignored since it is of order log(N) whereas the first term is of order N. This means that no particle in the ground state ($\varepsilon_p = 0$) can contribute to the pressure for any z. Using the same procedure as above, the pressure P as a function of T is

$$P = \begin{cases} g_{5/2}(z) \cdot (2s+1) \cdot k_B T / \lambda^3 & n < n_c \\ 1.342 \cdot (2s+1) \cdot k_B T / \lambda^3 & n > n_c \end{cases} \qquad (16)$$

where $g_{5/2}(1) \cong 1.342$ for $n > n_c$. A plot of the ideal Bose gas pressure versus particle density for several temperatures is shown in Fig. 2. The critical pressure for BEC is shown by the dashed line which is proportional to $n^{5/3}$. The relation between critical pressure and particle density can be obtained by substituting $T = \text{cst} \cdot n^{2/3}$ from Eq. (13) into Eq. (16) for $z = 1$. The most notable feature in Fig. 2 is the saturation of the gas pressure as a function of density beyond the BEC transition. This break in the behaviour of the pressure as a function of particle density is an indication of the change of phase, from gas to condensate, undergone by the particles. Such breaks in the behaviour should be apparent in all the physical properties of the gas after the transition. Notably, the rate of expansion of the gas specified by the diffusion coefficient should decrease abruptly when the particles enter the common momentum state, and the transport of the condensate over macroscopic distances (as compared to the crystal lattice spacing in our experiments) should be greatly enhanced due to a spectacular property, also observed in liquid He^4 and intimately linked with BEC: superfluidity. In addition, as will be seen in Sec. 1.6, the condensate can be viewed as a wave (or matter wave) with a definite phase, implying that interference should occur between condensates.

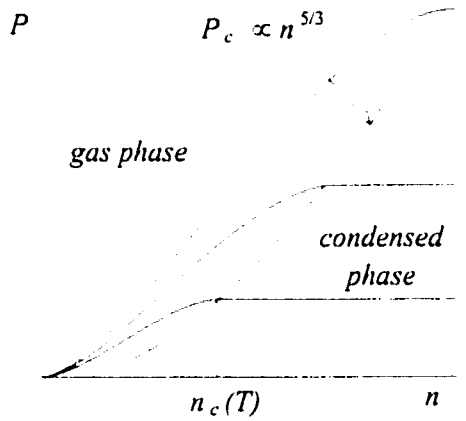

Fig. 2 Isotherms of an ideal Bose gas.

The ideal Bose gas theory can be extended to the more realistic case of a non-ideal Bose gas by including first order particle interactions; however the main properties

predicted by the ideal Bose gas theory are not modified. For example, while the compressibility of the ideal Bose gas (the inverse of the slope in Fig. 2, which equals infinity for $n > n_c$) becomes finite for the non-ideal case, it remains very large and still has a discontinuous jump at the transition point [1]. The non-ideal Bose gas theory will not be used in this work since some assumptions made in the ideal case such as an infinite volume, homogenous density and thermodynamic equilibrium are not completely satisfied at all times in our experimental system. Refined predictions made from simple extensions of the ideal case seem dubious, however we stress that the basic characteristics of the ideal gas model such as the predicted critical density should be apparent. A more complete model of our exciton system which accounts for the stability of a moving condensate and the superfluid behaviour (impossible for an ideal Bose gas) by incorporating exciton-phonon interactions will be introduced in Sec. 1.5.

1.2 Excitons

An electron excited into the conduction band is still physically close to the hole left behind in the valence band; and since they have opposite charge, they can bind together much in the same way a proton and electron combine to form a hydrogen atom, although in the present case, the Coulomb interaction is screened by the periodic lattice field. The electrically neutral entity formed by the bound electron-hole pair is called an exciton. It is a boson since the exciton spin s is either 0 or 1; s = 1 excitons are labeled orthoexcitons and s = 0 excitons are called paraexcitons. The binding energy E_b, of the exciton follows the same type of series as observed in hydrogen, but is modified by the parameter ε, which takes into account the screening effect of the ions in the lattice.

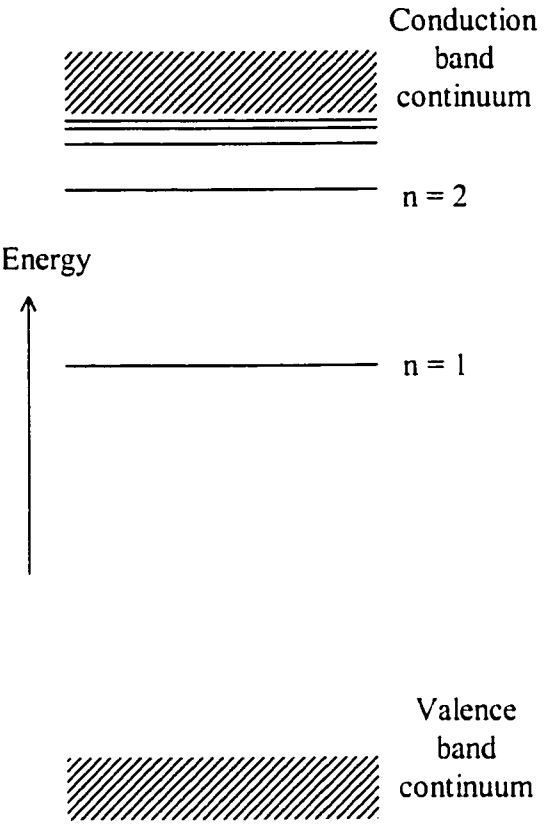

Fig. 3 Exciton energy levels for k=0.

$$E_b = \frac{e^4 \mu_{ex}}{2\hbar^2 \varepsilon^2 n^2} \quad n = 1,2,3,\ldots \tag{17}$$

where e is the electronic charge, ε is the static dielectric constant (~ 7 in Cu_2O [2]) and $\mu_{ex} = m_e m_h/(m_e + m_h)$ is the exciton reduced mass where m_e and m_h are the electron and hole effective masses respectively. Due to spin orbit coupling, the paraexciton will have a slightly larger binding energy than the orthoexciton. From Eq. (17), which is schematically represented in Fig. 3 (although the spacing between the exciton levels has been exaggerated for clarity), it can be seen that the exciton energies will be smaller than the energy gap of the crystal and will allow for absorption of photons in a region expected to be transparent to light. The exciton energy levels will manifest themselves as narrow absorption peaks in the crystal absorption spectrum mentioned in the following section.

The radius of the excitonic entity (half the mean distance between the electron and hole) is given by

$$r_{ex} = a_o \frac{m_o}{\mu_{ex}} \varepsilon n^2 \qquad (18)$$

where a_o is the Bohr radius and m_o the electron rest mass. Small radius excitons for which r_{ex} is smaller or on the order of the lattice constant are usually bound to their parent atoms and are called Frenkel excitons. Larger radius excitons (r_{ex} > lattice constant), which we study in this work, are called Wannier excitons; this type of exciton can be viewed as a free particle, able to migrate through the crystal lattice with frequent collisions with the ion cores.

This migration process, modeled by Brownian dynamics, is called diffusion and is characterized by the relaxation time τ_s (or mean time between collisions or scattering time). The particle mobility B (i.e. the drift velocity acquired by the particle due to an external force) is at the heart of the diffusion process and is defined by $B = \tau_s/M$ where M is mass of the particle being scattered. (N.B. Many papers quote the electronic mobility $\mu = eB$ where e is the electronic charge). The diffusion coefficient D which is generally available experimentally is related to the mobility by the Einstein relation $D = BkT$. The diffusion process will be used to characterize many of the experimental results and will be described in greater depth in the Secs. 1.5 and 3.1.1.

The time between exciton creation and recombination is the exciton lifetime τ, which is determined by the probability that the electron undergoes a transition back to the valence band either directly or indirectly. This probability is in turn governed by quantum selection rules and the density of the initial and final energy states. However, an exciton can be dissociated by an electric field which is of the same order of magnitude as the field between the electron and hole in the exciton. The dissociation produces a free electron in the conduction band and a free hole in the valence band able to supply the initial creation energy as an electrical current in an external circuit, a detailed description the exciton mediated photovoltaic effect is given in Sec. 2.2.1. Therefore in the diffusive regime a high purity crystal free of defects will allow excitons to travel the maximum theoretical average distance, given by the diffusion length $\ell = (D\tau)^{1/2}$.

The initial density of excitons optically created in a crystal by a pulse of light will vary with depth and can be calculated in the following manner: the density of excitons in a layer of thickness dz parallel to the illuminated face is equal to the loss of photons by absorption in the thickness dz divided by dz, assuming that every photon produces an exciton. Therefore, using $I(z) = I_{max}e^{-\alpha z}$ where $I(z)$ is the intensity of light at a depth z from the surface, I_{max} is the incident intensity and the fact that the $I(z) \propto N(z)/A$ where $N(z)$ is the number of photons at a depth z from the surface and A is the illuminated area, the density of excitons at a depth z is given by

$$n(z) = -\frac{1}{A}\frac{d}{dz}N(z) = -\frac{d}{dz}I(z)\delta t\frac{\lambda}{hc} = \frac{\alpha\lambda I_{max}\delta t}{hc}e^{-\alpha z} \qquad (19)$$

where α is the absorption coefficient, λ is the incident wavelength and δt is the duration the surface is illuminated. Note that for Eq. (19) to be valid, the time δt over which the photons are absorbed must be much shorter than the exciton lifetime and the excitons must remain at their initial location during the pulse. The first assumption is not a concern here since the laser pulse used in the experiments has a duration of 10 nsec, while the paraexciton lifetime in Cu_2O is greater than 10 μsec [3]. The second assumption is more difficult to satisfy since the exciton mobility can be very large ($\mu \sim 10^6$ cm^2/(eV sec) [4, 5]) at low temperatures resulting in rapid diffusion from the excitation region. This problem will be tackled later on. Summarizing, the density of excitons at a given depth will mostly depend on the incident intensity and the absorption coefficient since both these parameters can be greatly varied ($> 10^3$), and depend to a lesser extent on the laser wavelength which in our case undergoes only small changes (~ 10%).

1.3 Phonons and Absorption

The phonons in Cu_2O have been extensively studied [6, 7] by many techniques including recombination luminescence, optical absorption and Raman scattering since they play an important role in the absorption and recombination of excitons and free carriers. A synopsis will be presented here to simplify discussions presented later on.

The six phonons shown in Fig. 4 are the most important modes that interact with the excitons in our experiments. The vertical scale of the acoustic modes is increased by factor of 1000 so that they are visible on the figure. The optical modes are flat as a function of wave vector in the region of interest. The slope of an acoustic mode is the group velocity for that particular mode and hence defines the speeds of sound in the crystal. The LA phonon-exciton coupling is at least an order of magnitude larger than the TA phonon-exciton coupling [8] hence the LA phonons play a much larger role in the exciton dynamics seen later and the speed of sound generally refers to the LA phonon group velocity.

The Γ_{15}^- TO phonon is coupled to the radiation field and its dispersion is modified when it crosses the photon dispersion curve creating two branches both asymptotically reaching the photon curve as seen in Fig. 4. In the crossing region where the phonon is modified the mode is called a polariton, short for polarization wave and photon. Therefore

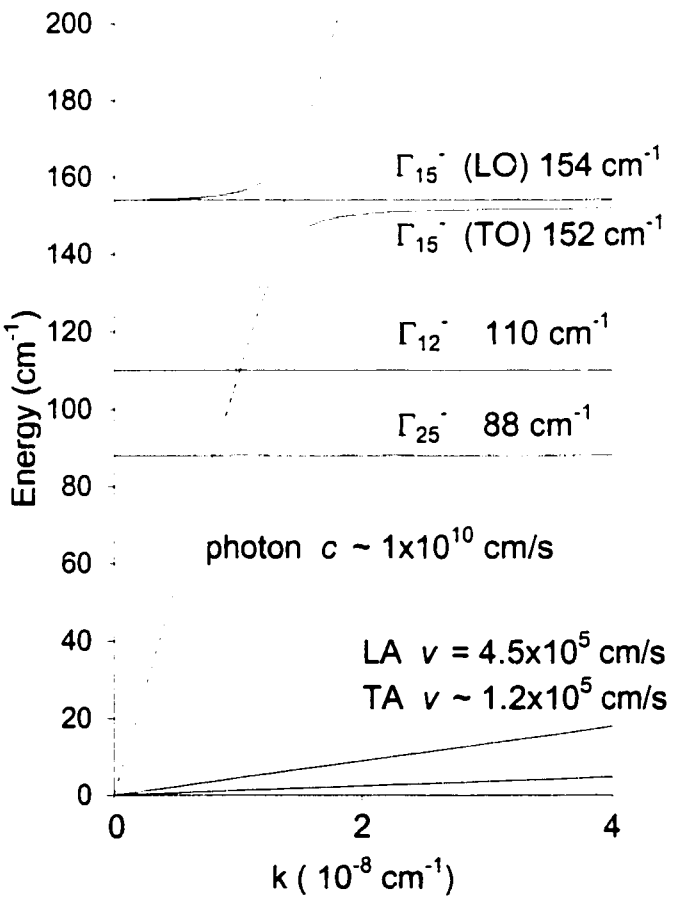

Fig. 4 Phonon dispersion curves for Cu_2O (solid lines) and the photon dispersion curve (dotted line). The LA and TA curves are magnified by a factor of 1000. LA stands for longitudinal acoustic, TA is transverse acoustic, LO is longitudinal optical and TO is transverse optical.

when a photon enters the crystal with about the same energy as a TO phonon a polariton is created. The polariton velocity is the group velocity of the coupled mode and therefore ranges from 10^6 to 10^{10} cm/s depending on the photon energy. Note the LO phonon does not interact with light and the upper polariton branch is associated with the TO phonon even though near $k = 0$ both the LO and TO modes have the same energy.

The exciton dispersion relationship is also coupled to the radiation field and the exciton polariton effect has been measured in Cu_2O [9]. The behaviour is analogous to the polariton mentioned above with only the transverse exciton with a dipole moment normal to its wave vector interacting with the photon, which has a transverse mode only.

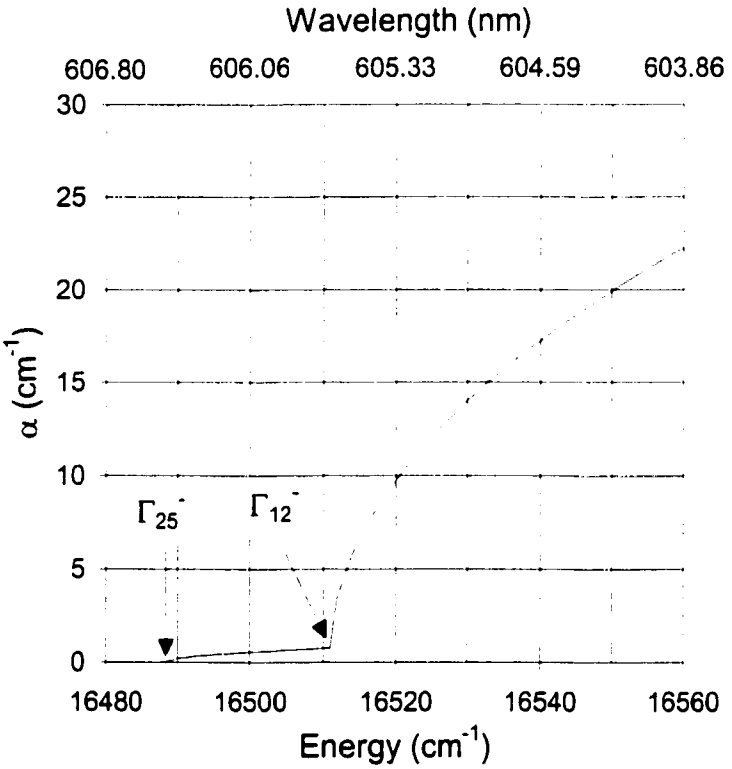

Fig. 5 Absorption coefficient for Cu_2O at 2K derived from a fit of data to be presented in Sec. 3.4.3. The arrows denote the positions of the Γ_{25}^- and Γ_{12}^- optical phonons. The energy of the n = 1 orthoexciton (X_o) is 16401.5 cm^{-1} (λ = 609.7 nm).

Light can be absorbed by the crystal when its energy is greater than the energy gap between the valence and conduction bands, and since the density of states in both bands is high and continuous, the absorption is strong and fairly flat (away from the band edge) as a function of wavelength. As mentioned earlier light can also be absorbed by the discrete exciton states producing absorption peaks below the band gap. With the assistance of phonons, absorption can also begin at a discrete energy (the energy of a phonon) above the exciton peak since a photon can create an exciton and one or more phonons simultaneously. As can be seen in Fig. 5, the exciton-phonon absorption edge in Cu_2O has two thresholds. There is a small step for photons with energy: $X_o + \Gamma_{25}^-$ where X_o is the orthoexciton

energy and Γ_{25}^- is the optical phonon energy, and a second more rapid rise in absorption for photons with energy: $X_o + \Gamma_{12}^-$. After the initial rise there is a continuum due to absorption from orthoexciton + optical phonon + LA phonon(s) the latter phonon having variable energy and creating the continuum of states. The rate of increase of α follows $E^{1/2}$ as expected from a phonon assisted direct transition [10]. The sharper rise in the second absorption threshold is due to the stronger coupling (factor of ~ 20) between the orthoexciton and the Γ_{12}^- phonon [11]. The transition probability for a photon with energy: $X_p + \Gamma_{25}^-$ where X_p is the paraexciton energy, is several orders of magnitude weaker than the $X_o + \Gamma_{12}^-$ case [11] and results in a correspondingly smaller α, this is verified in the experimental absorption data by the absence of a paraexciton absorption edge.

1.4 Condensation of Excitons

BEC is believed to be the main cause of the spectacular properties of superfluid He^4 below the λ-point. However, due the large mass of the Helium atom, and large interactions between particles, the λ-transition has defied all theories attempting to explain it simply in terms of BEC. Therefore a more dilute variable density system where Bose statistical effects are predominant is needed to verify the quantum properties of the condensate.

Under the right conditions, excitons created in ultra-pure direct gap semiconducting Cu_2O crystals are prime candidates to undergo Bose-Einstein condensation. The excitons are bosons which behave very much like an ideal gas, due to their small mass, $2.7m_o$ [12] and small radius $r_{ex} \sim 0.7$ nm [13]. The criteria for a dilute gas, $nr_{ex}^3 << 1$ where n is the exciton density, is satisfied for excitons in Cu_2O for densities up to about 10^{20} cm^{-3} ($nr_{ex}^3 = 3 \cdot 10^{-2}$). The small radius also helps prevent the breakdown of excitons into an electron-hole plasma at high density, called the Mott dissociation. The Mott transition occurs when $nr_{ex}^3 \sim 0.3$ (in the case of Cu_2O; $n = 10^{21}$ cm^{-3}). A repulsive exciton-exciton hard core potential [14] insures against the formation of excitonic molecules such as biexcitons [15] which have been observed in CuCl [16]. Furthermore, the n = 1 paraexciton is a forbidden transition to all orders and has an extremely large binding energy (~ 150 meV). These two facts lead to an exceptionally long lifetime and stability against thermal dissociation since $k_BT \sim 0.2$ meV at 2K. Estimates for the paraexciton lifetime range from 13 μsec to 150 μsec and perhaps 1 msec [3, 11]. The spread in the values reflects the great difficulty of measuring the lifetime. Furthermore the effective lifetime in a particular crystal may be greatly affected by the sample quality since non-radiative recombination (enhanced by defects) is dominant for the paraexciton.

Since the n = 1 paraexciton is a forbidden transition, the paraexcitons must be created in an indirect fashion in Cu_2O. A photon with energy greater than E_{gap} excites an electron into the conduction band where it quickly (on the order of a psec [17]) simultaneously combines with the hole to form an exciton and thermalizes with the other excitons by phonon emission. Both exciton species are created in the process with the ratio of ortho to para being 3 to 1 since the density of states contains the degeneracy factor $g = 2s+1$. The orthoexciton has a very short lifetime, $\tau \sim 3$ to 30 nsec [3, 11]

principally due to down conversion to the lower (by 12 meV) paraexciton state. The down conversion is accompanied by the emission of a LA phonon. Spectroscopic analysis indicates that both exciton species have the same temperature which can be significantly higher than the lattice temperature [18] if the incident photon energy is much greater than E_{gap}.

The critical density required for BEC is calculated using Eq. (13); for paraexcitons (spin 0 and mass $2.7m_o$) at a temperature of 2K

$$n_c \cong 8 \times 10^{16} \text{ [cm}^{-3}\text{]} \tag{20}$$

which corresponds to a very dilute gas using the criteria mentioned above. To calculate the density of excitons created by optical excitation in Cu_2O, Eq. (19) is used with the appropriate absorption coefficient for the incident laser wavelength, found in the literature [19, 20] and from our own measurements. The intensity was corrected to include losses by reflection at the sample surface and cryostat windows (refraction indices 2.7 and 1.46 [21]); the transmitted intensity was 0.7 of the laser intensity stated in the figure. The results are plotted in Fig. 6, the two lower traces with relatively small α (accessible using light from a dye laser), show a very gradual absorption over 200 μm while the curve corresponding to the absorption of light of the 2nd harmonic of a Nd:YAG laser (λ = 532 nm) is steeply attenuated over 10 μm. The intensity for the two lower traces was chosen so that the maximum density (i.e.

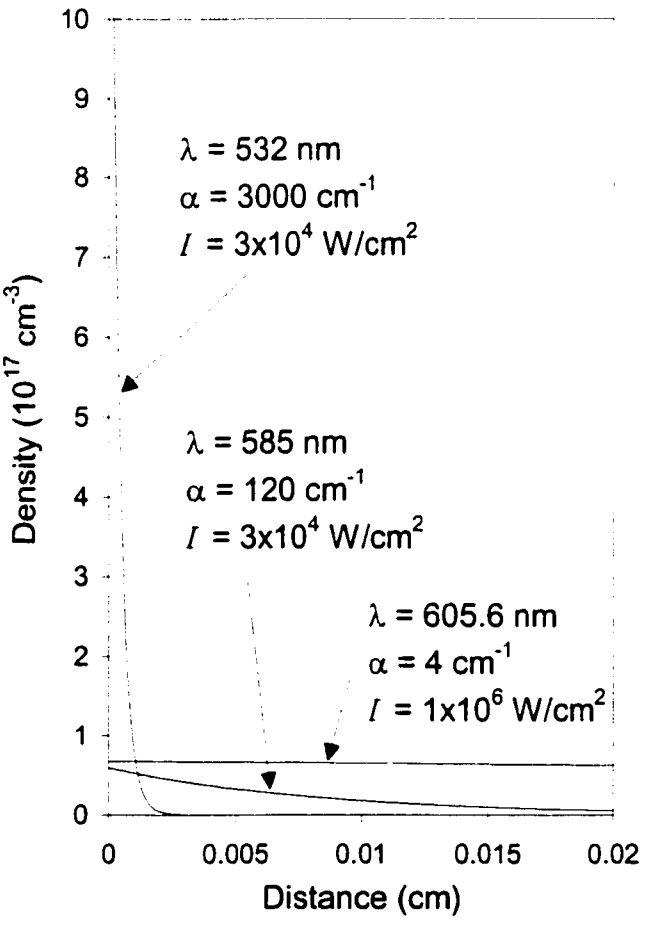

Fig. 6 Exciton density profile calculated using Eq. (19) after a short laser pulse ($t << \tau$) for three different incident wavelengths and intensities in Cu_2O at 2K.

near the surface) is very close to the critical density calculated in Eq. (20). The λ = 532 nm trace is plotted with the same intensity as the λ = 585 nm trace, as can be seen the green laser produces a much higher density of excitons near the surface than the yellow laser. At first glance it would seem the green laser would be much more effective at reaching the critical density for condensation, however the critical density depends on temperature, and the excess energy deposited by the green laser is three times that of yellow beam. The excitons in Cu_2O must shed this excess kinetic energy by phonon production which results in heating of the exciton gas. The heating effects at high densities (10^{18} - 10^{19} cm^{-3}) can produce temporary exciton gas temperatures up to 30K [18]. Furthermore the initial exciton cloud will expand during the and after the laser pulse changing the density profile. The initial expansion of the sharp absorption profile may be much greater due to the higher density gradient, so the exact balance of temperature and density of the excitons at early times is a very difficult problem, but it is known that exciton gas temperature does reach equilibrium with the lattice after ~ 30 nsec [18].

The lattice can also be heated by the phonons; the heating energy Q will be equal to the number of photons times the excess energy of a photon. The maximum excess energy is given by E_{532} - $E_{n=1}$: the energy of a λ = 532 nm photon (2.331 eV) minus the n=1 exciton energy (2.02 eV at 2K). The following expression can be used to evaluate the approximate final lattice temperature in the volume delimited by the illuminated area and α^{-1} (0.63 of all the photons are absorbed within this distance, dubbed an absorption length). Eq. (21) will give the maximum possible temperature since it is assumed that no lattice energy diffuses away during the heating.

$$\begin{aligned} Q &= m \cdot c(T) \cdot \Delta T \\ N_o \int dE &= m \int_{T_o}^{T_f} c(T) dT \\ n_{ex}(E_{532} - E_{n=1}) &= \frac{\rho c_o}{4}[T_f^4 - T_o^4] \end{aligned} \tag{21}$$

where $c(T) = c_o T^3$ (c_o = 5.86x10^{-6} J/g·K) is the specific heat capacity at low temperature in Cu_2O [22], ρ = 6.14 g/cm^3 is the mass density of Cu_2O, T_f and T_o = 2K are the final and initial temperatures respectively. At exciton densities of 10^{20} cm^{-3} T_f ~ 27K for λ = 532 nm; for longer wavelengths at the same exciton density T_f decreases since less excess energy is imparted to the crystal e.g. T_f ~ 20 K for λ = 585 nm for the same exciton

density. It is important to note that at equivalent *intensities* the exciton density and temperature will be much lower for the $\lambda = 585$ nm pulse as compared to the $\lambda = 532$ nm pulse due to the large change in α. In addition these results are certainly overestimated since experimental exciton luminescence lines do not appreciably shift during the laser pulse indicating the lattice temperature remains below 20K [23].

1.5 Excitonic Superfluidity

Superfluidity has long been observed in liquid He^4 as a frictionless flow of the liquid below the λ-transition due to the BEC of the He^4 atoms. This work will show that the nearly ballistic transport of excitons in Cu_2O can be attributed to excitonic superfluidity due to BEC of the excitons. In this case the superfluid, or condensate, is actually more like a gas flowing without resistance through a crystal. A simple theoretical explanation of the nearly ballistic transport comes from the application of the Landau criterion to the excitonic superfluid. The Landau criterion simply postulates that a superfluid is stable against elementary excitations, which deplete the superfluid population by exciting a particle out of the condensate, if the superfluid travels at less than the speed of sound in the medium. However the stability of a moving packet of excitons (i.e. the condensate) is a much more difficult problem due to the exciton-phonon interactions. A very good solution to the problem of excitonic superfluidity has been proposed by Loutsenko and Roubtsov (LR) [24], a brief description will be given here.

LR argue that what we have observed experimentally is the propagation of an exciton-phonon condensate, the interaction between phonons and excitons playing a key role when the propagation velocity nears the sound velocity. The LR model has a Hamiltonian with three logically separate terms: an exciton term which includes an exciton-exciton potential, a phonon term and most importantly an interaction term with an exciton-phonon potential. The system of field equations derived from this Hamiltonian for a Bose gas moving with uniform velocity, is neither Galilean nor Lorentz invariant due to the inclusion of the phonon field. This noninvariance causes the effective exciton-exciton potential (combined effect of exciton and phonon interactions) to be anisotropic and velocity dependent. The most important result of the LR model is the prediction of a critical velocity v_o above which the sign of the effective potential changes, going from the normally repulsive potential to an attractive potential. The critical velocity is given by

$$v_o = \sqrt{v_s^2 - (\sigma_o^2 / \chi_o \rho)} \qquad (22)$$

where v_s is the LA phonon velocity, σ_o is the exciton-LA phonon coupling constant, χ_o is the exciton-exciton interaction constant and ρ is the crystal density. In Cu_2O the

substitution of the appropriate parameters into Eq. (22) leads to a critical velocity of ~ 0.5 - 0.7 v_s. Above the velocity of sound the potential becomes repulsive again. Propagation of the condensate at $v_o < v < v_s$ gives rise to a family of stable stationary (in the uniformly moving frame of reference) solutions to the aforementioned system of field equations. The resulting particle distribution has the form of a soliton

$$n(x) = n_o \operatorname{sech}^2\left(x/\Delta\right) \qquad \frac{1}{\Delta} = \beta n_o \tag{23}$$

where the spatial width Δ (half width half maximum: HWHM = 0.88Δ) is related to the soliton amplitude n_o by the parameter β. Therefore the soliton width is not a function of time and the packet can propagate over a large distance without expanding or changing its shape. This solution is logical if the soliton is associated with a condensate where all the particles have the same wave vector.

The LR theory predicts that below the critical velocity a spatially inhomogeneous condensate (i. e. a packet) is unstable and that it disintegrates. Therefore below the critical velocity the transport should be diffusive as expected from Brownian dynamics and the particle distribution has the form

$$n(x,t) = \frac{n_o}{\sqrt{4\pi Dt}} \exp\left(\frac{-(x-vt)^2}{4Dt}\right) \exp\left(\frac{-t}{\tau}\right) \tag{24}$$

which is the 1D solution of the diffusion equation with drift term

$$\frac{\partial n}{\partial t} = D\frac{\partial^2 n}{\partial x^2} - v\frac{\partial n}{\partial x} - \frac{n}{\tau} \tag{25}$$

where v is the drift velocity, D is the diffusion coefficient and τ is the particle lifetime. The drift term $v\partial n/\partial x$ may originate from the coupling between excitons and non-equilibrium LA phonons produced by the exciton cooling process alluded to in Sec. 1.4. In the diffusive regime the width of the distribution increases as a function of time, in fact the rate of increase determines the diffusion coefficient D. This is in contrast with the constant width of the soliton distribution associated with the condensate.

Finally we note that in the LR theory a spatially homogeneous condensate is a stable solution for excitons moving at $v < v_o \sim v_s / 2$. The implications of this solution will be discussed in Sec. 3.4.

1.6 Condensate Interference

It is well known that two ideal classical gas clouds do not display interference effects because there is no coherence between them. To be more specific, the lack of coherence means there is a random phase difference between the two wave functions describing each cloud, or each wave function is said to have no definite phase. The arbitrary phase of the cloud wave function stems from that fact that the cloud wave function is a superposition of the individual particle wave functions, which are in this case uncorrelated.

If the wave functions of all the clouds particles are the same (i.e. all the particles are in the same state, the condensate) the wave function that describes the cloud now inherits the correlation, or order, present between the particles and the cloud wave function acquires a definite phase. Two wave functions with definite phases (i.e. condensates) are said to be mutually coherent and can interfere.

Normally interference is thought of as the linear superposition of coherent waves which gives rise to a set of maximums and minimums in the resulting wave. Incoherent input waves would otherwise produce a homogeneous field. Since the condensate is a solitary wave (soliton), and the medium in which it propagates is nonlinear, the mechanism behind the interference of two condensates is not this simple case. However our experimental system is analogous with the well known situation encountered in nonlinear optics of the interaction between two very short (femtosecond) high intensity laser pulses. The coherent exciton-phonon polarization field of high amplitude describing the condensate replaces the coherent laser field. The nonlinear response of the crystal is expressed as a perturbation expansion in odd terms of the polarization field limited to fifth order:

$$-i\frac{\partial\psi}{\partial t} = a\frac{\partial^2\psi}{\partial x^2} + b|\psi|^2\psi - c|\psi|^4\psi \qquad (26)$$

The waves will interact according to the fundamental interaction of their constituents, in this case excitons. Therefore in the particle picture the first nonlinear term corresponds to two-body interaction, which we assume attractive, following LR. The higher order nonlinear term corresponds to three body repulsive (hard core) preventing biexciton formation. For the case of two condensates traveling uniformly in the same direction

separated by an initial distance (longitudinal interference) we have solved this nonlinear Schrödinger equation (NLSE) numerically using the following split-step algorithm.

```
for (j = 1; j <= nBPM; j++)
{
 dfour1(data, n, 1);          //Fourier transform
 for (i = 1; i < n;i += 2)   {
      phi = (i-1)*(i-1)*coeff;
      data[i] = (tempr=data[i])*(tempcos=cos(phi))-
                        data[i+1]*(tempsin=sin(phi));
      data[i+1] = tempr*tempsin+data[i+1]*tempcos;
 }
 for (i = n+1; i < n2; i += 2)     {
      dfreq = (double) (i-n2-1);
      phi = dfreq*dfreq*coeff;
      data[i] = (tempr=data[i])*(tempcos=cos(phi))-
                        data[i+1]*(tempsin=sin(phi));
      data[i+1] = tempr*tempsin+data[i+1]*tempcos;
 }
 dfour1(data, n, -1);  //Transform back to real space
 for (i = 1;i < n2;i += 2)   {
      data[i] *= n_inv;
      data[i+1] *= n_inv;
      norm = data[i]*data[i]+data[i+1]*data[i+1];
      phi = (c*norm-b)*norm*delta_t;
      data[i] = (tempr=data[i])*(tempcos=cos(phi))-
                        data[i+1]*(tempsin=sin(phi));
      data[i+1] = tempr*tempsin+data[i+1]*tempcos;
 }
```

To simplify the problem, a 1D case was assumed. We also ignored the contribution of thermal excitons and further only considered the system evolution after formation of two condensates with an assumed fixed phase relationship. As initial conditions, both packets were taken as bright solitons of width Δ traveling at uniform velocity v:

$$\Psi(x,t) = [A_1(x,t) + A_2(x,t+\tau)]e^{iw(t-x/v)}$$
$$|A_i(0,t)|^2 = |A_{0,i}|^2 \operatorname{sech}^2(t/\Delta) \tag{27}$$

The resulting fits of $|\Psi|^2(x, t)$ to the experimental data will be shown in Sec. 3.2.1.

One can also envision the case of transverse interference (i.e. two condensates separated by a distance perpendicular to their common propagation direction). From the LR theory the attractive potential encapsulated in the parameter b changes sign and becomes repulsive for interactions perpendicular to the propagation direction. No

theoretical model has been developed for this case, the experimental results along with some conclusions will be presented in Sec. 3.1.6.

1.7 Amplification by Stimulated Emission

As mentioned earlier it is well known that half-integer spin particles (fermions) obey the Pauli exclusion principle, which prevents multiple occupancy of a given quantum state. On the other hand, particles with integer spin (bosons) obey a reverse rule. Their scattering probability towards a state already occupied by other bosons is enhanced by a factor $f + 1$, where f is the occupation number of the final state. Under favorable conditions, this quantum 'attraction' can become precipitous. Light amplification by stimulated emission of radiation (LASER) provides a unique example of this effect for massless Bose particles, photons. However, amplification by stimulated emission is a much more general effect applying to any bosonic field including massive particles. In this work we explore the stimulated emission (without participation of radiation) of a special case of massive Bose particles, optically inactive paraexcitons in a Cu_2O.

In its spontaneous form, the basic exciton scattering process consists in the annihilation of an exciton of energy E_i and wave vector $\mathbf{K}_i$, the creation of an exciton (E_f, $\mathbf{K}_f$) and the simultaneous emission (or absorption) of an acoustic phonon. It represents one step in a chain of scattering events after injection of hot excitons in an insulating crystal leading to their energy relaxation and to the establishment of a quasi-thermodynamic equilibrium among the particles. Since we deal with a three body elementary process, the initial exciton (E_i, $\mathbf{K}_i$) is coupled to a continuum of final states, defined by the set of vectors ($\mathbf{K}_f$, $\mathbf{q}$) which satisfy energy and momentum conservation laws.

$$E_i = E_f \pm \hbar\omega_q \qquad \mathbf{K}_i = \mathbf{K}_f \pm \mathbf{q} \tag{28}$$

with the additional constraints

$$E_{i,f} = \frac{\hbar^2 \mathbf{K}_{i,f}^2}{2m} \qquad \hbar\omega_q = \hbar\mathbf{q}\mathbf{v} \tag{29}$$

where v is the longitudinal sound velocity in the crystal and m the exciton effective mass. From the point of view of excitonic motion, the succession of such spontaneous events leads to a diffusive exciton transport modeled by the diffusion equation mentioned above.

In the stimulated version of the process, exciton scattering is induced by an incident exciton field (f_c, E_c, $\mathbf{K}_c$), where $f_c >> 1$ is the occupation number of mode c. The directions and magnitudes of $\mathbf{K}_f$ and $\mathbf{q}$ are prescribed by the supplementary conditions

$$E_f = E_c \qquad \mathbf{K}_f = \mathbf{K}_c \tag{30}$$

The growth of the bosonic wave is obtained from the time rate change of the average number of bosons in mode c [25],

$$\frac{\partial f_c}{\partial t} = \frac{2\pi}{\hbar}\sum_q \gamma^2(q)\Big\{ f_{c+q}(1+f_c)\Big[(1+f_q)\delta(\hbar\omega_q + E_c - E_{c+q}) + f_q\delta(\hbar\omega_q - E_c + E_{c+q})\Big] - (1+f_{c+q})f_c\Big[(1+f_q)\delta(\hbar\omega_q - E_c + E_{c+q}) + f_q\delta(\hbar\omega_q + E_c - E_{c+q})\Big]\Big\} \tag{31}$$

where $f_i = f_{c+q}$ and f_q are respectively the occupation probabilities of excitons and acoustic phonons with energy E_k and $\hbar\omega_k$, and $\gamma(q) = \gamma_0 \cdot \sqrt{q}$ is the matrix element of the exciton-phonon interaction. An excitonic Bose condensate with $f_c >> 1$ on the R.H.S. of Eq. (31) can provide the triggering term for the stimulated excitonic transition. However stimulated exciton scattering can occur even below Bose condensation threshold since in the quantum-degenerate statistical regime several exciton modes near $K = 0$ have already a large occupation number. The first term in Eq. (31) expresses an amplification process, the second term a loss process in which an exciton is scattered out of mode f_c by creation of an exciton of wave vector $\mathbf{K}_c \pm \mathbf{q}$. If stimulated exciton emission overcomes induced exciton absorption, a net gain is achieved for the excitonic field. In the context of excitonic transport, stimulated exciton scattering induced by a traveling excitonic field (f_c, E_c, $\mathbf{K}_c$) leads to its amplification.

Normally when one thinks of a laser and gain from stimulated emission it is assumed that the system must have a population inversion; Imamoglu *et al* have shown that this is not necessary for an exciton laser when the photon character vanishes (no participation of radiation) [26]. In fact these authors note that stimulated emission can be observed at densities lower than those required for condensation provided that the exciton reservoir be kept far from thermal equilibrium.

2 Experiment

This chapter will present a detailed description of the equipment, sample preparation procedures, data acquisition methods, cryogenic and optical setups required for the successful realization of our Bose-Einstein condensation experiments in Cu_2O.

2.1 Laser Beams

Four different kinds of lasers were used in our experiments: a frequency doubled pulsed (δt = 10 nsec) Nd:YAG at λ = 532 nm, a pulsed (δt = 8 nsec) dye laser pumped by the YAG producing a tunable output in the visible wavelengths, a CW Ar^+ gas laser with output at 488 nm and 514.5 nm and a CW dye laser pumped by the Ar^+ also producing a tunable output in the visible spectrum. The peak output power of the pulsed lasers was about 15 MW and 3 MW respectively, the maximum output power of the CW lasers was about 2.6 W and 0.5 W respectively. To accurately calibrate the intensity of the light striking the sample, a diaphragm the same size as the one covering the sample was placed at the sample position and the average power exiting the aperture measured using a calibrated power meter. The intensity (normally in units of W/cm^2) of a CW beam is the average power divided by the aperture area. The peak intensity of a pulsed laser is related to the average power (or vice-versa) by

$$I = \frac{P_{avg}}{A f \delta t} \tag{32}$$

where f is the repetition rate, A the illuminated area and δt the temporal pulse width (generally the FWHM). To simplify exciton density calculations, we usually assume that the peak intensity as defined by Eq. (32) can also be regarded as the average intensity during a square pulse with duration δt.

The intensity profile of a laser beam varies approximately like a Gaussian; however in our calculations the intensity is assumed to be constant across the beam. Our approximation is valid since the spatial extent of the laser beams at the sample position was generally much larger than the aperture so that the intensity drop off from center to edge was typically less than 30%. This means the intensity on axis was slightly larger than what is calculated using Eq. (32) and slightly less near the edge of the aperture.

2.1.1 Laser Attenuation

In order to vary the exciton density a means of precisely changing the laser intensity was required. The intensity of most lasers can not be easily varied at the source without affected the beam quality, pulse duration, wavelength calibration etc. Therefore an external method using different kinds of attenuating filters is generally used.

CW laser beams generally have a relatively low intensity and front surface attenuation filters can be used. This type of filter consists of a reflective metallic coating on a glass substrate. However, the high peak powers of a pulsed laser would vaporize the metallic coating. Consequently volume absorbing neutral density filters were used to attenuate the pulsed beams. Standard filters come in optical densities of 0.05 (normal glass), 0.1, 0.2, 0.3, 0.5, 1 and 2. Optical density is related to attenuation by

$$I = I_o \cdot 10^{-OD} \tag{33}$$

where I_o is the incident intensity, OD is the optical density and I is the transmitted intensity. Intermediate optical densities are achieved by using combinations of filters i.e. to attenuate a factor of 4, two $OD = 0.3$ ($10^{-0.3}$ x $10^{-0.3}$ = 0.5 x 0.5 = 0.25) filters are used. An attenuation as great as 10^{-5} was sometimes necessary, this was achieved by stacking several filters in series reducing the intensity gradually thereby reducing the risk of burning a filter.

One of the disadvantages of neutral density filters is that they slightly deviate the beam. This is because the two faces are cut to a slight wedge to reduce etalon effects. Also slight deviations from the rated optical density can compound as many filters are stacked in series, and keeping track of many filters becomes difficult and error prone. Furthermore the optical density varies slightly as a function of wavelength.

2.1.2 Quadruple Quartz Wedge Attenuator

A quadruple quartz wedge attenuator solves these problems, the beam deviation is on the order of microradians (as opposed to centiradians), the optical density is repeatable and precise to less than 0.05 OD and the attenuator can be controlled by computer. In addition the damage threshold is that of quartz (> 3 J/cm^2), a very robust optical material. The accuracy of the device is limited by its calibration which in turn is limited by time, laser instability and mechanical flexure in the gear system. The useful dynamic range is on the order of 2.5 OD and this is limited by the gearing and the

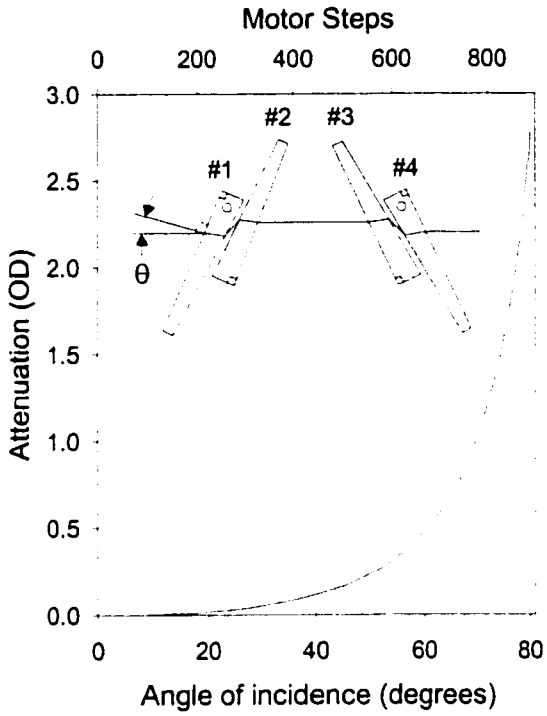

Fig. 7 Attenuation in optical density as a function rotation angle of quartz wedges.

resolution of the driving stepper motor. The device can be calibrated for any wavelength in the visible to near infrared.

The device is based on the Fresnel reflection equation for polarized light. A quartz wedge absorbs a negligible amount of light in the region of interest so light is either transmitted or reflected, the amount transmitted is a function of the incident beam angle [27]. Two pairs of quartz wedges are set on two counter-rotating tables, the beam deviation produced by the first wedge is canceled by the second wedge, and the beam offset introduced by the first wedge pair is canceled by the second wedge pair (see inset of Fig. 7). A stepper motor (Slosyn model MO61-CE08) rotates the tables through a series of reduction gears. A stepper motor is used since a computer can command the motor to move a predetermined number of steps.

In theory the attenuation as a function of plate angle and beam wavelength can be calculated exactly but in practice the measured optical density differs somewhat especially at high attenuation levels. This may be due to beam divergence, residual orthogonal polarization or nonlinear effects in the index of refraction of quartz at high intensity. A computer program subroutine calibrates the device by measuring the intensity throughput with a power meter as a function of stepper motor step angle. The effective *OD* at each motor position (an example is shown in Fig. 7) is then calculated and saved to a file. To slew to a desired *OD* a lookup table based on the calibration file and linear interpolation is used to translate the requested *OD* into motor steps by finding the closest matching OD that corresponds to an integer number of motor steps, and the motor is stepped to the new position. The calibration and slew routines with accompanying user interface are built into the program TEK.

The initial alignment of the devices must be precise if a large (> 1.5 *OD*) dynamic range is required. The laser beam must be centered on the entrance slit and perpendicular to the housing so as to clear the exit slit. Furthermore the two pairs of wedges must be set to parallel to each other to define the zero point. Beam centering is not crucial if the beam is smaller than the slits, however a large beam should be well centered to have maximum throughput. The orthogonality of the beam and parallelism of the wedges is crucial and must be verified by observing the reflections of the incident beam on a distant surface, the farther the surface the more accurate the calibration will be, however a few meters should suffice. The first quartz wedge will produce two reflections, front surface and rear surface, these will be separated by a little more than the wedge angle (1°). The second wedge produces indistinguishable reflections from the first wedge since its surfaces are parallel to the first wedges inverse surfaces (i.e. #1 front || #2 back, #1 back || #2 front). The reflections from the third and fourth wedges (i.e. the second pair) should ideally be collinear with the first pair when $\theta = 0°$ but the manufacturer (Newport Research Company) tilted the first pair vertically by +1.3° and the second pair by -1.3°, allowing the user to distinguish the reflections. The small tilt has no impact on performance. When perfectly aligned four laser spots should be observed, one pair horizontally separated by 1°, 1.3° above the incident beam virtual axis and an identical pair 1.3° below the axis. The spots from the front surface of the first and third wedges should be vertically aligned with the beam axis (i.e. surfaces normal to the beam axis). Consequently the spots from the back surface of the first and third wedges should be respectively to the left and to the right of the beam axis (if the inset of Fig. 7 is a top view, the spot from wedge #1 would be to the right). A small displacement of the motor will send the top pair of spots in one direction and to other pair in the opposite direction since the two tables are counter-rotating. The spots quickly disappear if the tables are rotated too far since they cannot exit the entrance slit, removing the cover will obviously aid initially finding the spots.

The original device as sold was equipped with a simple knob to adjust the table orientation. This was woefully inadequate since turning the knob through most of the range would produce little attenuation, then a small fraction of the last turn had an enormous effect (see Fig. 7). Settings could not be accurately repeated due to the critical

angular dependence and calibration was very difficult due to the nonlinear response. The only way the device could be rendered functional was by attaching a stepper motor a using a computer to calibrate and linearize the response curve.

The stepper motor is fixed to the exterior of the housing and is attached to a shaft which drives a series of reduction gears (total reduction is 10 times) inside the attenuator housing. The stepper has a fixed resolution of 200 steps/rev but can be operated in half-step mode giving 400 steps/rev at reduced torque. Since the load is very small in this application, low-torque induced stall is never an issue. The stepper motor coils are modulated by a driver circuit which accepts TTL inputs from a computer and is wired to a DC power supply. The driver circuit (Slosyn model 230T), AC/DC transformer, voltage regulator circuit and external connectors are all built into a single project box. A nine lead wire links the box to the motor, and a five lead wire links the box to the parallel port of a computer. The motor cable has a positive and negative for each of the four coils and one spare lead. A specially designed switch in the control box allows the user to toggle from a parallel to serial motor connection. The parallel connection has a reduced maximum torque but a flatter torque vs. rotation speed curve, the series connection was used in this application.

The computer cable has direction (CW/CCW), step mode (full/half), all windings off (AWO), pulse and ground leads. The first three must be kept in the correct state at all times; the pulse lead is activated to command the driver circuit to move the motor one (full or half) step in the (CW or CCW) direction. The AWO lead instructs the driver circuit to power down the coils allowing the user to spin the motor freely. The leads are connected to four of the computer's parallel data ports, a second motor can use the remaining four ports.

To drive the motor by computer this simple algorithm was implemented in the program TEK:

```
'Part of subroutine MoveMotor in program TEK
'All variables and constants are integers
CONST cpus, cpus2              'these depend on CPU speed

Get #filenumber, 1, posi       'Get old position
dist = finalpos - posi         'Number of steps to move

' bit=0 means pin is held low (low = 0 Volts = active)
```

```
' bit=1 means pin is held high (high = 4.9 Volts = inactive)
'PU = 1          triggers on upward slope, dataport 0
'CW = 2          CCW if bit is zero,              dataport 1
'halfstep = 4    fullstep if bit is zero,         dataport 2
'AWON = 8        AWOFF if bit is zero,            dataport 3

'Code for setup of wordon and wordoff bits omitted

'Following loop will generate a square wave with dist cycles
For i = 1 To Abs(dist)
     vbOUTw lptdataport, wordoff     'Set pin ready
     For z = 1 To cpus: Next         'Wait
     vbOUTw lptdataport, wordon      'Trigger step
For z = 1 To cpus2: Next             'Wait
Next
vbOUTw lptdataport, wordoff          'Reset pin
Put #filenumber, 1, finalpos         'Store new position
```

The statement: vbOUTw *port, value* sends the word: *value* to the machine address: *port.* In this case the machine address is the parallel port *lptdataport* (usually = &H378 for LPT1) and the first bit of the word sent is toggled off and on in *wordoff* (usually = 4 + 8 = 12) and *wordon* (usually = 1 + 4 + 8 = 13) to generate a square wave. The square wave has a duration of *dist* periods, moving the motor *dist* motor steps.

When turning the computer on an uncounted pulse will occur if the motor control box is on since the computer sets all ports high on startup. In addition turning the power on or off to the stepper motor will cause a random (in direction and magnitude but usually less than a full step) move of the motor. This is an unfortunate property of stepper motors due to the way the coils are energized. The only solution to these two problems is to turn the motor control box off when turning the computer on or off (to reduce the systematic uncounted step), and to reset the zero point each time the power to the motor control box has been interrupted. In practice this is not a great issue since a calibration is done before each experiment.

2.1.3 CR599 Dye Laser Alignment and Calibration

The CW laser used in the experiments was a Coherent CR599 dye laser pumped by a Coherent Innova 70 Ar^+ gas laser in multiline mode. The CR599 uses a high pressure laminar jet of dye solution crossing through the pump beam to produce laser light in the yellow to red spectral range. The dye solution consisted of R6G (sometimes called Rhodamin 590) powder diluted in reagent grade ethylene glycol. The dye concentration

stated in the user manual (2 to 3 g/L) was found to be too high to obtain maximum efficiency. Starting with 0.75 g of powder (dissolved first in 50 ml of methanol) in 1 L of ethylene glycol and adding small amounts of a concentrated solution (0.25 g dissolved in 50 ml of methanol) a maximum efficiency was reached at about 1 g/L.

Before aligning the cavity great care should be taken in aligning the dye jet and catcher tube even at the expense of slight leakage from the catcher tube. If misaligned the jet will produce bubbles in the solution which greatly reduce the output stability. Since the dye solution should be replaced about once a year, a small leak is not detrimental to the operation of the laser. The pump beam should strike near the very top of the pump mirror so that luminescence intercepted by the full reflector mirror will clear the pump mirror and it's mount. While aligning the cavity the luminescence spots originating from the jet and projected onto the ceiling should be carefully observed; for good efficiency they should be equal in intensity, side by side and at their *minimum* intensity. The output beam mode can be varied by tilting the full reflecting end mirror or by translating the focus of the pump mirror in the dye jet. Maximum efficiency was obtained when the beam shape was a single vertically elongated ellipse (aspect ratio about 1.5), this was assumed to be the TEM_{00} mode for this laser. Final tweaking should be done using the partially reflecting end mirror, although adjustments made to the pump mirror orientation are the most sensitive and consequently the most common.

The maximum efficiency ever attained was on the order of 18% (470 mW for 2.6 W multiline Ar^+ input), this value dropped to 16% after some time, probably due to some mechanical flexure of some of the components and reduction in the dye efficiency. Changes in the output power can be significant in the first 20 minutes or so of use, simply due to the laser housing heating up, therefore precise adjustments done in this time period may be for not as the laser will housing will soon find a new equilibrium.

The dye output power is a function of wavelength, a typical response curve for the R6G dye solution is shown in Fig. 8. The FWHM of the laser line, as seen in the inset, is always on the order of 0.2 nm when using the single plate birefringent filter in the laser cavity; however the line is not quite symmetric, showing a slight bulge on the short wavelength side. The width of the laser line is nearly constant over the entire gain region, changing by only about 10%. The calibration for the micrometer screw which rotates the

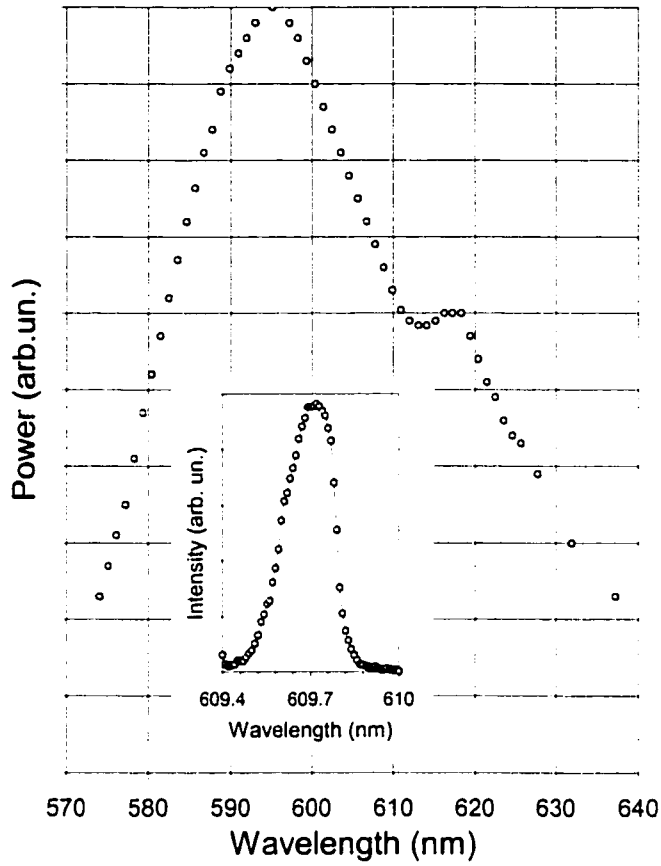

Fig. 8 CR590 dye laser (with R6G dye solution) output power as a function of output wavelength. Inset shows CR590 line width (spectrometer resolution ~ 0.04 nm).

birefringent filter is sensitive to the alignment of the cavity, the pump power and the jet pressure. For an approximate conversion from micrometer screw setting (x in μm) to wavelength (λ in nm) use the equation: $\lambda = 0.21x + 474$, the conversion should be accurate to less than a nanometer.

2.2 Exciton Detector

2.2.1 Exciton Mediated Photovoltaic Effect

Due to the extremely low radiative efficiency of paraexcitons in Cu_2O the detection of these particles by luminescence techniques is very difficult, therefore a non-optical method was required to locally detect the excitons. The method we have refined is based on the exciton mediated photovoltaic effect [28]. The exciton mediated photovoltaic effect was originally used by solar cell researchers for converting light into an electrical current [29]. The original "sandwich" type detector developed to gather as many of the excitons in the crystal as possible has been slightly modified to become a local exciton detector which could be used in a time resolved type of measurement as seen below.

Figure 9 demonstrates the basic idea behind the original method. The Cu_2O sample (a p-type semiconductor) is sandwiched between a semi-transparent Au electrode on the left and a Cu electrode on the right. The gold provides an ohmic contact for Cu_2O. An ohmic contact can pass very large currents with only a small voltage drop across the metal-semiconductor junction. The Cu contact on the other hand is a rectifying contact: at the Cu/Cu_2O interface the respective Fermi energy levels line up and lead to a bending of the energy bands of the semiconductor. The potential barrier, ϕ_B at the interface is of the order of 1 volt [30, 31]. This results in a high electric field region W (where W is the depletion width) in the Cu_2O crystal which extends to a depth of 10-100 nm [32]. The local static electric field will thus have a magnitude of $\phi_B/W \sim 10^5$-10^6 V/cm. The field required to dissociate an exciton in Cu_2O is of the order $E_b/(r_{exc}e) \sim 10^6$ V/cm where E_b is the exciton binding energy and r_{exc} is the exciton radius. Therefore a fraction of the

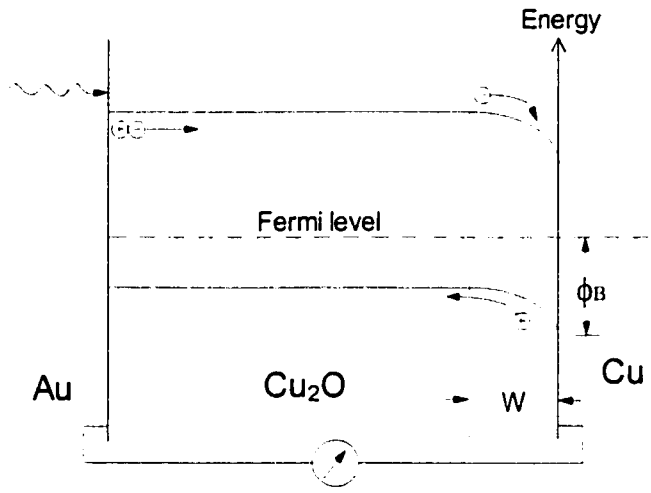

Fig. 9 Solar cell electrode arrangement. Excitons optically created in the crystal volume diffuse to the Cu/Cu_2O interface where they are dissociated by the local field and collected a free electrons and holes.

excitons reaching the Cu/Cu_2O interface will be dissociated and detected as an external current (small external resistance) or voltage (large external resistance) between the Au and Cu electrodes.

For multimegawatt / cm^2 pulsed illumination and time resolved measurements needed for Bose-Einstein condensation and exciton transport studies, the sandwich electrode arrangement of Fig. 9 is unsuitable. Firstly, the high intensity laser beam would damage the semi-transparent Au electrode. Secondly, the extremely high series impedance of the thick (a few millimeters) Cu_2O sample at low temperatures ($\sim 10^9$ Ω) together with various distributed capacities would result in relatively high time constants for the detected signal, preventing the nanosecond resolution required for the time resolved experiment. Thus most of the time resolved high intensity studies were made with the modified arrangement shown in Fig. 10 where the Au electrode (single cross-hatch) is deposited on the same face as the Cu electrode (double cross-hatch), opposite the illuminated area (of equal surface as the Cu electrode) as depicted by the dotted circle on the left side of the crystal. The active detector region is the 10-100 nm thick volume of Cu_2O under the thin 50 nm Cu film, the total detector area is ~ 0.03 cm^2 (2 mm diameter). The impedance of the detector will be determined by the separation between the Cu and Au electrodes, which in this case is much less than in the solar cell arrangement. The crystal itself acts as light filter blocking most of the light from reaching the active region (which would create excitons directly in the depletion width) and only measures exciton that have traveled from the front face after a delay corresponding to their transit time. A few early measurements were

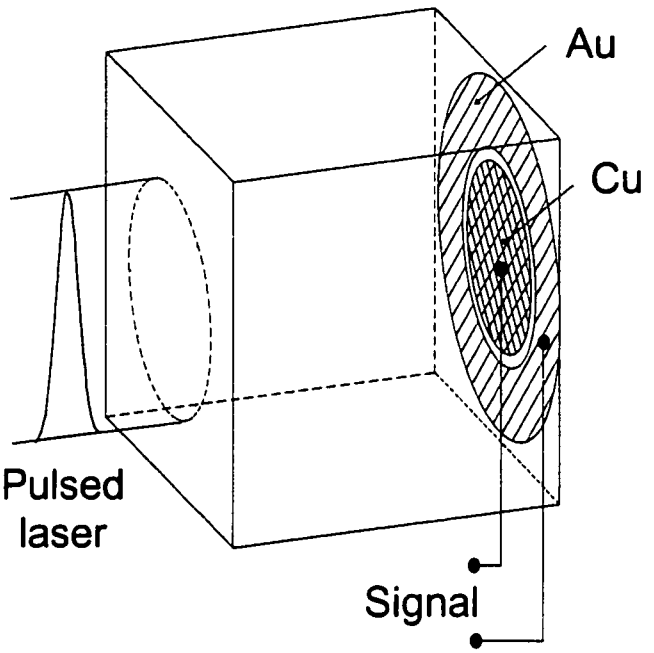

Fig. 10 Electrode arrangement used for high intensity time resolved measurements.

performed using an interlocking finger type electrode (an example can be seen in Fig. 12 in Sec. 2.3). But due to ease of fabrication (especially attaching the wire contacts see Sec. 2.3.4), slightly higher signal strength and better symmetry with the cylindrical exciton cloud, the interlocking finger electrode design was dropped in favor of the ring design.

2.2.2 Detector Response

The detector linearity and response time were verified for the circular electrode arrangement at liquid helium temperatures by directly illuminating the electrode face with laser light. The wavelength of the light was 532 nm so that the photons would be absorbed close to the surface creating excitons directly in the depletion layer avoiding effects due to exciton transport. The impedance of the measuring device (a digital oscilloscope) was set to 50 Ω, the same used in all the time resolved experiments. The results shown in Fig. 11 confirm the detector linearity from fractions of a mV up to several dozen mV, these signal intensities are the same order of magnitude as the measured excitonic signals to be introduced later. A typical time resolved trace is shown in the inset, the FWHM is 14 nsec, close to the rated laser pulse duration of 10 nsec which was independently verified using a high speed photodiode (fall time < 1 nsec).

The magnitude of the signal gives an indication of the maximum efficiency of the exciton detector. The laser beam was as large as the Au electrode, but the light striking deposited Au or Cu was reflected since the electrode layers were very thick (an advantage of this configuration is that the Au can be thick making it more robust and opaque). The amount of photons contributing to the signal is then proportional to the exposed Cu_2O

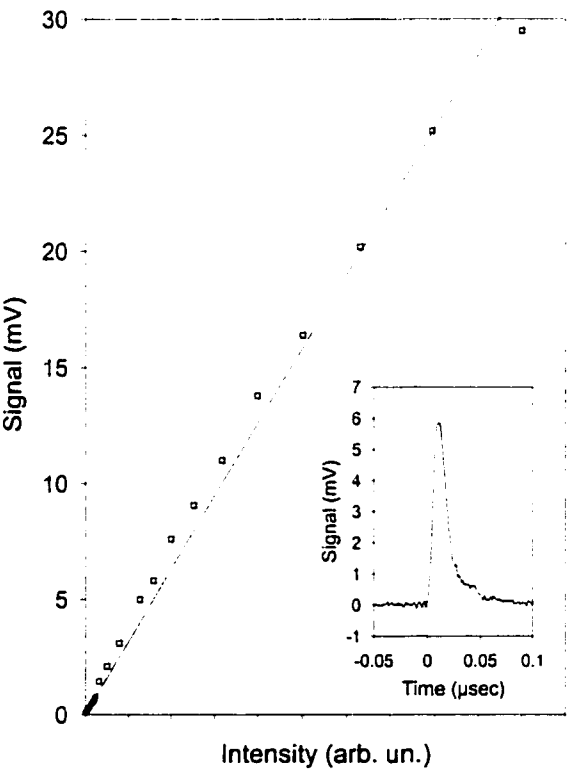

Fig. 11 Detector response as a function of incident intensity at T = 2K. The solid line is a linear fit. Inset shows typical time resolved trace of laser pulse.

surface between the electrodes. The input energy is the number of photons striking the Cu_2O surface times the energy per photon; the output energy is the electrical output power times the pulse duration. An efficiency on the order of 1% was calculated in this configuration. This would be a maximum efficiency for this detector since the light is deposited directly between the Cu and Au electrodes and the distance the free charges must travel is minimized. The time resolved signals presented later will be from excitons that are mostly dissociated near the center of the Cu electrode (underneath the electrode) and need to travel on average a much greater distance than in the above configuration, lowering the overall efficiency. By illuminating the face opposite the electrodes with weakly absorbed light and creating excitons in the depletion width underneath the electrode we have approximated the time resolved configuration, without the exciton transport component, and an efficiency of 0.1% was estimated for this method. These two results are in order of magnitude agreement with values obtained (1% to 0.1%) by solar cell researchers [33].

The magnitude of the signal will vary from sample to sample, and even for the same sample prepared at different times due to variations in crystal quality, surface preparation, electrode placement, wire bond quality and Cu electrode oxidation. Such large number of variables (some due to our limited facilities, others inherent in the material) makes the absolute calibration of the signal magnitude very difficult.

2.3 Sample Preparation

Since preparation of the samples required polishing and chemical etching, the thickness of the samples varied from experiment to experiment. We had four high quality natural growth single crystal samples available for our experiments although #3 could only be used for a short time before it had to be returned. All the crystals were cut into parallelepipeds and oriented along the <100> direction by a crystallographer. Sample 1 had an original size of 3.56 x 4 x 4 (all lengths in millimeters) and was the highest quality sample of the four. It was used the most often, providing the bulk of the results presented in this work (at a thickness of 2.2 mm); its current size is 1.97 x 3.8 x 3.8. Sample 2 had an original size of 3.74 x 4 x 4 and is currently 2.5 mm thick. Samples 3 and 4 were substantially larger than the first two, 11 x 10 x 8.3 and 8 x 6 x 5 and were only used once. Sample 3 had a single defect area which was easily avoided in our transport experiments. Sample 4 had numerous defects but fortunately had a single long column (in the 8 mm direction) of mostly defect free volume in which the experiments were performed. All of the samples originated from a mine in Namibia.

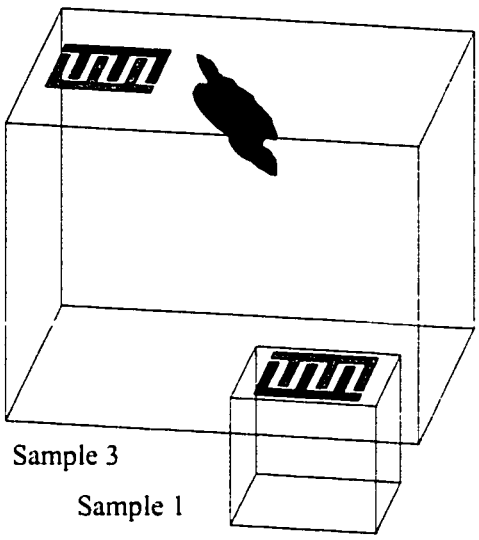

Fig. 12 Comparative sizes of samples 1 and 3 with first generation interlocking finger electrodes.

2.3.1 Polishing

The first step in the sample preparation was the polishing, performed in the Department of Geology facilities. Polishing is carried out to remove any scratches, previous electrodes or epoxy from the surface of the crystal. If large scratches are not removed they will be further enlarged and deepened by the chemical etch performed afterwards, due to the anisotropic etching rate. The following polishing recipe (it is not the only method) produces good results, although the quality can vary substantially with operator skill and experience. Note that the times shown (per face) can also vary substantially due to the polishers experience, the amount of pressure exerted or if the preceding step is not properly completed.

Table 1: Polishing procedure

1	9.5 μm Al_2O_3 powder on glass sheet with distilled water for ~1 min, longer if epoxy and/or electrodes must be removed. Rinse with distilled water/methanol solution in ultrasonic cleaner. Wipe dry with tissue paper. N.B. This step removes by far the most amount of material from the crystal, therefore one must be wary of polishing for too long, but all of the epoxy and/or electrodes *must* be removed.
2	1 μm diamond paste on Microcloth with polishing fluid for ~15 min. Rinse with distilled water/methanol solution in ultrasonic cleaner. Carefully touch dry with optical tissue paper.
3	0 to 1 μm crushed diamond powder on Microcloth with no lubricant ~1 min. Rinse with distilled water/methanol solution in ultrasonic cleaner. Carefully touch dry with optical tissue paper.

All the polishing was done without any type of special holder, the sample is held between two fingers or under a single finger when it is too small. The last two steps are performed on an adjustable speed turntable. A higher angular turntable speed along with placing the sample near the edge of the turntable reduces the polishing time but requires more dexterity to keep the sample from being flung out of the operators fingers. The maximum manageable turntable speed increases with operator skill. It is very important to clean the sample, hands and tweezers before every step to avoid contamination of a fine powder with a coarser one. Note that it is a good idea to stop every few minutes to rinse, dry and observe the sample through a microscope to see if it is time to proceed to the next step. Knowing when to change powders is more an art than a science, but by using a microscope one can tell when the scratches and dimples in the surface are as small as possible, and further polishing with the same powder would yield little improvement. When finished, all the surfaces were reflective and flat. Minor craters (< 1 μm) remained but these seemed intrinsic to all the crystals since if the small craters were polished away, others were uncovered somewhere else on the surface.

2.3.2 Chemical Etching

Chemical etching was performed on the sample to eliminate the top atomic layers which may have been damaged during polishing. In addition the electrodes deposited afterwards could easily be scratched off by the wire contacts if no etching was performed. The following recipe developed by solar cell researchers has been found to lower the surface recombination rate and maximize the barrier field at the Cu/Cu_2O interface [34].

Table 2: Etching procedure

1	Rinse in distilled water.
2	Soak for 1 min. in methanol with final 20 sec in ultrasonic cleaner.
3	Etch for 3 min. in HBF_4 (~5 μm/min), then dilute quickly with distilled water so that there are no spots etched more than others.
4	Repeat steps 1 to 3 if electrodes are still present from a previous experiment.
5	Repeat step 1 and 2.
6	Soak for 90 sec in Bromine(2% vol.)/Methanol solution with final 30 sec in ultrasonic cleaner.
7	Repeat step 2 and 6.
8	Repeat step 2 and 1.
9	Quickly blow dry with He or N_2 to eliminate water spots.

2.3.3 Electrode Deposition

To dissociate the excitons into electron hole pairs and inject them into an external circuit to measure a voltage, Au and Cu electrodes as shown in Figs. 10 and 12 were deposited on the polished face of the crystal. Since the crystals are relatively small (for human manipulation), and the electrodes even more so, the evaporation mask design needed special consideration in order to deposit the electrodes without overlapping them and causing a short circuit.

Two types of masks were used, a finger pattern mask shown in Fig. 13 made by laser lithography at the National Research Council in Ottawa and the circular pattern

mask (Fig. 14) made by the Physics machine shop. Both masks are designed to consistently deposit two different materials within 250 μm (or less) of each other, on an area less than 4 mm by 4 mm square. The four guide posts embedded in the mask holder also shown in Fig. 13 are placed so that when the finger pattern mask is rotated 180°, the second electrode interlocks with the first electrode. The procedure to deposit the finger pattern electrodes is as follows: the crystal is placed in the center of the holder and held by Teflon screws. The edges of the crystal are then lined up with two marks on the mask to position the crystal exactly by adjusting the Teflon screws. Also the surface of the crystal is aligned to be flush with the surface of the holder so that there is a minimum of space between the mask and the crystal. This ensures that even if the sample is not exactly over the evaporator source, the electrode will not shift due to the angle. The first evaporation using Au is carried out and the mask holder is removed from the evaporator. The mask is removed and replaced rotated 180°; this must be done carefully so as to not move the sample and ruin the alignment. The sample is once again placed into the evaporator and the Cu electrode is evaporated.

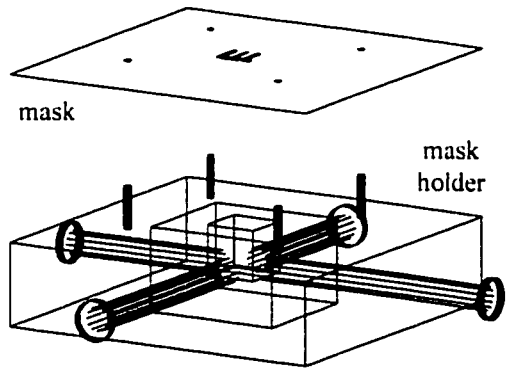

Fig. 13 Mask (finger type) and mask holder for electrode deposition.

Both the Au and Cu electrodes were evaporated to about the same thickness, 80 to 100 nm. The films must be thick enough to prevent diffusion of the epoxy (Sec. 2.3.4) through the electrode and into the Cu_2O forming another photovoltaic barrier. Also the Cu tends to diffuse into the Cu_2O over time, eventually erasing the electrode and thin Au electrodes easily peel off from thermal cycling or handling.

The order in which the materials are evaporated can be important: evaporating Au then Cu reduces the exposure of the Cu/Cu_2O interface to heat, which chemically oxidizes to form a non-conducting layer of CuO between them, which in turn reduces the barrier height and efficiency of the exciton detector.

The same procedure is followed for the circular electrodes except that three evaporations are performed. The outer Au ring is deposited first, then the mask is rotated 180° and a second Au ring is deposited over the first. The second evaporation has the

effect of covering the blind spots produced by the three symmetrical center supports and producing a complete ring. Note that for the second evaporation a circular mask with a radius slightly larger than the circular center section of the mask in Fig. 14b is placed over the center section to nullify any misalignment. The final evaporation of the center spot using Cu is performed with the mask in Fig 14a in place.

As mentioned earlier the ring type electrodes have been used in all the recent

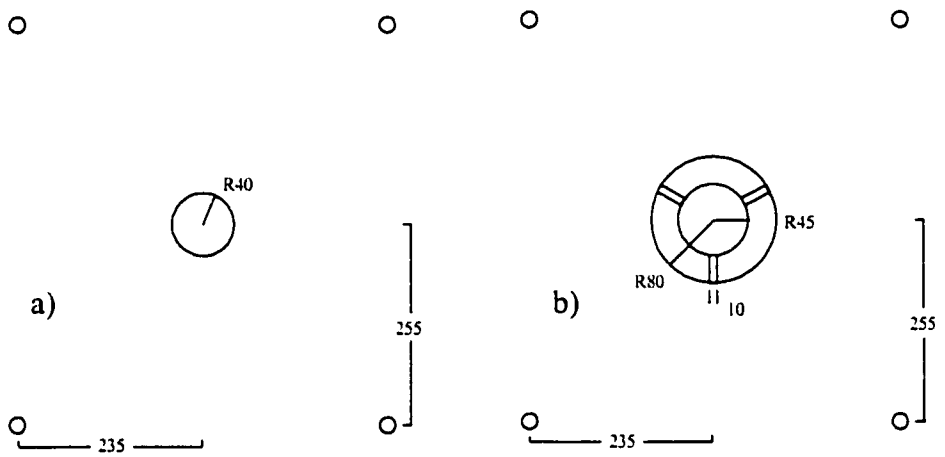

Fig. 14 Masks used for circular electrode evaporations. a) Cu electrode, b) Au electrode. The four outer holes match the posts on the mask holder. Dimensions are thousands of an inch and the R denotes a radial dimension.

experiments for several reasons. Firstly it has the same symmetry as the exciton cloud created by optical pumping, secondly more of the Cu is in the center of the sample where the excitons are expected to arrive, and thirdly the much wider area (1 to 2 mm width as compared to 0.5 mm for the interlocking finger configuration) made attaching the wire contacts much easier.

2.3.4 Wire Contacts

The most difficult part of the sample preparation was making a good bond between small gauge Au wires (referred to as contacts) and the electrodes. The bond must be able to withstand an extreme change in temperature (from 300 K to 2 K) and hence differential thermal contraction. Several attempts were made with Silverprint, a type of conductive paint used for printed circuits, but after a few thermal cycles, the bond became very brittle and was likely to fail. Two different two-part epoxies, Epo-Tek 20E and Epo-Tek 415G, were initially tested. The 20E easily survived many thermal cycles.

However this type of epoxy must be cured at 200 °C for 5 minutes, and in this short time a substantial layer of CuO forms between the Cu/Cu_2O interface, greatly reducing the detector efficiency. Furthermore the bond is so strong that a part of the crystal can be broken off when attempting to remove the epoxy. The Epo-Tek 415G cures at room temperature but could not withstand the low temperature stresses and has never survived a thermal cycle. Another fastener called Circuitworks a compound similar to Silverprint, manufactured for the same purpose but with a thicker consistency when applied, and not as brittle once dry, was used and produced inconsistent results. It sometimes survived many thermal cycles then none at all. The epoxy currently in use: Epo-Tek 410E is the best we have tried so far. It cures at room temperature over a few days, has enough viscosity so as not to leak while being applied but not to much so that it spreads well, and most importantly it survives thermal cycling.

The diameter of the wire contacts is very important, since larger wires strain the bond much more due to their larger spring constant, and wires that are too small are difficult to solder solidly to the vacuum feedthroughs (see Sec 2.3.5) . The wire could be fixed to the feedthrough with epoxy but a solid solder is much stronger and less electrically noisy than almost any epoxy or mechanical contact. The wire material can be any conductor, however Au and Cu are among the best due to their low resistivity and general availability. The sample holder is made of Cu so that differential thermal contraction between Cu wires and the sample holder should be near zero seemingly making Cu the material of choice. However most Cu wire must be stripped of a non-conducting coating before being used and can oxidize afterwards, they are also more difficult to solder than the Au wires. We found that a Au wire with a 50 μm diameter to be the best compromise.

The following method for bonding the contacts to the electrodes using only a steady hand and magnifying glass was perfected over several years and was found to be consistently successful. Before bonding the contacts make sure the sample holder (Sec. 2.3.5) is securely fastened to the cryostat rod and the wires leading from the coaxial connector at the top of the rod down to the sample holder are soldered to the vacuum feedthroughs. The sample should also be well seated in the sample holder in the correct

orientation so that it is flat against the bottom and snug against the holder walls, extra space around the sample may be filled with Teflon tape.

Table 3: Epoxy application

1	Set sample in sample holder in correct orientation
2	Solder Au wires to vacuum feedthroughs
3	Cut wires to correct length and make a small foot on free end
4	Bend wire into shape so that foot of wire is in correct position with tension pressing foot down slightly
5	Dip a tool (scrap piece of wire) in epoxy to have a small chunk of epoxy on one end
6	Use tool to bring epoxy to foot on sample surface and repeat if necessary

The amount of epoxy needed on the end of the tool can be judged by practicing several times on a microscope slide. The epoxy bond will always be delicate since a heat cured epoxy cannot be used, a bond that has survived many thermal cycles and that can support the weight of the sample is rare.

The epoxy must be removed by polishing if it does not come off by thermal cycling. Small remnants of epoxy can be sometimes removed by methanol and cotton swabs; however the Au electrode is also easily removed with this method. The Cu electrode is generally much more robust and requires etching and/or polishing for complete removal since the Cu atoms actually diffuse into the crystal and form chemical bonds [31].

2.3.5 Sample Holder

The purpose of the sample holder is to solidly grip the sample (without applying too much force) in the cryostat at liquid helium temperatures, provide a good thermal contact to the low temperature bath, delineate the surface area on the opposite face from the electrodes to be illuminated by the laser beam, hide the electrodes from direct illumination, and to serve as a wire panel for the delicate wire contacts described in the previous section. In all six different sample holders with three distinct generations were fabricated for the four samples. Two holders representing generations one and two are shown in Fig. 15.

Three first generation holders for samples 1, 2 and 3 (shown in Fig. 15a) were made from Delrin, a black plastic, to electrically insulate the sample from the cryostat. On one side of the holder an approximately 4 mm square by 2 mm deep hole was machined to hold the sample (in the case of samples 1 and 2). In this hole another cylinder 3 mm in diameter by 2 mm deep was drilled to allow large cross section of He to be in contact with the sample. Next a 2 mm diameter hole was drilled straight through for laser beam access. The smallest diameter hole selects only the center of the beam, so that the variation of the intensity as a function of radius is no more than 30% as mentioned in Sec. 2.1. A rectangular light cap was fitted over the sample on the holder face opposite the illuminated side to block stray light from hitting the electrodes. Two small funnels from the bottom of the holder allow He to enter the light cap interior. The "front cell" photovoltaic signal generated by the parasitic light scattered around the sample or coming through the cracks between the light cap and sample holder was useful in determining the time zero reference point. However, under certain conditions, stray light hitting the electrodes could, for an unknown reason, totally disable the detector.

A second generation holder for sample 1 shown in Fig 15b) (used afterwards with sample 2) was built to amend certain weaknesses of the original design. The light cap design was improved to minimize the parasitic light reaching the sample (some always

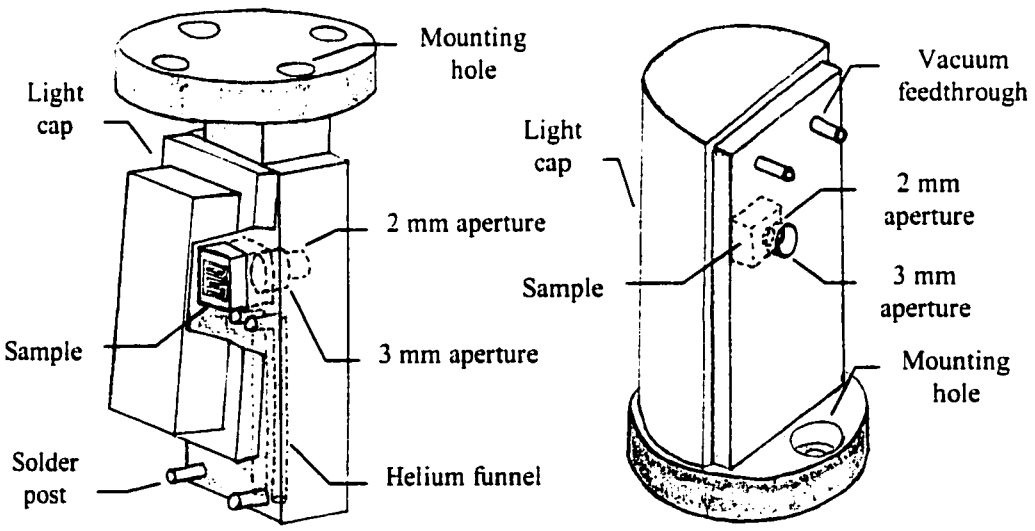

Fig. 15 a) 1st generation sample holder made from Delrin plastic, b) 2nd generation sample holder made from Cu.

gets through) and to completely contain the sample and solder posts. This way the Au wires from the electrodes to the solder posts were never disturbed during installation or removal of the light cap. The new solder posts were vacuum feedthroughs, a solid wire embedded in a non-conducting plastic cylinder. The feedthrough allows an electric current to pass through a metal barrier while keeping the current isolated from the barrier and also keeping the barrier vacuum or light tight. The order of the 2 mm and 3 mm holes was reversed to allow better access to the sample by non-normal laser beams such as those used in double beam experiments and to better delineate and position the beam on the sample surface.

Another important design change was to build the sample holder from Cu (the light cap was still made from Delrin). During some experiments it was found that the sample mounted in a Delrin holder had great difficulty reaching and/or keeping the He bath temperature in non-superfluid He (even with He funnel tubes), especially when illuminated by high intensity laser pulses. In fact with the very large sample 3 the light cap had to be completely removed to properly cool the sample. The reason for this is the low thermal conductivity of plastic (especially at low temperature) due to its amorphous structure. When enclosed by Delrin the sample could only dissipate heat through He gas or liquid flowing by the front face; Cu on the other hand is one of the best thermal conductors even at He temperatures and the entire sample holder could act as a heat sink. Our experiments showed that the sample could dissipate much more heat in the Cu holder, allowing experiments with simultaneous pulsed and CW laser illumination. The sample was not electrically insulated from the cryostat and this did not seem to be a problem for some time (sample impedance ~ 10^9 Ω, load impedance 50 Ω), although later on occasional odd behaviour of the room temperature DC test signal lead us to coat the Cu holders with an electrically isolating spray. Note that the two wires from the electrodes and the solder posts are isolated from each other, sample holder and the cryostat at all times by the vacuum feedthroughs.

The major design change of the third generation holder (two were built, for sample 1 and sample 4) was a reduction of the holder length and the addition of a side aperture. Applications for this secondary aperture will be described in Secs. 2.4.4 and 2.4.5. When the sample is immersed in He gas there is always some liquid He bubbling in the bottom

of the cryostat, sometimes the liquid would touch the sample causing temperature fluctuations and rendering some temperature ranges inaccessible due to instability. Reducing the sample holder length decreased the chance that the He liquid could touch the sample when operating in the He gas. The side aperture was 1 mm in diameter and centered on an orthogonal axis about 1 mm from the illuminated face through the approximate center of the sample. The small size of the aperture compared to the primary one is due to the small thickness of the crystal, about 2.2 mm when the holder was fabricated. A larger hole would let to much scattered light directly strike the electrodes.

Other improvements included relocating the feedthroughs from the bottom to the top of the holder, and adding funnels (bottom and top) for He to get into and out of the light cap enclosure. Moving the feedthroughs reduced the chance that the coaxial cable from the top of the sample rod down to the solder posts would get stuck in the cryostat rod access tube when removing the sample with liquid He in the cryostat.

2.4 Experimental Setup

2.4.1 Optical Cryostat and Temperature Control

All of the Bose-Einstein condensation experiments were performed with the sample immersed in very cold He gas or liquid in a cryostat, resulting in sample temperatures on the order of 2K to 10 K. Since our experiments required illuminating the sample we used an optical cryostat (Janis Research model 8CNDT) that had four window ports (each a pair of vacuum spaced fused quartz plates) giving optical access to the sample. To keep the sample temperature stable for long periods of time while illuminating it with laser light (hence heating the sample) and to change the sample temperature to a temperature other than liquid He temperature of 4.2K, some kind of active cooling/heating mechanism was required.

Our cryostat was equipped with two heaters, one below the sample on the optical chamber floor, the other above the sample on the cryostat rod. The bottom heater indirectly affects the sample temperature heating the He liquid entering the sample chamber which then forms a liquid or gas heat bath for the sample (if sufficiently heated the He liquid vaporizes). The top heater directly heats the sample by conduction through the cryostat rod to which the sample holder is fixed. The cryostat rod is an approximately 1 meter long Invar rod which is used to lower the sample into the cryostat holding it in position in the optical chamber. At the bottom is a cylindrical copper block to which the heater is mounted and the sample holder attached. At the top it has a cover forming a vacuum tight seal with the cryostat body and has provisions for passing wires (temperature sensors, electric heater power, sample signals) from the outside world into the ultra cold enclosed environment or vice versa.

Active cooling was achieved by pumping on the He liquid or gas out of the optical chamber, up the cryostat rod access tube and out of the cryostat. A higher pumping rate (proportional to pump tube cross section and pressure differential) results in a higher cooling rate. By controlling the pumping rate, heating rate and amount of He liquid entering the optical chamber the sample temperature could be controlled and stabilized. The amount of He entering the chamber is controlled by a needle valve, the source of some frustration since the very small opening would occasionally get blocked by frozen air. The heating rate was controlled by externally varying the current supplied to the two

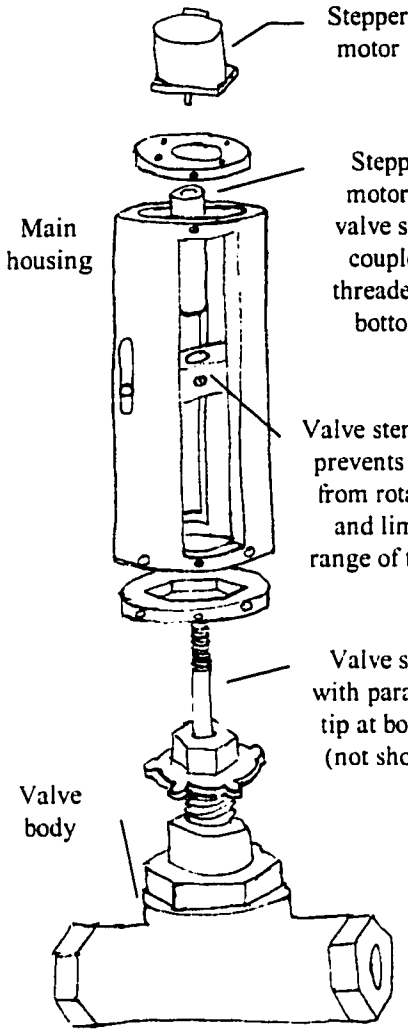

Fig. 16 Exploded view of stepper motor mounting and coupling to a parabolic all metal valve.

heaters. The pumping rate is varied by closing an external valve between the cryostat and the pump.

Early variable temperature results were obtained with a fairly coarse manually adjusted valve and achieving a stable temperature in some regimes was very difficult since fine and repeatable adjustments were very difficult to do. The small finite steps of a stepper motor translated into a linear motion by a screw, coupled to a high quality valve (Baumann Globe Valve model 24588) improved the temperature setability tremendously. The stepper motor mounting and motor to valve stem coupling as shown in Fig. 16 were designed by the author and built by the Physics machine shop. The new valve had a stem with parabolic tip which slid in the valve body in a direction perpendicular to the pipe. The parabolic tip ensures that open surface area increases linearly with the translation of the pin. A valve of this design must be fabricated to high tolerances to achieve a good seal because the valve body to stem tip contact is a metal on metal seal. The advantage of this design is that no rubber seals are exposed to low temperatures.

The same algorithm implemented to move the attenuator stepper was used to control the valve stepper since both motors and control boxes were identical. The user interface was integrated into the program TEK. The variation of the liquid temperature was found to be approximately linear as function of motor steps, decreasing as the valve opened. The gas temperature however decreased nearly exponentially and depended also on the heating rate (to transform the liquid He reserve into gas at the bottom of the

cryostat) and needle valve setting. The absolute temperature for a particular motor position varied too much from experiment to experiment, particularly in the gas phase, to attempt an absolute calibration but repeatability during a single experiment was very good.

Three regimes with overlapping temperatures ranges were accessible: superfluid He from about 2K to 2.17K, liquid He from 2.17K to 4.2K and gaseous He from about 2.2K to greater than 10K. Most of the experimental results presented in chapter 3 were performed in the superfluid with little or no variation in temperature and for many of these experiments the temperature is simply stated as 2K. In experiments where the temperature was varied the exact values were recorded.

In the liquid He phase bubbles scattering the laser light caused some effective attenuation; the bubble density and size in our cryostat are functions of temperature and hence the optical "transmission" is a function of liquid temperature as shown in Fig. 17. The effective attenuation was taken into account in the analysis where warranted. In the superfluid or gaseous He phase the He is very nearly invisible giving a transmission of one; in the superfluid phase this is mostly due to a thermal conductivity 10^6 times greater than in the gas or normal liquid phase. The unusually high thermal conductivity prevents the formation of bubbles since thermal instabilities from which the bubbles are produced are greatly suppressed. The high transmission of the gas is due to its low density as compared to the liquid phases. The largest bubbles and most violent bubbling, hence low transmission, occurs at temperatures just above the lambda transition; the bubbles instantly disappear when the temperature reaches the lambda point at 2.17K. Note that to cool the liquid the pumping

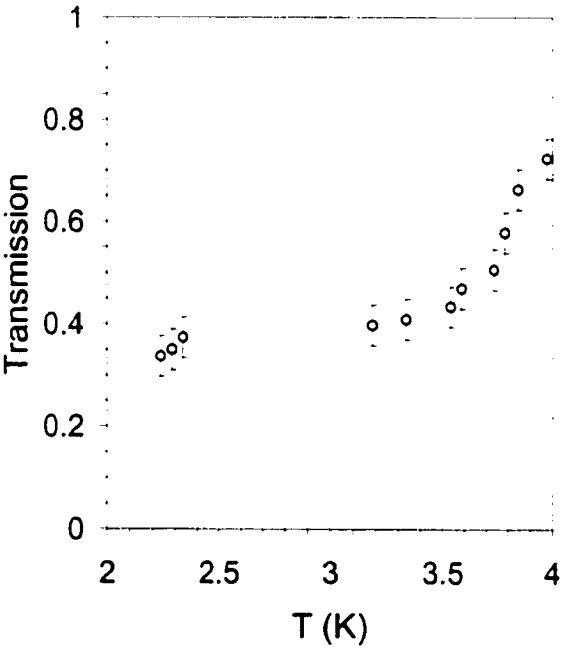

Fig. 17 Optical transmission through 2.5 cm of liquid He as a function liquid temperature. Superfluid and gaseous He have a transmission of 1.

rate was increased and this may have lead to a greater instability forming more bubbles as the temperature is lowered.

The temperature readings were supplied by two sensors, one mounted on the optical chamber floor, and another mounted on the copper cylinder on the end of the cryostat rod. The sensors are silicon diodes which have a temperature calibrated resistance. An external temperature controller (LakeShore Cryotronics model DRC 80C) sends small electrical pulses to the sensor and determines the resistance (which varies with temperature) which is then converted to a digital temperature reading by lookup table and interpolation and displayed on the controller front panel. The calibration can be verified by observing the lambda transition at 2.17K, the bubbles in the normal liquid suddenly disappear due to the tremendous increase in the thermal conductivity, and the He boiling point at 4.2K.

2.4.2 Data Acquisition

All of the time resolved data was recorded using a digitizing oscilloscope which averaged a trace over many laser pulses (typically 100 to 200 pulses). The oscilloscope was a Tektronics model 620b with a maximum sampling rate of 2 Gs/sec with 500 MHz bandwidth on two channels and two auxiliary 500 Ms/sec channels operating with 50 Ω impedance (therefore measuring current). The averaging is required to reduce the random background noise which can be at as large as the signal itself. A sampling rate of 500 Ms/sec was generally used since the oscilloscope memory could only hold 2000 points per trace and a 4 μsec window was required for most of the measurements. Once the trace was sufficiently averaged a computer with a GPIB interface to the oscilloscope could download the curve to a file on the hard disk. The data acquisition starts when the trigger channel rises above a preset voltage. The trigger is an electrical pulse generated by the laser power supply to alert the instrumentation that the laser has fired. The trigger reaches the oscilloscope through a coaxial cable plugged into one of the oscilloscopes auxiliary channels. The arrival time of light on the sample is delayed as compared to the trigger arrival by amount of time determined by the difference in signal and trigger cable lengths, laser optical path and a built-in trigger delay in the laser control module. Typical total delays were between 90 and 120 nsec.

To extract accurate information from the raw data, some substantial post-processing was required. Firstly, a noise background was subtracted from the trace to eliminate noise structures which did not change significantly during the acquisition time (10 to 20 seconds) and therefore were not averaged out. Often many different backgrounds were used for different traces due to the changes in the noise signature over several minutes. A background is acquired under the same experimental conditions except that the laser beam is blocked from reaching the sample. The traces were then time shifted to the correct time zero found with the optical trigger (the fiducial from parasitic light mentioned in Sec. 2.3.5). Then a Savitzky-Golay smoothing filter was applied to further reduce noise and increase the precision of the following analysis. The width of the filter was determined by the width of the peak being smoothed and the signal to noise ratio; the larger the filter, the more noise will be eliminated. However too large a filter will distort the true underlying signal by widening the peak and reducing the amplitude. The analysis is then performed the peak amplitude, peak arrival time, peak width (FWHM), peak half width on the leading edge (HWHM), the total integrated signal and other characteristics are calculated. The results are output in an ASCII format, readable by spreadsheet and graphing programs. The program TEK (originally written in QuickBasic for DOS then ported and extended in Visual Basic for Windows by the author) which controls the stepper motors, calibrates the attenuator, reads the temperature sensors, transfers data through the GPIB interface from the oscilloscope, controls an optical shutter, controls a spectrometer, takes spectra from a lock-in amplifier or oscilloscope, displays and manipulates data in multiple windows and performs the data analysis mentioned above, all with a graphical user interface, is about 21000 lines long (~ 400 pages) and will not be presented here.

2.4.3 Single Pulse Excitation

Most of the different types of experiments presented in this work were based on the simple setup presented in this section. In this basic experiment single optical laser pulses at 10 Hz were used to create an exciton gas in the Cu_2O sample. The photovoltaic signal resulting from excitons dissociated at the opposite sample face from where they are created are measured as a function of time and averaged over many pulses as mentioned earlier. Since the distance traveled by the excitons is fixed (the sample thickness) the

arrival time of the signal reveals the average exciton velocity. This type of experiment was usually performed as a function of both laser intensity (affecting the initial exciton density) and sample temperature; by varying the incident laser wavelength (from green to yellow) the initial exciton dynamics could also be changed. The sample thickness was another variable parameter albeit not very controllable.

Figure 18 shows a schematic of the experimental setup for single pulse excitation, the laser light (dotted line) is directed onto the sample in the cryostat by high reflectivity (>99.9%) multilayer dielectric mirrors; this type of mirror must be used due to the extremely high beam intensities (10^7 W/cm^2). The beam is attenuated by neutral density filter (Sec. 2.1.1) and an attenuator (Sec. 2.1.2); different laser wavelengths are obtained by either using the pulsed Nd:YAG laser (λ =532 nm) or the dye laser pumped by the Nd:YAG laser (λ = 570 to 595 nm). The filters should be positioned as close to the sample as possible to reduce beam displacement. The illuminated geometry is the simple picture depicted in Fig. 10; a delineated surface opposite the electrode face is illuminated by the laser beam. Some experiments required apertures smaller or of different shape than the fixed 2 mm diameter hole in the sample holder, therefore pinholes, wires and slits were mounted in the path of the beam outside of the cryostat as close as possible to the cryostat window on an adjustable *z-y* table not shown in Fig. 18 (*x* would be the laser propagation direction). The resulting illuminated geometry for such obstacles will be shown with the accompanying experimental results in chapter 3.

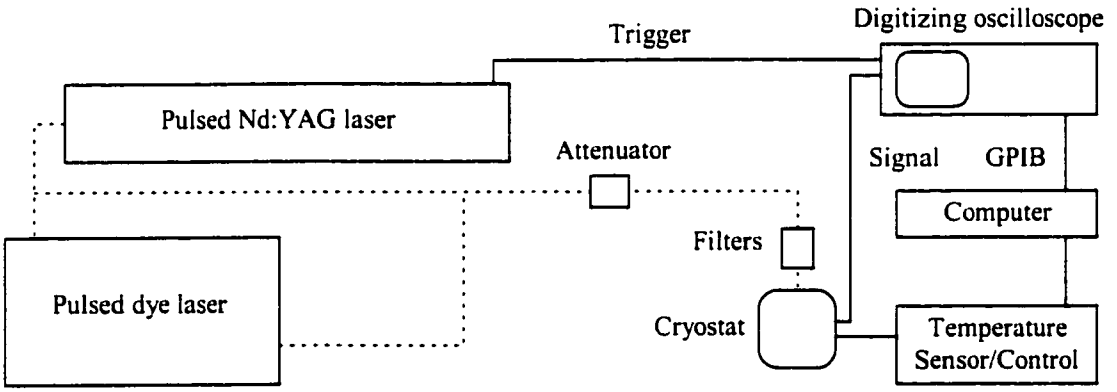

Fig. 18 Experimental setup for time resolved high intensity single beam pulsed laser measurements. Either the Nd:YAG laser (λ = 532 nm) or the dye laser pumped by the Nd:YAG laser (λ = 570 nm to 595 nm) is used alone to illuminate the sample.

The solid lines in Fig. 18 denote electrical cables between instruments: the trigger and signal cables are coaxial, the signal cable being triply shielded. This unusual amount of shielding is required due to high frequency (GHz to MHz range) electrical ringing emitted by the Pockels cell, a high voltage power supply for the laser flashlamp. The ringing is present in all conductors in the room and can completely overwhelm the photovoltaic signal as shown in Fig. 19. Shielding the laser itself or the trigger cable did not yield any substantial improvement, in fact in subsequent models, the manufacturer of the laser (Lumonics) completely redesigned the laser casing and power supply to reduce the noise. In our case the solution was a piece of crumpled aluminum foil wrapped around the top of the cryostat covering the sample rod protruding from the cryostat cover, the signal cable connector and the temperature sensor connector. Some noise still leaked in through the top temperature sensor cable, an unshielded multistrand cable which could not be shielded without affecting the temperature measurement. Therefore for fixed temperature measurements the top temperature sensor was disconnected, monitoring changes in the lower sensor was sufficient once equilibrium was established.

The amount of noise reduction seemed to depend on the contact between the sample rod, the external terminal of the coaxial signal cable and the metal clamp holding

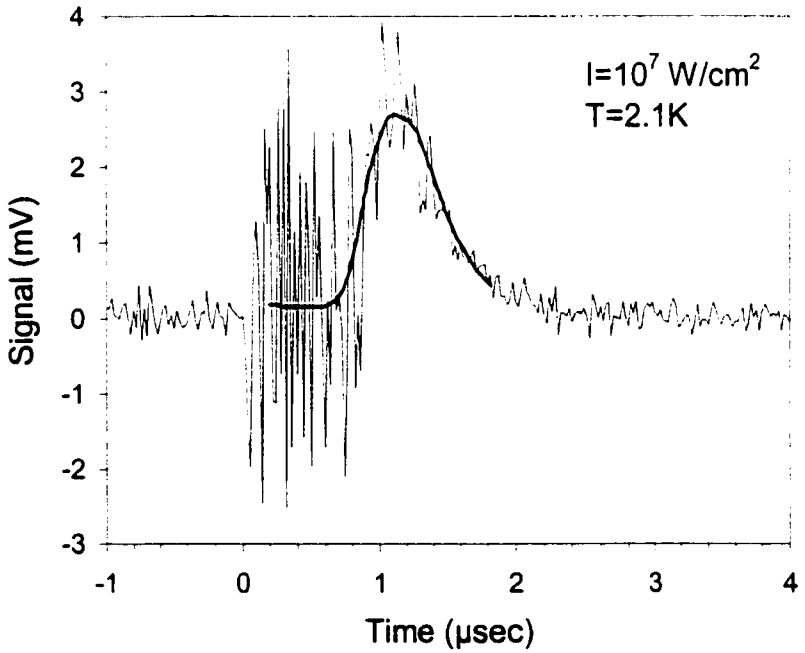

Fig. 19 Preliminary measurement using sample 1 with a of thickness 3.56 mm. The thick line drawn through the noise is the underlying signal.

the cryostat cover to the cryostat body. Simply grounding all the components or putting them in a Faraday cage did not work, but the crumpled aluminum foil seemed to destroy the "coherence" of the noise (i.e. ringing). The foil was manipulated until the noise was reduced. During the experiment frost would form on the cryostat degrading the foil contact and progressively increasing the noise. This was especially a problem if some frost had formed before the foil was put on. Eliminating the frost with a hair dryer generally helped.

2.4.4 Double Pulse Excitation

2.4.4.1 Sequential Collinear Excitation

The purpose of this double pulse experiment was to observe the interaction between two packets of excitons simultaneously moving through the crystal. The single pulse from the Nd:YAG laser is split into two beams using a 50%/50% beamsplitter as shown in Fig. 20. One beam continues on to the sample as in the single pulse excitation experiment, the other beam is reflected back and forth several times before reaching the sample. The longer optical path of the second pulse introduces a controllable time delay δt between the two pulses. This delay corresponds to an initial distance $v\delta t$ in the propagation direction where v is the velocity of the first packet, between the packets in the crystal. Using this experimental setup enables us to study the longitudinal interference between the two packets as a function of distance between the packets; results will be shown in Sec. 3.2.

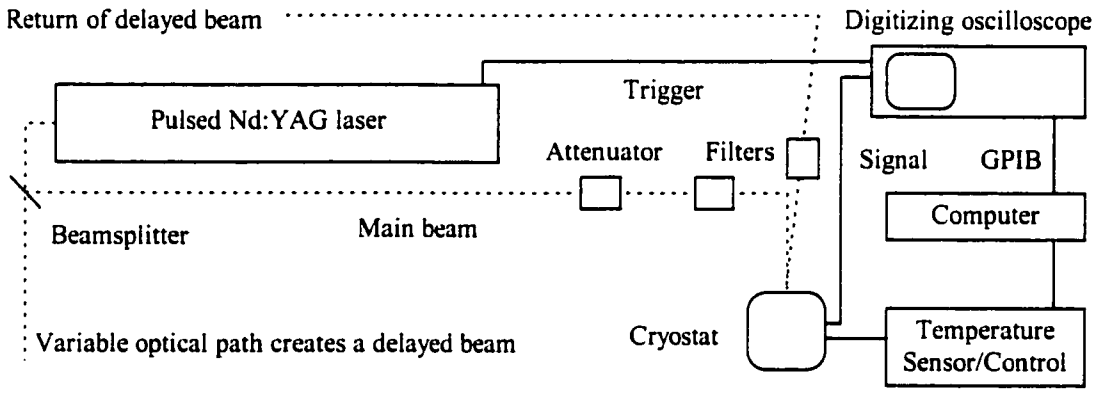

Fig. 20 Experimental setup for sequential collinear pulsed excitation. A Nd:YAG laser pulse is split into two pulses by a 50%/50% beamsplitter. The pulses arrive at the same sample surface separated by a time determined by the length of the delayed beams optical path.

The delayed beam had to strike the sample surface at a small angle, less than 3° from normal incidence, to avoid the corner mirror redirecting the main beam onto the sample; this small angle had no effect on the experiment. In the case where the beam had traveled a large distance (several hundred meters), beam divergence (~ 1 mrad) expanded the beam and reduced the intensity considerably for two reasons: the beam cross section is increased and the 25 mm diameter mirrors used to steer the beam only reflected the central portion of the enlarged beam. A lens positioned a few meters from the cryostat was used to refocus the beam to approximately its original size when the maximum intensity was too low.

The intensity of each beam was controlled independently by two banks of filters and the attenuator, the delayed beam having a variable unknown attenuation component for the reasons mentioned above. The intensities were equalized by adjusting the output photovoltaic signal from the delayed beam to the same magnitude as the main beam output signal. The intensity of the main beam was always precisely known.

2.4.4.2 Orthogonal Excitation

A variation of the previously described double beam experiment, the goal of this procedure is to probe the interaction between a single exciton packet with a fixed (in number) population of "cold" excitons in the path of the packet. The exciton packet is created in the usual manner but a portion of the Nd:YAG beam is directed into the dye laser using the beamsplitter to produce output in the red portion of the spectrum. The red laser light is steered into the cryostat in a direction perpendicular to the green beam as

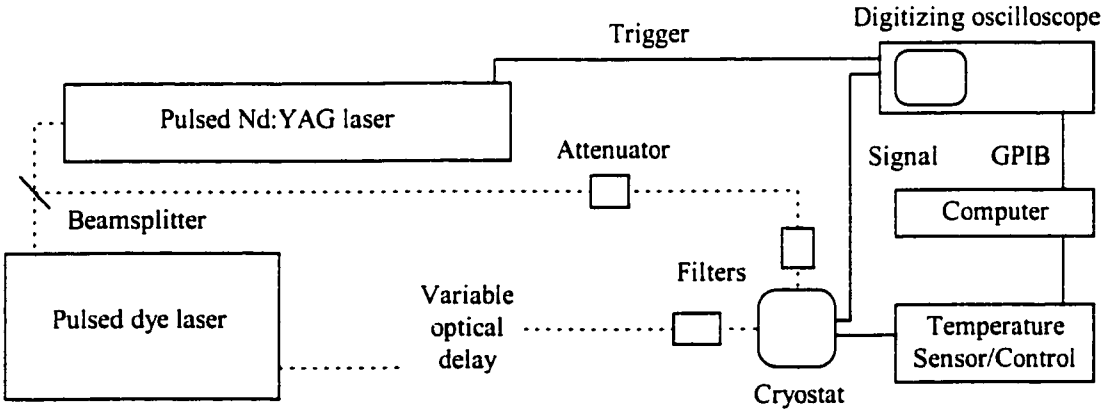

Fig. 21 Experimental setup for orthogonal double beam excitation. The Nd:YAG laser and the dye laser with output in the red are used simultaneously to illuminate orthogonal sample faces. The dye laser beam can be delayed with respect to the Nd:YAG beam by lengthening its optical path.

shown in Fig. 21. The red beam is positioned to illuminate the side aperture and the dye laser wavelength is set to a weakly absorbed region so that excitons are created deep in the crystal volume while no light directly hits the electrode. However, weakly absorbed wavelengths are easily scattered in the crystal due to impurities and lattice defects, the scattered red light gives rise to a second fiducial which is sometimes very strong.

The excitons created by the red laser are said to be cold because they are created by photons with only a small amount of excess energy as compared to the paraexciton energy. As mentioned earlier paraexcitons can not be directly created but the orthoexciton direct transition is weakly allowed in a very narrow spectral band called the quadrupole line (the transition is allowed in the quadrupole approximation). Orthoexcitons can also be created indirectly along with a single optical phonon Γ_{12}^- and an acoustic phonon in a continuum of wavelengths as seen in Sec. 1.3. These cold orthoexcitons quickly ($\tau \sim 3$ to 30 nsec) down convert to the lower lying paraexciton ground state.

This experimental setup allowed us to introduce a controllable time delay δt between the green and red pulses, so the cold excitons could be deposited in front of, in, or behind the exciton packet. Results from experiments as a function of both laser intensities and the orthogonal pulse delay time will be shown in Sec. 3.3.

2.4.5 Pulse and CW Excitation

The simultaneous pulsed and CW laser experiments were performed to explore an entirely new regime of condensate dynamics. The condensate is formed in the usual manner by a single laser pulse, however the crystal is continuously illuminated by a CW laser, producing a background of excitons filling the entire crystal volume. The non-condensed background excitons permeating the crystal can interact with the condensate producing many spectacular results as will be seen in Sec. 3.4. The two basic arrangements for the lasers beams: collinear and orthogonal, will be explained below.

The collinear pulse and CW laser beam arrangement shown in Fig. 22 is very similar to the setup described in Sec. 2.4.3 except that a tunable CW laser is added to illuminate the front sample face. The most common CW wavelengths used were at about 605.5 nm, associated with the phonon assisted absorption edge in Cu_2O, and the orthoexciton quadrupole line near 609.7 nm. These wavelength are relatively weakly

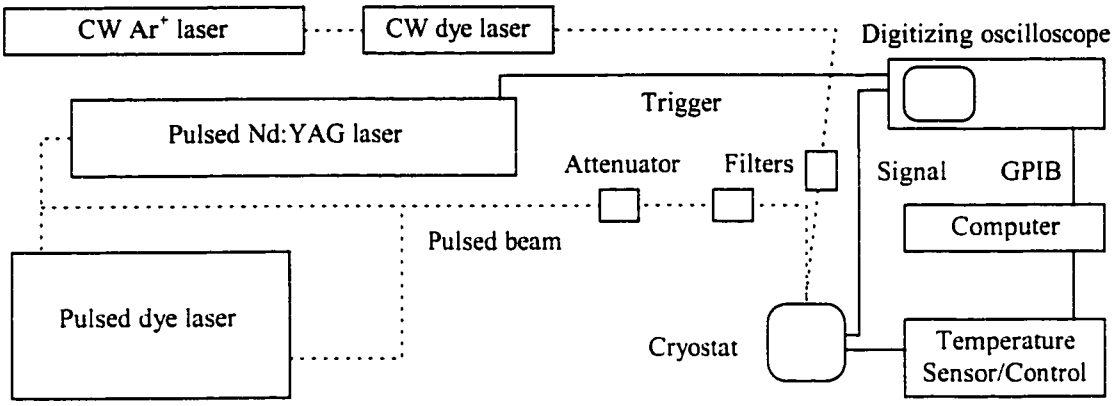

Fig. 22 Experimental setup for collinear pulse and CW beam excitation. The pulse beam is either the Nd:YAG laser or the pulsed dye laser with output in the yellow. A CW dye laser constantly illuminates the same sample face as the pulsed beam.

absorbed distributing the excitons throughout the crystal, so that the exciton condensate created by the pulsed laser travels the entire distance through the crystal in a background of these particles. In theory (Sec. 1.7) the condensate can accumulate some of the background particles and show a gain as compared to the packet traveling alone. The results from these experiments will be shown in Sec. 3.4. Some measurements were also performed as a function of CW wavelength so that the distribution of the background excitons and exciton/phonon ratio could varied.

The pulsed laser could be either the Nd:YAG or the pulsed dye laser pumped by the Nd:YAG. For most of the experimental results gathered in this geometry the CW laser was not exactly normal to the surface as can be seen in Fig. 22, but the angle was kept to a minimum (< 4°). When this angle was varied some of the results changed somewhat, however this was not explored any further and the angle was always about the same (± 1°) for all the different experimental runs.

Due to the fairly large divergence of the CW dye beam a lens was always used to reduce the beam size and consequently increase the intensity of the beam on the sample surface. The beam waist was always larger than the 2 mm sample aperture to keep the surface fairly evenly illuminated, the intensity drop off near the edge of the aperture was similar to the case of the pulsed laser beam.

A modification of the position of the CW laser beam from the previous case leads to the orthogonal excitation arrangement shown in Fig. 23 which is similar to the setup in Sec. 2.4.4.2. The CW laser beam impinges on the sample through the 1 mm diameter side

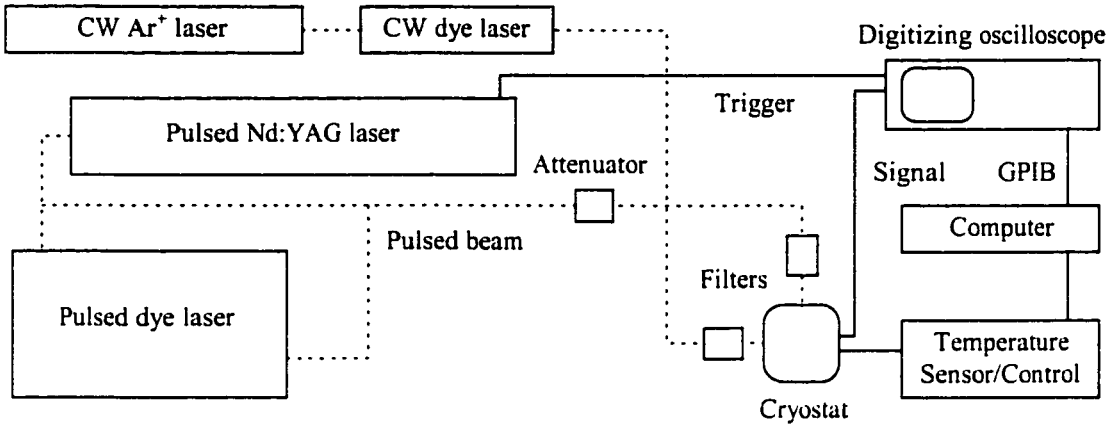

Fig. 23 Experimental setup for orthogonal pulsed and CW beam excitation. The pulse beam is either the Nd:YAG laser or the pulsed dye laser with output in the yellow. A CW dye laser constantly illuminates the side face of the sample.

aperture. Again a lens was used to increase the power reaching the sample through the aperture. This arrangement accomplishes the same goal as the previous setup, distributing cold excitons in the volume of the crystal, but at the same time greatly reducing the amount of CW light directly hitting the electrodes.

3 Results and Analysis

This Chapter will present the results obtained from numerous experiments performed over many years. The goal of the experiments was to gain a better understanding of Bose-Einstein condensation of excitons and its related effects in Cu_2O. The results of each experiment are accompanied by a discussion or analysis which attempts to incorporate the findings within the overall picture of BEC.

3.1 Single Pulse Excitation

3.1.1 Exciton Diffusion

Before discussing the ballistic transport of excitons across the sample, data corresponding to the more mundane case of exciton diffusion will be described in this section. The diffusion process was briefly described in Secs. 1.2 and 1.5; an overview as applied to our experimental and measurement system is described here.

We consider the case of excitons with little interaction in a crystal lattice (i.e. Brownian particles). The thermal motion of the particles invokes a mean squared displacement of a particle in 1D equal to

$$< x^2 >= 2Dt \tag{34}$$

where t is the elapsed time and D is the diffusion coefficient which varies as a function of temperature and essentially describes the damping or viscosity of the system. A very large diffusion coefficient means there are few collisions and the system easily expands due to its own thermal motion. Eq. (25) in Chapter 1 describes this type of system as a differential equation, for which the solution is Eq. (24), a Gaussian expanding in space as a function of time. For a system of excitons in Cu_2O at low temperature (T = 2K) the solution (with zero drift velocity) is plotted in Fig. 24 as a function of position and time. As can be seen in the figure the particle distribution initially localized near x = 0 spreads out in a matter of microseconds to a nearly homogeneous exciton gas due to the large diffusion coefficient. The value of the diffusion constant used in the calculation was obtained from fitting experimental data to be shown below and is consistent with values found in the literature [5, 11]. The exciton lifetime used in this calculation is large (τ = 50 μsec) as compared to the diffusion times involved and consequently has little effect on the results.

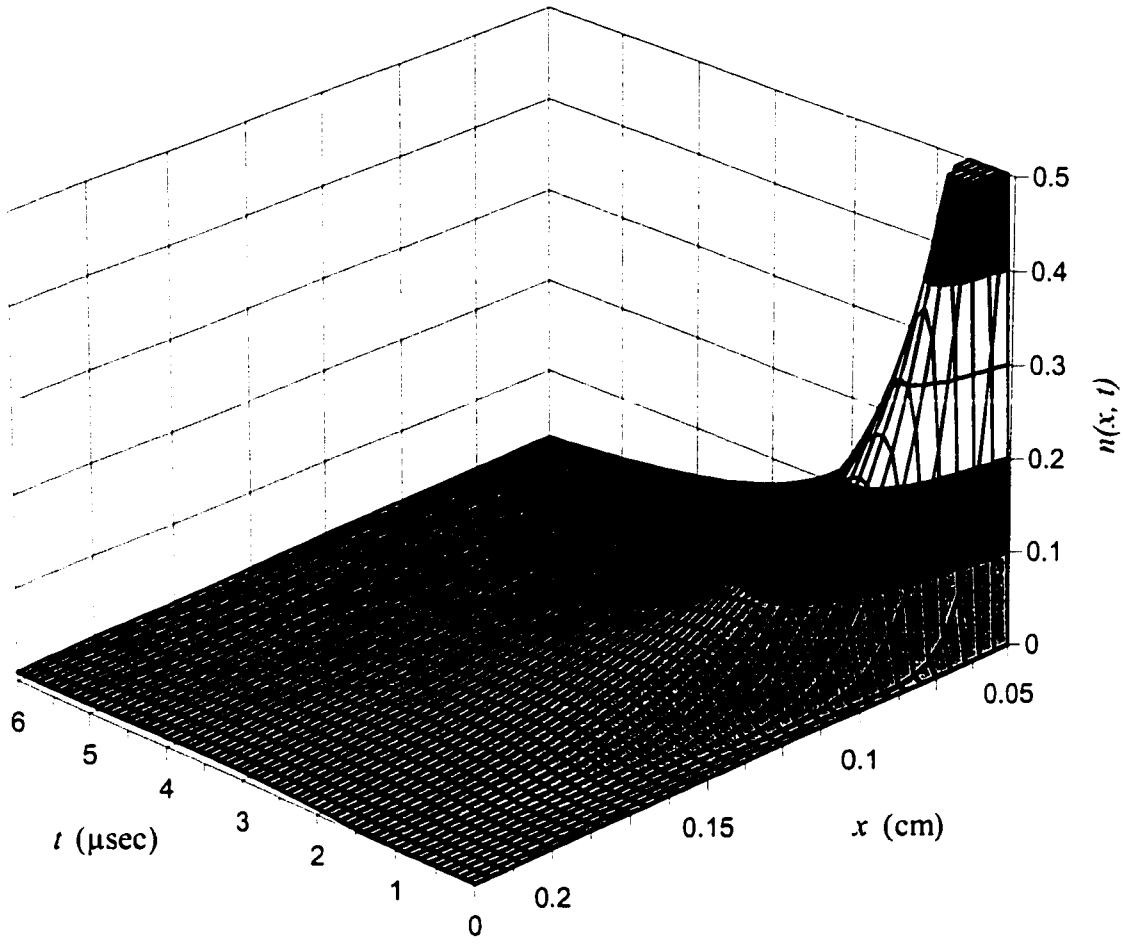

Fig. 24 Solution of 1D diffusion equation given by Eq. (25) as a function of position and time with parameters D = 2000 cm^2/s, v = 0 and τ = 50 μsec. The maximum of the distribution is arbitrarily set to 1 but the z-axis has been cutoff at 0.5 to clearly show the late time behaviour.

This theoretical model was verified by the single pulse excitation experiment described in Sec. 2.4.3. A dye laser pulse (λ = 585 nm) deposits a fixed number of excitons in a relatively short time (~ 8 nsec) within a narrow region (~ 100 μm) near the sample surface. The excitons diffuse into the crystal and those reaching the opposite surface a few millimeters away are measured by the detector as a function of time. The experiment, like the theoretical model is nearly one dimensional since the area over which the particles are deposited and the detector area are the same size, about 30% of the crystal face. Although as we shall see this does not preclude some diffusion occurring in the directions perpendicular to propagation.

The amplitude of the electric signal S (in mV) produced by the detector as a function of time is proportional to the exciton flux at the detector, hence

$$S(t) = \eta n(t) v A \tag{35}$$

where η is the detector efficiency, n is the local exciton density, v is the local exciton average velocity and A is the local cross sectional area of the cloud or the detector area, whichever is smaller. Note that the efficiency is only known to within a few orders of magnitude therefore making the absolute calibration of the density difficult. The average velocity is the drift velocity of the cloud. However Eq. (35) can only be easily applied in the ballistic regime where all the excitons are moving at about the same velocity: this case will be examined in the next section. The transport of particles (which implies some kind of non-zero local average velocity) by a diffusion process is a consequence of the time evolution of Eq. (25) and hence does not require an explicit velocity i.e. diffusion with zero drift velocity still leads to a non-zero signal. Therefore in the diffusive regime the amplitude of the electric signal is directly related to the local exciton density: $S(t) \propto n(t)$ and the time resolved data can be directly fitted by Eq. (24).

The smoothed time resolved data for four laser intensities is shown in Fig. 25 along with a fit of each individual trace using Eqs. (24) and (35) for a fixed distance x = 1.97 mm: the crystal thickness. The traces in Fig. 25 were substantially smoothed (400 point wide filter for a 2000 point trace) to help in the fitting process and for clarity in the figure; even so some noise still remains especially at lower frequencies near the primary signal component frequencies. The diffusion coefficient (D = 2000 cm^2/s) and exciton lifetime (τ = 50 μsec) are the same for the four fits, the drift velocity (v = 1.2x10^5 cm/s) varies only slightly (~ 15%) and the amplitude S_o ($\propto n_o$) is scaled to the laser intensity by $S_o = 0.036I$ where S_o and I have units of mV and W/cm^2 respectively. The value of the lifetime, as long as it is greater than about 10 μsec, has little effect on the quality of the fits, therefore this type of experiment can not determine the exciton lifetime. The linear relation between the laser intensity and signal amplitude while the drift velocity is constant indicates that the resulting exciton density in the cloud scales linearly with input density as expected from the diffusion model. The data was also fitted by a 3D model (Eq. (25) is the same except the exponent in the denominator of the prefactor is 1.5 and not 0.5); the results were nearly identical to those shown in Fig. 25 except the scaling factor (0.036 above) was larger.

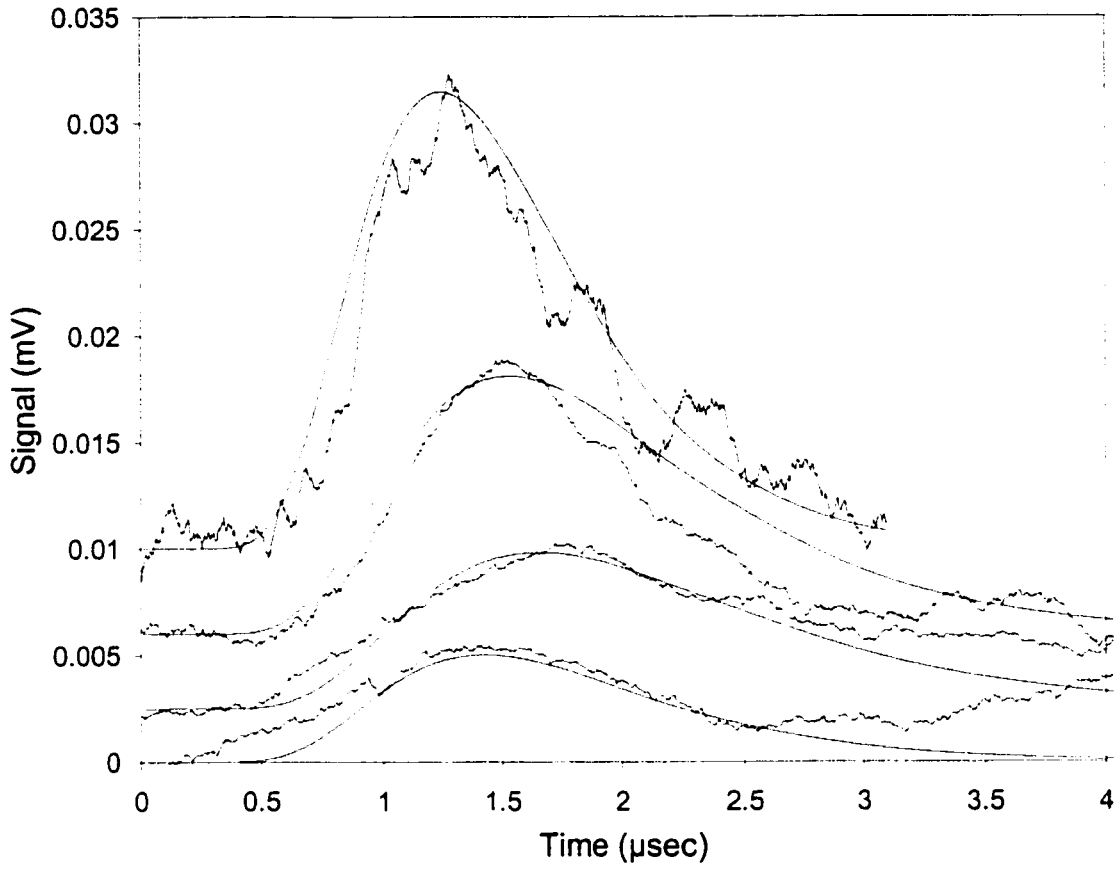

Fig. 25 Excitonic flux from single pulse illumination (λ = 585 nm) for a 1.97 mm thick Cu_2O crystal at T = 2K. The results for four laser intensities are shown vertically displaced for clarity, each with a fitted curve. From the bottom the intensities are: $0.027I_o$, $0.043I_o$, $0.069I_o$ and $0.11I_o$ where $I_o = 10^5$ W/cm^2. The fitted curve using Eq. (24) is the smooth trace in each case, the fitting parameters are given in the text.

The drift velocity is assumed to be constant during the transport in this theoretical model, however this is unlikely in the real system. The drift is likely to be fastest right after the laser pulse due to the exponential absorption profile which creates a large density gradient towards the interior, and due to the peak in the non-equilibrium LA phonon population during exciton creation and cooling which could impart momentum to the excitons. Then the excitons likely slow down as the particle distribution becomes more homogeneous and the phonon population equilibrates. However we can not determine the instantaneous velocity from our transport measurements, only the average velocity.

A Nd:YAG laser pulse (λ = 532 nm) which deposits the excitons in an even narrower region near the sample surface (~ 3 μm) produces very similar results except the signal amplitude is smaller and the noise more important since the signals are very

near the background noise threshold. The smaller amplitude is presumably due to a greater expansion of the cloud perpendicular to the propagation direction.

3.1.2 Ballistic Transport

We now study the opposite of diffusive transport, ballistic transport (i.e. prolonged propagation at or near the speed of sound without scattering where $\tau_s \rightarrow \infty$), by repeating the same experiment described in the preceding section with an increased laser intensity. A high and low intensity trace (labeled a) and c) respectively) produced by illumination from a dye laser (λ = 585 nm) can be directly compared in Fig. 26; the shape and amplitude of the exciton distribution arriving at the detector changes drastically from one case to the other. The much more compact exciton cloud created by the high intensity laser pulse travels faster across the sample, has a higher peak density (even considering the factor of 3 in velocity), and contains many more excitons than the cloud created by

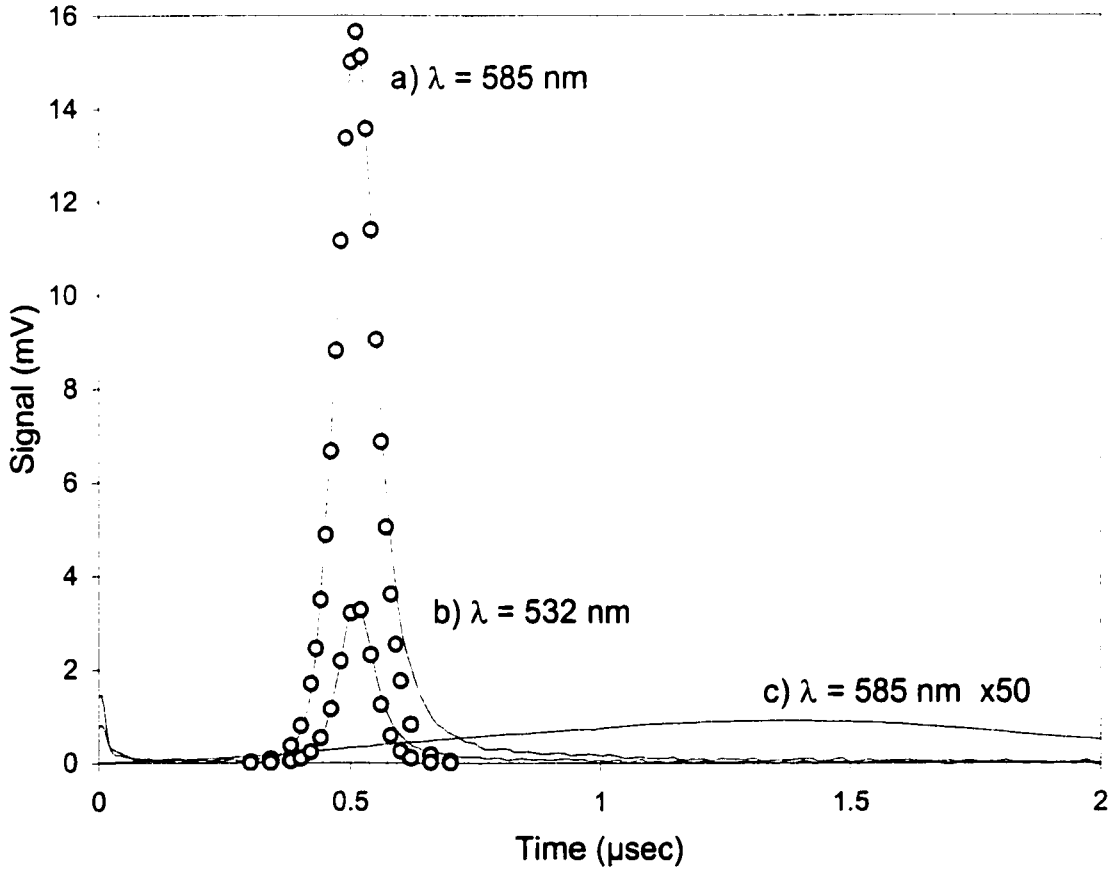

Fig. 26 Excitonic flux from single pulse illumination for a 1.97 mm thick Cu_2O crystal at T = 2K. From the top the intensities are: $10I_o$, $10I_o$ and $0.2I_o$. The bottom trace c) was amplified by a factor of 50 for clarity. The laser wavelength for each trace is noted on the figure. The open circles are best fits to the signal using Eq. (23).

the low intensity laser pulse as witnessed by the larger time integrated signal.

The excitons in the compact cloud are said to be ballistic since they are traveling over a large distance at nearly the speed of sound. The following calculation demonstrates this fact: using the arrival time of the maximum of the distribution t_{max} and the crystal thickness x, we calculate the average packet velocity: $v = x / t_{max}$ = 1.97 mm / 0.51 μsec = 3.9×10^5 cm/s, about 87% the speed of sound. The packet size d is calculated by multiplying the temporal width Δt of the distribution by the average velocity: $d = v\Delta t$ = 3.9×10^5 cm/s x 0.09 μsec = 350 μm. Trace b) obtained by Nd:YAG illumination is shown for comparison to trace a). The packet size and velocity are nearly equal for the same laser intensity ($I = 10I_0$) for both laser wavelengths, even though the initial density of excitons due to absorption is greatly different as was shown in Sec. 1.4. It appears that in the ballistic regime the transport velocity and final packet size does not depend so much on the initial distribution of the excitons. We can not completely explain the large difference in the signal amplitude between traces a) and b) although it may be due to a factor of 2 difference in the lateral size of the packet giving a factor of 4 signal change, or it may be due to greater losses occurring during transport in the λ = 532 nm excitation case.

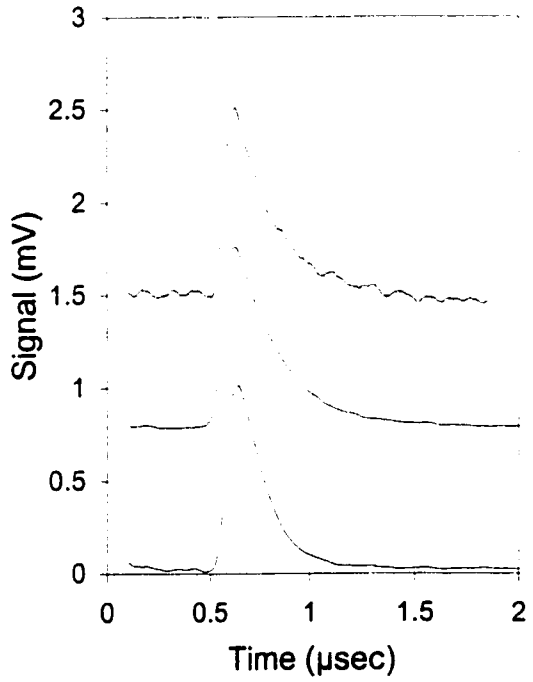

Fig. 27 Ballistic packet propagation for three distances (from bottom: 2.5 mm, 3.56 mm (both sample 1) and 8.3 mm (sample 3)) under the same conditions ($I \sim 60I_0$, T = 2K and interlocking finger electrodes). The top two traces have been time shifted (0.21 and 1.215 μsec) and vertically scaled (2.6 and 14) to the same position and amplitude as the bottom trace.

The ballistic propagation continues for even greater distances than in Fig. 26; three traces produced by intense Nd:YAG illumination of thicker crystals are shown in Fig. 27. We note that in this figure the size of the cloud remains nearly constant ($v\Delta t$ ~ several hundred μm) after propagating over more than 8 mm. This behaviour is completely different than the diffusive motion present at low laser intensity where the cloud is always growing in size. At some point early in its

travel the ballistic cloud has stopped diffusing since a gradual growth would be apparent in the travel between 2.5 mm and 8.3 mm, and the cloud is much larger than the initial exciton distribution. We postulate that after an initial expansion and cooling stage the excitons undergo Bose-Einstein condensation and the condensate acquires the large (at early times) drift velocity of the cloud. The two main characteristics of the transport, the nearly sonic propagation over large distances and the formation of a non-diffusive packet, are simple consequences of the superfluidity of the excitons and the grouping of particles into a single momentum state.

According to the LR theory a stable condensate propagating above the critical velocity and below the sound velocity should be in the form of a soliton. The open circles in Fig. 26 represent a best fit soliton which reproduces the form of the signal quite well especially on the leading edge. The surplus of particles on the trailing edge may be due to non-condensed particles ejected from the condensate; more about this later. We note that the cloud right after condensation is not necessarily (and most probably not) a soliton. The excitons probably undergo some reorganization to gain the stable soliton shape and the final packet thickness measured at the detector may not correspond to the original condensate thickness.

An alternative interpretation of the ballistic motion has been proposed where the excitons are blown across the crystal by a non-equilibrium LA phonons created during exciton formation and cooling, this is the "phonon wind" model [34]. The model does predict the observed propagation of excitons at near sonic velocities, but it offers no mechanism that suddenly halts the diffusion of excitons *part* way into the transit as must be the case for the observed ballistic signals in Figs. 26 and 27. This is but one of the faults of the model and many other inconsistencies are revealed by nearly every other experiment discussed in this work. We believe that the phonon wind model is incorrect as applied to our results and that the ballistic transport of excitons in Cu_2O is due to Bose-Einstein condensation [35, 36, 37]. However as mentioned above the motive force responsible for the drift of the diffusive cloud could be non-equilibrium phonons.

3.1.3 Transition from Diffusive to Ballistic Transport

After discussing the two extremes of transport we now examine at the more difficult case of transport with both components and the critical laser intensities and related exciton densities at which the changeover occurs. The full range of transport for dye laser illumination (λ = 585 nm) for a Cu_2O crystal at T = 2K is presented in Fig. 28. The abrupt accumulation of particles into a packet is evident above $I \sim 3I_o$ (as indicated by the arrow) as the distribution narrows and the average velocity increases. Below this excitation intensity and above a lower critical intensity we postulate that the transport is neither purely ballistic nor purely diffusive but a mixture of both.

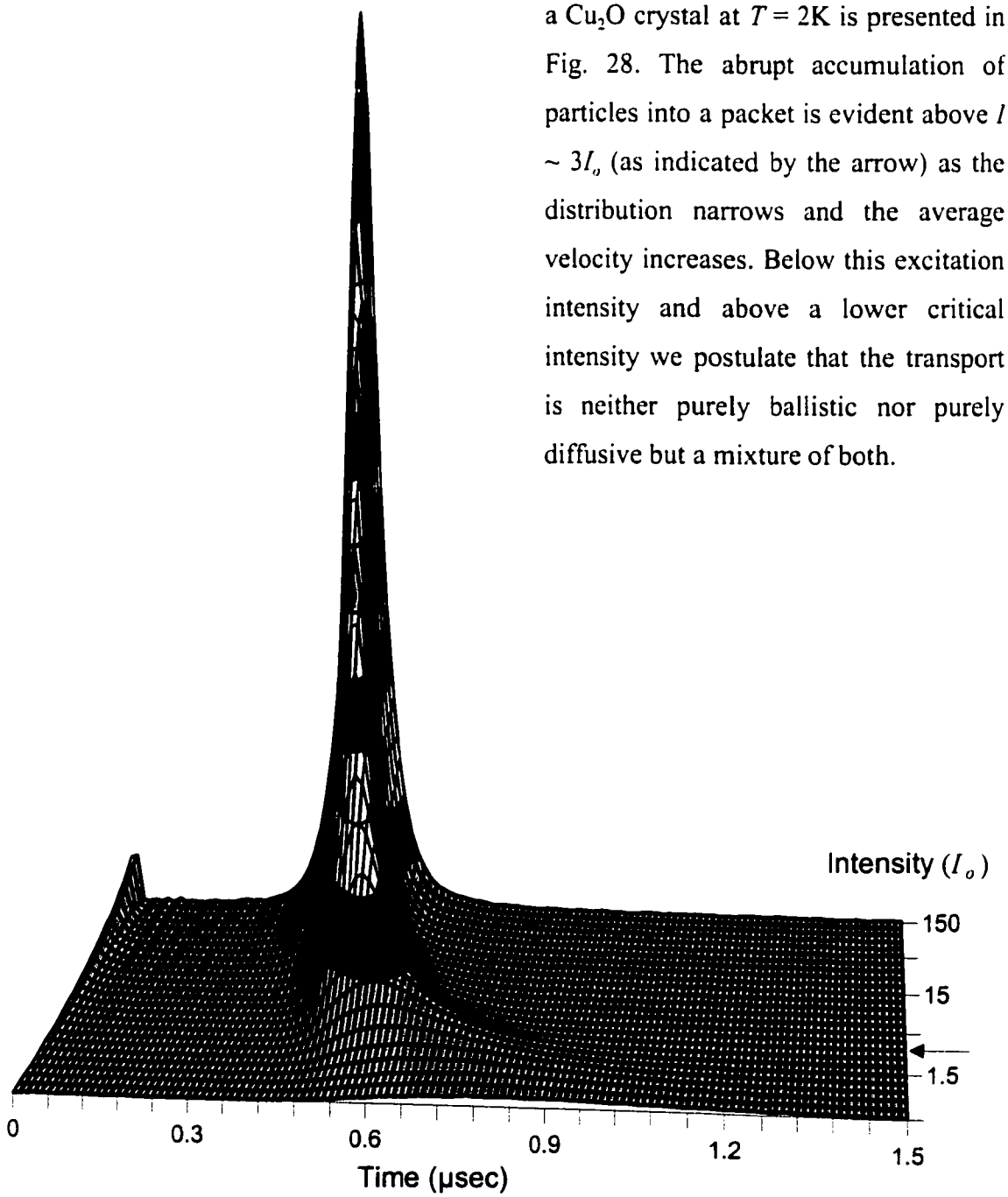

Fig. 28 Time resolved excitonic flux from single pulse illumination (λ = 585 nm) with intensities from $0.5I_o$ to $150I_o$ for a 1.97 mm thick Cu_2O crystal at T = 2K.

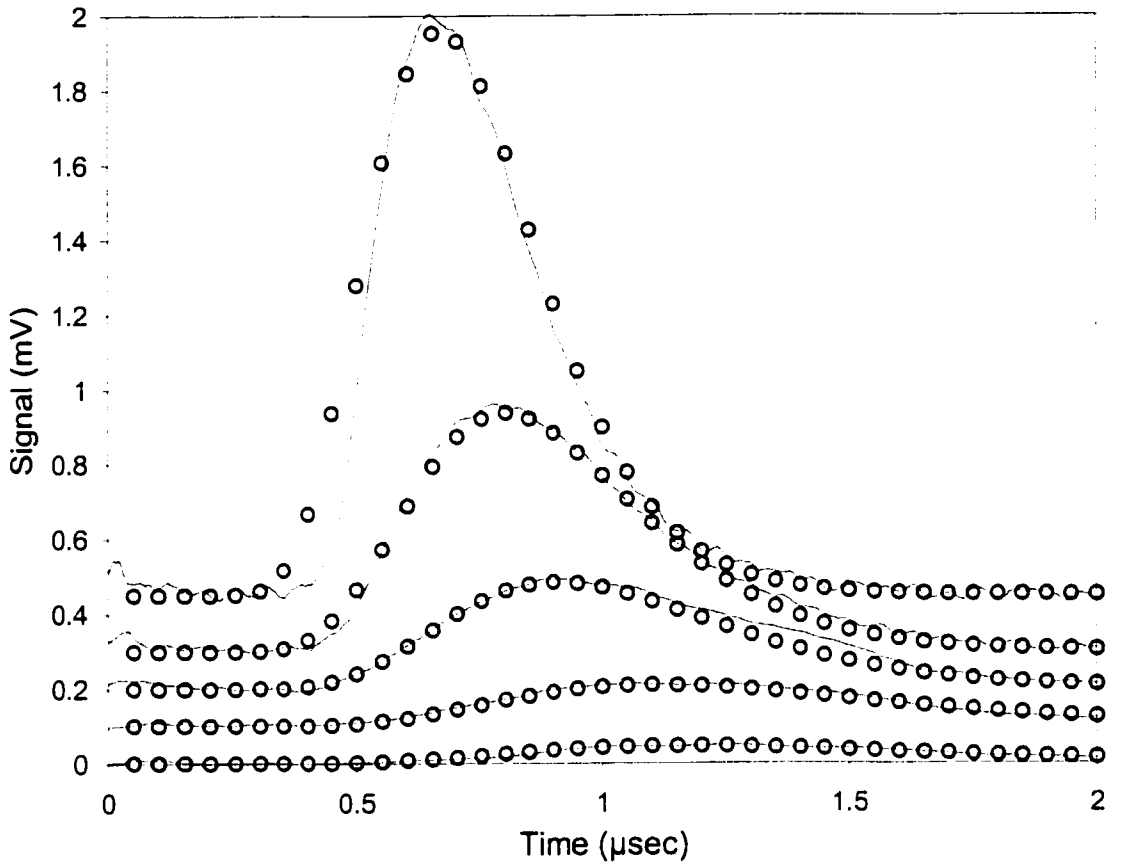

Fig. 29 Excitonic flux from single pulse illumination (λ = 585 nm) for a 1.97 mm thick Cu_2O crystal at T = 2K. The results for five laser intensities are shown vertically displaced for clarity, each with a fitted curve (open circles). From the bottom the intensities are: $0.17I_o$, $0.27I_o$, $0.43I_o$, $0.7I_o$ and $1.2I_o$ where $I_o = 10^5$ W/cm^2. The fitting parameters are given in Table 4.

To elucidate this hypothesis Fig. 29 was constructed. In this figure traces for five intensities ranging from $0.17I_o$ to $1.2I_o$ are shown along with traces fitted using Eq. (24) (open circles). The data was fitted using the same parameters as in Fig. 25 (D = 2000 cm^2/s, τ = 50 μsec), except that the drift velocity and the amplitude was increased as a function of laser intensity (see Table 4). The signal amplitude parameter S_o should increase linearly with the laser intensity if the diffusion model was fully applicable but this is not the case here; to properly fit the data the parameter S_o must be

Intensity (I_o)	v (10^5 cm/s)	q
0.17	1.6	1.3
0.27	1.7	1.9
0.43	2.1	2.8
0.7	2.4	3.7
1.2	2.9	4.7

Table 4 Fitting parameters used in Fig. 29; v is the average drift velocity and q is an amplitude scale factor applied to the linear scale used in Fig. 25 i.e. $S_o = q\ 0.036I$.

increased non linearly by multiplying it by the factor q shown in Table 4. Furthermore in order to better fit the $1.2I_o$ and $0.7I_o$ traces the diffusion coefficient would have to be reduced from 2000 cm^2/s to ~ 1000 cm^2/s in these two cases since the fitted trace is too wide, especially on the leading edge. The apparent increase in the average drift velocity and in the number of excitons reaching the detector, along with an apparent decrease in the diffusion coefficient leads us to conclude that the packet has propagated ballistically and remained a fixed size for part of its journey across the crystal. We attribute this behaviour to Bose-Einstein condensation of the excitons for a fraction of the total transit time, the fraction increasing as the laser intensity is increased. We believe the mechanism provoking this behaviour is the increasing fraction of particles in the condensate as the density surpasses the critical density. The fraction of excitons in the condensate is calculated using Eq. (14) and graphically depicted in Fig. 30. The larger the fraction and hence number of excitons in the condensate, the farther it can propagate ballistically.

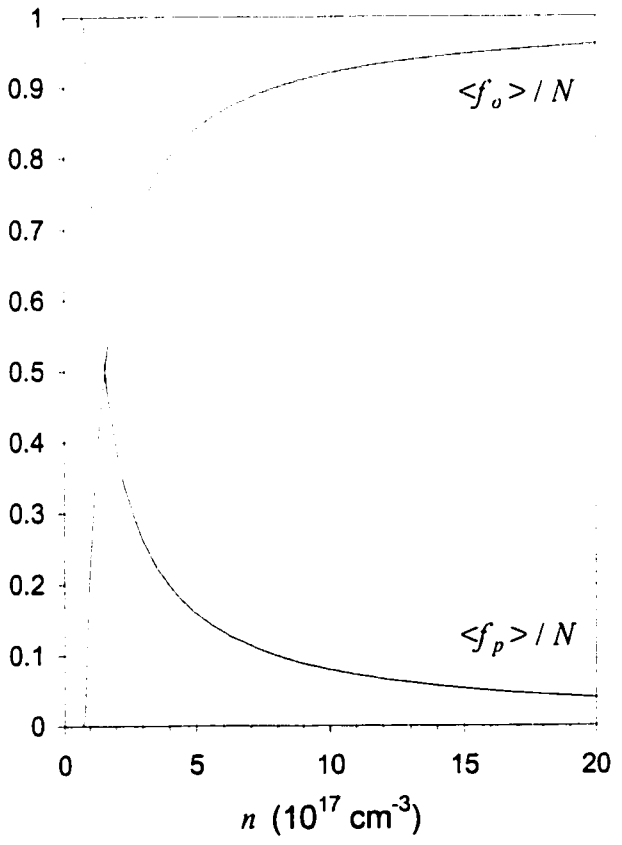

Fig. 30 Fraction of condensed ($<f_o>/N = 1 - cT^{3/2}/n$, c = 2.8×10^{16} $cm^3/K^{3/2}$) and normal ($<f_p>/N$) excitons as a function of exciton density in a Cu_2O crystal at T=2K.

Bridging this idea with the results shown in Sec. 3.1.2 leads us to the question: what is the intensity above which the transport is ballistic for the entire length of the transit? In order to find the critical intensity at which the ballistic motion appears and the intensity at which the transport is fully ballistic, two graphs were constructed as follows: The arrival time of the distribution maximum such as those seen in Fig. 28, can be converted into an average propagation velocity (normalized to the sound velocity) v/v_s using the sample thickness. The temporal width of the packet in conjunction with the velocity gives the spatial

extent of the packet d in the propagation direction. We used the temporal HWHMx2 in an attempt to filter out the effects of the trailing edge. The normalized velocity and packet size are plotted as a function of laser intensity in Fig. 31. Data for two different laser excitations (λ = 585 nm and 532 nm) and sample thickness (1.97 mm and 2.2 mm respectively) are shown.

Figure 31 clearly reveals a sudden increase in the average packet velocity and a sudden decrease in the size of the packet reaching the detector at ~ $0.3I_o$ for the λ = 585 nm data. Near this intensity there is also a significant increase in the fitting parameter q (see Table 4) which signals the departure of the transport from the diffusion model. The exciton density profile near the surface for this laser intensity and wavelength was calculated in Sec. 1.4 and the profile shown in Fig. 6. The density of excitons (~ $6\text{x}10^{16}$ cm^{-3}) is very close to the critical density for BEC of excitons reinforcing the link between the onset of partial ballistic transport and BEC. As the laser intensity is increased the

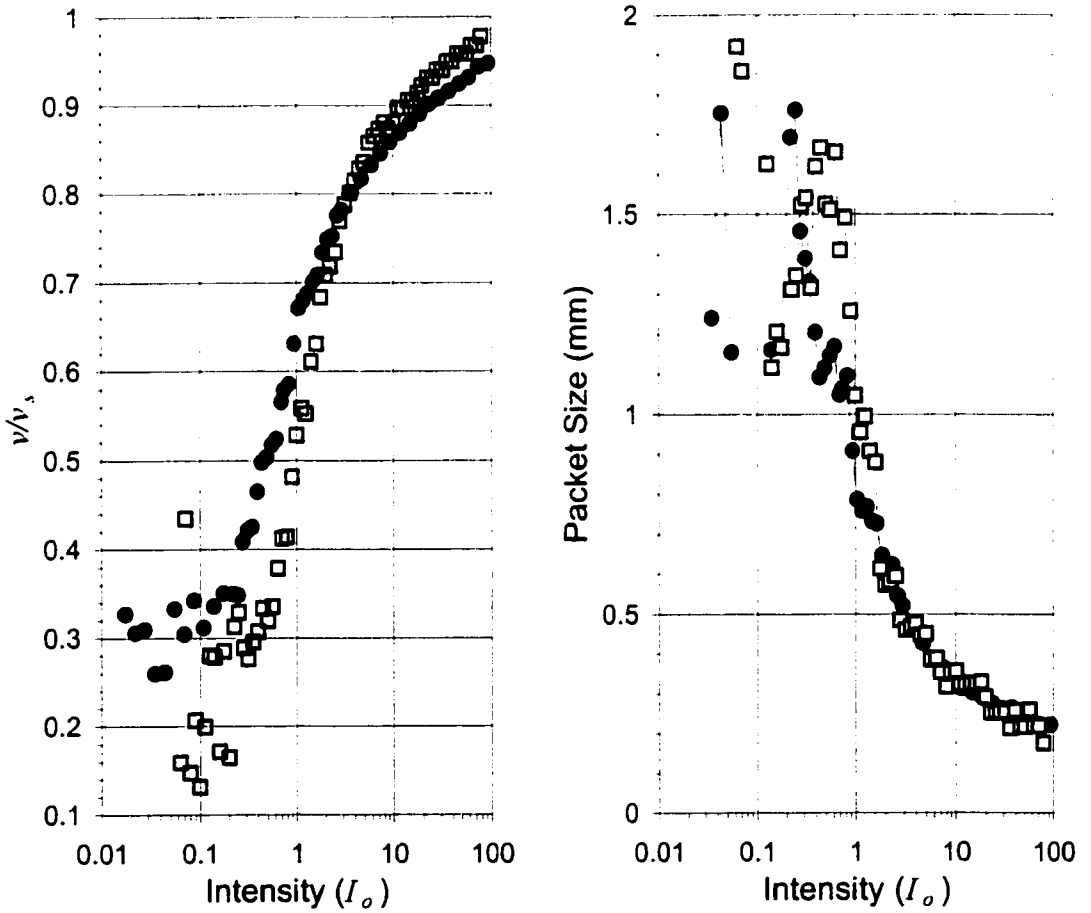

Fig. 31 Normalized average drift velocity (left pane) and size of exciton packet (right pane) at T = 2K. Filled circles: λ = 585 nm, x = 1.97 mm; open squares λ = 532 nm, x = 2.2mm.

average velocity increases and the packet size decreases; this is an agreement with the proposed model since if the fraction of ballistic transit increases the average velocity would increase as well, and the size of the packet would decrease due to a decrease in the amount of diffusion since fewer excitons are in the non-condensed fraction as seen in Fig. 30.

Such a break is not as clear in the λ = 532 nm data, especially when one looks at the raw data (not shown here): the smaller signal amplitudes and lower signal to noise ratios muddy the picture. Indeed if one expected a break in the behaviour following the above reasoning it should occur at much lower intensity (~ $0.02I_o$) well below the noise threshold. But the temperature and density at early times are much more difficult to predict for this laser wavelength; the initial distribution surely expands and cools and perhaps condenses, but for how long and when? The increase of the velocity and decrease of the packet size at higher intensities mirrors the λ = 585 nm data indicating that the overall transport is similar, the details at early times are unclear.

We now focus our attention on the transport at high intensity. As mentioned above both laser excitation wavelengths produce the same behaviour, both v/v_s tracks start to saturate, and there is a break in the reduction of the packet size at ~ $4I_o$. This break can also be seen in the parameter β plotted in Fig. 32. β is proportional to the product of the packet width and amplitude and was calculated using Eq. (23) along with the relations: $n_o \propto S_o/v$ and $\Delta = v \cdot \text{HWHM}/0.88$ where S_o is the signal amplitude, v the packet velocity and we used the temporal HWHM on the leading edge. The relevant density in this case is the density of excitons in the packet as opposed to the initial exciton profile described by Eq. (19). Assuming no expansion of the packet in the

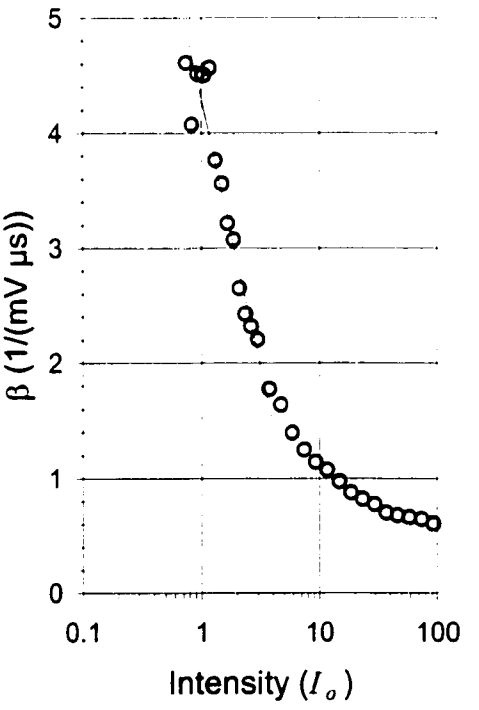

Fig. 32 Parameter β calculated from the temporal HWHM, the average velocity and the signal amplitude for the time resolved data shown in Fig. 28. The straight line helps guide the eye to the break at ~ $4I_o$.

perpendicular directions (with respect to motion) we can calculate the approximate density in the center of the packet independent of its lateral dimension:

$$n = \frac{\lambda}{hc}\frac{I\,\delta t}{d} \tag{36}$$

where λ is the laser wavelength, I is the laser intensity, δt is the laser pulse duration and d is the spatial width of the packet in the direction of propagation. The calculated density at $I \sim 4I_o$ and $d \sim 400$ μm for both wavelengths including 30% reflection losses is $\sim 1.7\text{x}10^{17}$ cm^{-3}, only a factor of two above the critical density for BEC. We propose that the break in the evolution of the properties of the packet is due to the arrival of a ballistic Bose condensed packet at the detector face. It is very important to note that the above calculation is insensitive to the lateral size of the packet, (as long as it is smaller than the detector and laser beam cross section). We can not directly measure the final lateral packet size with our "single pixel" detector and hence can not determine the final volume of the condensate. Results shown later on will indicate that the lateral size of the condensate may be smaller than the illuminated area, and other results will indicate that a very large number of the excitons are left behind, outside of the packet in the crystal volume.

In light of the preceding arguments we offer the following analogy: The condensate is like a comet, with a dense nucleus (the condensate) surrounded by a coma and followed by a tail (the normal particles). What we have called the packet above is the combination of nucleus and coma. The nucleus may be ellipsoidal due to the asymmetric exciton potential described by LR. The condensate is always trying to maintain chemical equilibrium with its surroundings and hence is always shedding particles from its core to feed the coma which is evaporating into the crystal volume and/or falling into the tail; all this is happening while the "comet" is moving ballistically away from the excitation face. At some point the condensate collapses and the "comet" slows down and diffusion (with perhaps an exponentially decreasing drift term) takes over. If the condensate happens to reach the detector face before collapse the observed transit is purely ballistic. At low laser intensities the formation of the comet may occur immediately after the laser pulse and the propagation is ballistic for a short time and then collapses and diffusion occurs. As the intensity is increased the "comet" lifetime increases but the formation time also

increases due to greater heating (see Sec. 1.4). Eventually the lifetime of the "comet" is longer than the transit time. The formation time at high intensities may explain why the width of the packet is always larger than the initial distribution width (a few hundred μm vs. 100 μm) even in the case of excitation at λ = 585 nm. It may also be that the condensate is simply adjusting its size to satisfy Eq. (23). As evidence we note the parameter β plotted in Fig. 32; while it is not quite constant above the critical intensity for ballistic transit there is only a small variation (factor of 3) in this realm as opposed to the very large rate of change below the upper critical intensity.

If the above model is correct, condensate evaporation during transit should lead to an increase in the critical intensity for ballistic transport as a function of sample thickness. This is difficult to verify since the evaporation rate could vary from sample to sample due to crystal quality (which would affect the background exciton level). Old results obtained with sample 1 when its thickness was 3.56 mm seems to indicate a break at ~ $6I_o$ [35] (as compared to $4I_o$ at 1.97 mm) which would be consistent with this interpretation.

3.1.4 Temperature Dependence of Ballistic Transport

Ideal Bose gas theory predicts that the critical density for BEC follows a $T^{3/2}$ temperature dependence. This prediction was verified experimentally by repeating the

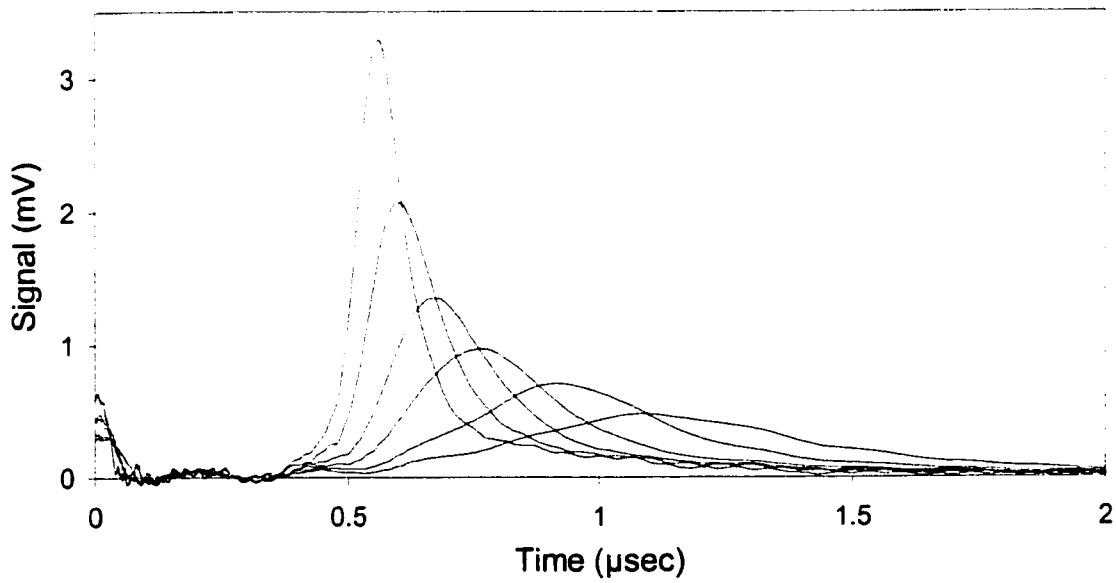

Fig. 33 Excitonic flux from single pulse illumination (λ = 532 nm) at $I = 20I_o$ for a 2.2 mm thick Cu_2O crystal. From the top the temperatures were 2.1K, 2.2K, 2.55K, 3K, 3.7K and 4K.

exciton transport experiment described in the previous section with a different sample temperature on each run. The time resolved signal for several temperatures at the same laser intensity is shown in Fig. 33. The data displayed here shows the same type of behaviour as in Fig. 28 where the temperature was fixed and the laser intensity varied. The similarity reveals the equivalence of temperature and density for a Bose-Einstein condensate.

To fully map out the phase transition from gas to condensed phase the following methodology was used: the temperature was stabilized to approximately the target temperature and traces were recorded for a series of intensities near the upper critical intensity. The temperature was stabilized at a different value and the process repeated. In the He gas above 4K the repetition rate of the Nd:YAG laser had to be lowered to 1 or 2 Hz (from 10 Hz) to avoid heating the sample because of the lower cooling rate in this temperature regime. The low cooling rate is caused by the low density of the He gas as compared to the liquid, and the low He gas evacuation rate required at these temperatures.

Some of the processed results from these experiments are shown in Fig. 34 where the packet size calculated from the HWHMx2 on the leading edge and the average velocity as described earlier is plotted as a function of laser intensity for four temperatures. The small vertical arrows denote the critical intensity at which there is a break in the packet size reduction rate. As was discussed

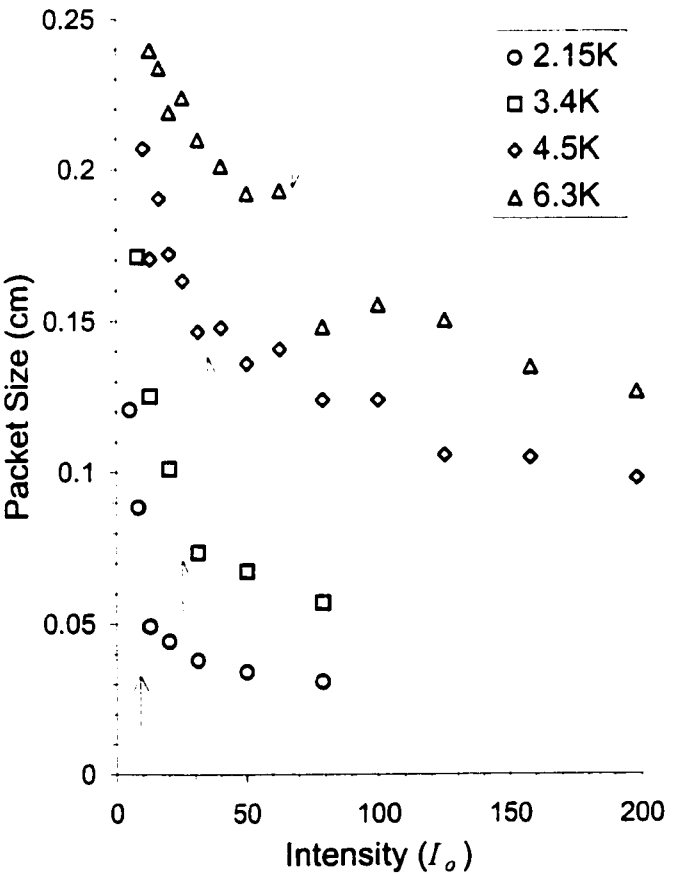

Fig. 34 Packet size as a function of Nd:YAG laser intensity in a 2.2 mm thick crystal for the temperatures indicated in the legend. Vertical arrows indicate the critical intensity for each temperature.

in the previous section this critical intensity is linked to the critical density for Bose-Einstein condensation of excitons after some initial expansion and cooling of the cloud. There is however substantial uncertainty in the interpretation of the critical intensity for a variety of reasons: firstly the raw data is inherently noisier due to the presence of the temperature sensor and at high temperature the lower repetition rate reduced the number of traces in the average. Secondly this data was collected before the fabrication of the variable attenuator and stepper motor controlled valve, so temperature and intensity fluctuations also caused some scatter in the points. Thirdly the break point is bracketed by only a few data points since the number of points collected for a particular temperature was limited by time constraints (i.e. changing the intensity with filters took more time than with the attenuator and the temperature could not be easily stabilized without the electric valve). In addition the unweighted average used by the oscilloscope included traces above and below the transition (due to pulse to pulse laser intensity fluctuations) washing out the transition. And finally the transition itself is not completely abrupt reflecting the large number of normal particles always reaching the detector and smoothing out the transition (see Fig. 36 below).

Nevertheless the critical intensity is plotted with appropriate error bars for a wide range of temperatures in Fig. 35 and the data is fitted to the curve $cT^{3/2}$ where $c = 3.5$. The critical intensity for the data obtained in liquid He was adjusted due to the apparent attenuation by bubbles (see Sec. 2.4.1). The error bars do leave some latitude in the value of the fitting

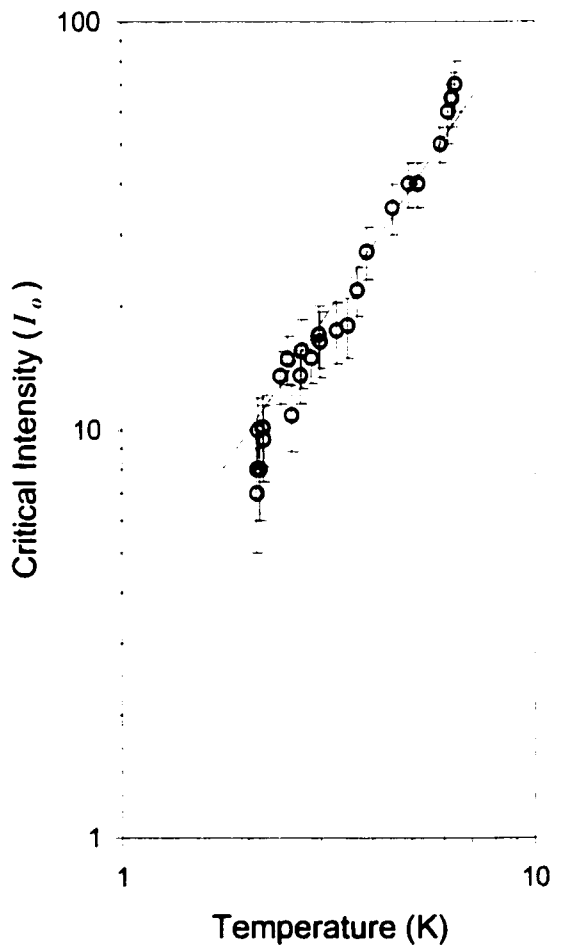

Fig. 35 Critical intensity as a function of temperature for a 2.2 mm thick crystal illuminated by a Nd:YAG laser.

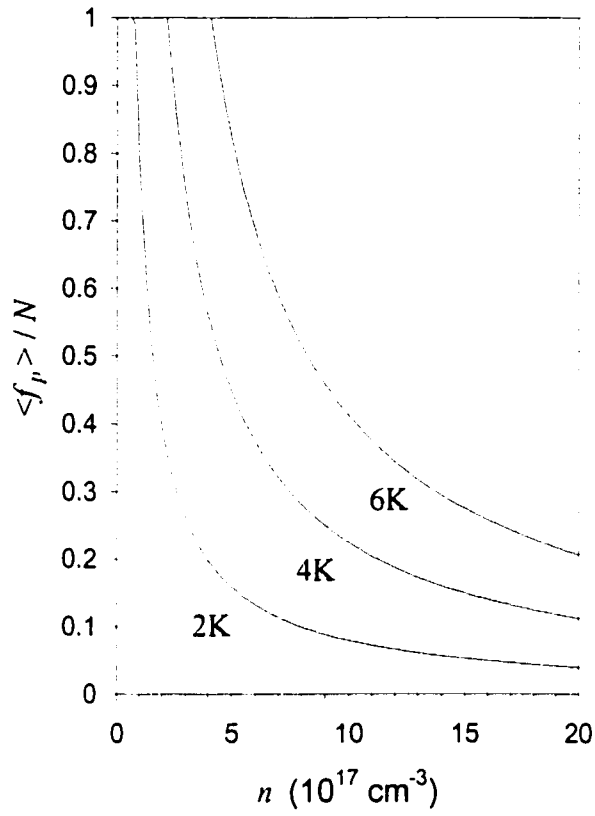

Fig. 36 Fraction of non-condensed excitons in Cu_2O as a function of density for three temperatures.

exponent (from 1.5 to 1.7) however the relatively good agreement between experiment and theory reinforces the identification of the exciton packet with a Bose-Einstein condensate.

As can be clearly seen in Fig. 34 the minimum packet size for a particular temperature increases with the temperature. Also the maximum average velocity (not shown) decreases as a function of temperature, although it is never less than about $0.5v_s$ which in LR theory is the minimum velocity for stable propagation. The origin of these physical facts is unknown; it may be related to a change in the initials dynamics which seems to determine the packet size as mentioned in the previous section or maybe related to the fraction of particles in the condensate. Fig. 36 plots the non-condensate fraction as a function of exciton density for three temperatures. The remarkable similarity of Fig. 36 to the experimental data in Fig. 34 (i.e. the reduction of the curvature and the increase in the non-condensed fraction, hence diffusive excitons, for increasing temperature) suggests a link between the latter hypothesis and the observed behaviour.

In our experiments we have only tracked as a function of temperature the higher of the two transitions mentioned in Sec. 3.1.3. The lower intensity transition, which seems easier to relate to the critical density for BEC, remains hidden in the noise or is perhaps non-existent since the data was collected with Nd:YAG excitation (see Sec. 3.1.3). Even with $\lambda = 585$ excitation the lower transition would be extremely difficult to pin down at

temperatures above 2.5K due to the very low signal amplitude and larger noise contribution in the variable temperature experiment.

3.1.5 Effect of Illuminated Area

By placing a variable sized pinhole in the path of the laser beam the effect of the size of the illumination area on the ballistic transport of excitons can be studied. This type of experiment was performed to investigate the initial dynamics of the exciton cloud before condensation and the conditions under which BEC occurs. The pinhole was positioned as close to the cryostat window as possible (~ 4 cm) to reduce diffraction

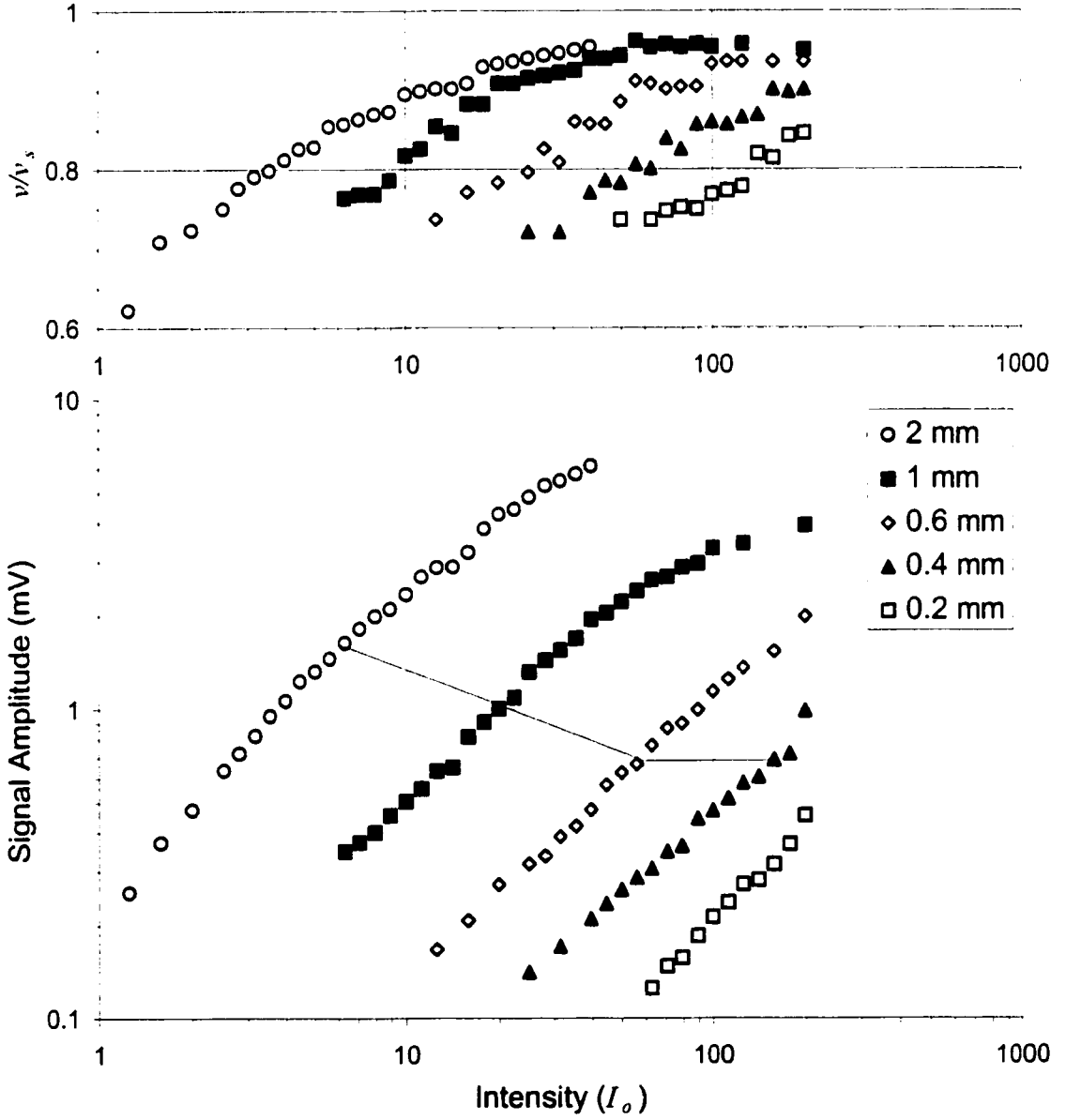

Fig. 37 Signal amplitude and normalized average velocity in a 2.2 mm thick crystal at $T = 2$K as a function of Nd:YAG laser intensity for the apertures indicated. The solid line is explained in the text.

effects. Even so the smallest pinhole (0.2 mm) may have projected a slightly smaller (~ 30% by diameter) and more intense (~ 20%) laser spot. These estimates are made from the results of a computer calculation of the Fresnel diffraction pattern for a slit of comparable size. The calculation also confirmed the absence of diffraction effects for the larger apertures. Since the aperture built into the sample holder was 2 mm in diameter no pinhole was used for that size.

Figure 37 shows the signal amplitude and normalized average velocity for the five apertures used in the experiment. From the figure it is evident that as the aperture size is reduced both the amplitude and velocity curves are shifted to the right to higher intensity, but unlike the shifts in Fig. 34 due to increasing temperature, the minimum packet size in the direction of propagation remains approximately constant as seen in Fig. 38. It would seem that the transport mechanism (diffusive versus ballistic) is a function of the illuminated area and not just the laser intensity. As expected the signal amplitude tracks are separated by approximately the square of the aperture ratio in all of the cases, except

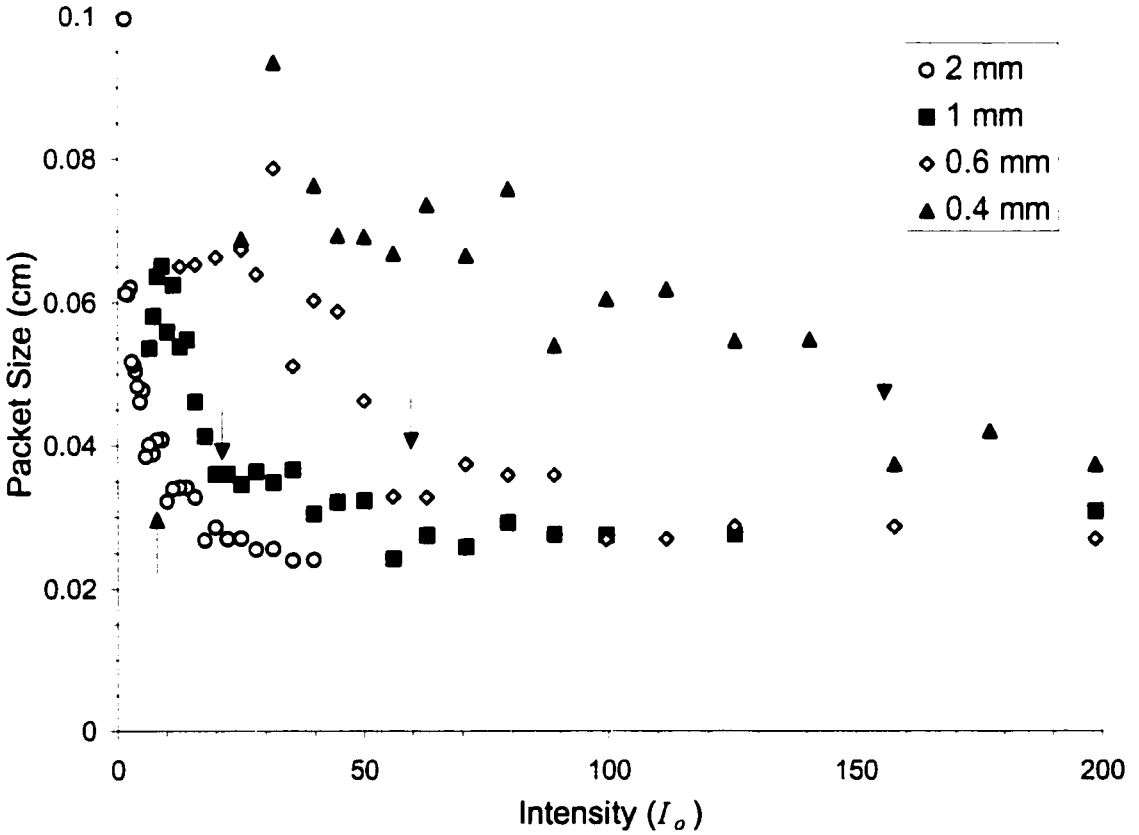

Fig. 38 Packet size in a 2.2 mm thick Cu_2O crystal at $T = 2K$ as a function of Nd:YAG laser intensity for the indicated aperture. Vertical arrows denote the critical intensity for each laser aperture.

for the smallest pinhole. The solid line in Fig. 37 crosses the position of the upper critical intensity on the signal amplitude track for each aperture which was found by the usual method shown in Fig. 38. No critical intensity could be determined for the smallest pinhole since the intensity was limited to $200I_o$ so as not to burn the sample. The absence of the transition is not surprising in light of the trend of the vertical arrows seen in Fig. 38.

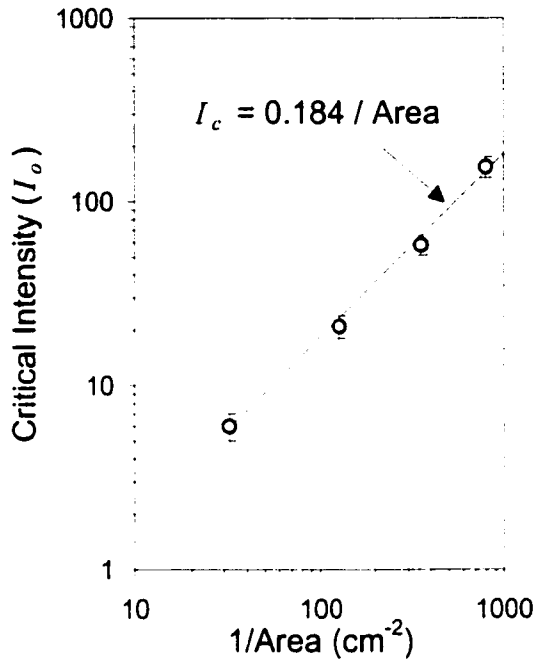

Fig. 39 Critical intensity determined in Fig. 38 as a function of inverse laser beam area. The solid line is a fit using the displayed equation.

The aforementioned trend is very nearly linear as seen in Fig. 39, the critical intensity being directly related to the inverse illuminated area. This figure leads us to one of two conclusions: either the critical density for BEC is function of the illuminated area, or what in our opinion is correct, the critical density is constant and therefore the initial number of excitons in the condensate (i.e. $I_c A$) is constant (= 0.184) as a function of illumination area. The latter interpretation leads us to conclude that the initial exciton distribution must undergo a lateral expansion to achieve a constant lateral cloud size and hence constant critical density. We believe that this expansion is occurring during transport and it seems that for fully ballistic transport a cylinder the length of the sample and perhaps 3 mm in diameter must be filled with a low density (~ 10^{15} - 10^{16} cm^{-3} although this is still much greater than the initial "vacuum") of non-condensed excitons. The presence of the large exciton background will be revealed experimentally in the following sections. The rationalization above does not preclude a short-lived condensate occurring at the lower critical intensity, independent of aperture size, however we can not verify this event.

We note that the lateral condensate size is still unknown since we have dealt only with ratios above, but we feel that the condensate will likely form only in the center portion of the large cloud where the density will always be higher, in fact: as mentioned

above the solid line in Fig. 37 intersects the signal amplitude track at the critical intensity for each aperture. The signal amplitude at the critical intensity is related to the critical density of the packet and the packet cross section as shown in Eq. (35). If we assume that the density is the same in all the pinhole cases (i.e. the critical density for BEC), the slight slope of the aforementioned solid line for the three largest apertures indicates that the lateral size of the packet arriving at the detector is changing slightly as a function of laser aperture. Since the two smallest apertures produce the same signal we believe that their diameters are linked to the minimum packet lateral width. Thus we believe the condensate at its smallest is an approximately 400 μm diameter sphere. For a 2 mm illuminated area the condensate likely forms an ellipsoid with minor axis 400 μm in the propagation direction and a major axis of ~ 600 μm in all directions perpendicular to propagation. The latter major axis was calculated from the square root of the signal amplitude ratio for the 2 mm and 0.6 mm apertures at the respective critical intensity.

3.1.6 Lateral Interference

We will now present results which are precursors to the effects that will be examined in greater detail in Sec. 3.2. This section bridges the gap between the study of an isolated condensate and interacting condensates. In order to study the lateral interaction between two exciton condensates and any possible coherence effects, the standard pulsed laser experiment described in Sec. 2.4.3 was performed with a slit assembly in the path of the beam. Results obtained using pinholes with areas equal to one and two slits will also be shown to serve as a baseline. The illumination configuration is shown in Fig. 40: the slit assembly was placed as close as possible (~ 4 cm) to the cryostat window to reduce diffraction effects. Using this arrangement a single laser beam is split into two components creating two exciton clouds side by side and the time resolved signal

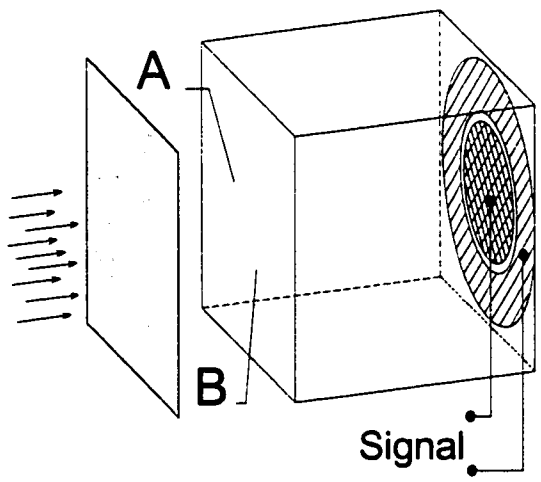

Fig. 40 Slit configuration for lateral interference experiments. For a particular pulsed laser intensity three traces can be recorded: slit A alone, slit B alone or trace C when slit A and B are simultaneously illuminated. The slits are 0.3 mm wide by 1 mm high.

resulting from the transport of two exciton clouds was measured. The time resolved signal for a one illuminated slit was recorded by blocking the other slit with a mask in front of the slit assembly. The mask consisted of two straight edged strips of thin sheet metal affixed to a fork shaped post on a translation table. The two strips were separated by a distance slightly larger than the widest slit separation so that for a small displacement one strip could block the left slit and for an opposite movement the other strip could block the right slit. A neutral position allowed both slits to be illuminated.

The narrow slits (0.3 mm) and small slit separations (0.5 mm to 1.7 mm) were very difficult to fully mask with certainty since the restricted space (crowded by the cryostat, slit assembly, mask, laser beam mirrors and lenses) made using a viewing loupe impossible. Furthermore the glare from the laser pulses and various shadows reduced the contrast. In addition equalizing the intensity falling on both slits and correctly positioning the slit over the center of the sample holder aperture were difficult and tedious tasks accomplished by trial and error. The main difficulty stemmed from the fact that the actual projections of the beam on the sample surface were blocked from view by the slit assembly and positioning of the beam and slit were done using the output signal. However after several attempts good results with equal signals from the individual slits, in most cases, were obtained.

The results for three laser intensities above or near the critical intensity required for ballistic transport and for five slit separations are shown in Fig. 41. For each of the fifteen combinations three traces were recorded: trace A for one slit, trace B for the other slit and trace C for both slits illuminated. In Fig. 41 trace C and the average of traces A and B are displayed. As mentioned above equalizing trace A and trace B was a difficult task especially for low signal amplitudes and a factor of 2 difference (in the trace amplitude) is present in some of the low intensity data. Amplitude differences in the high intensity data was more on the order of 20%. The intensities used in this experiment are very high as compared to the upper critical intensity found Sec. 3.1.3; however they are in line with the results of Sec. 3.1.5 since the slit area (0.3 mm^2) corresponds to the area of a 0.6 mm pinhole for which an upper critical intensity of $\sim 60 I_o$ was found.

Comparing the lower trace in each pair (the average of trace A and B) to trace C in Fig. 41, we see that the amplitude of trace C is always at least 2.5 times larger, in fact the

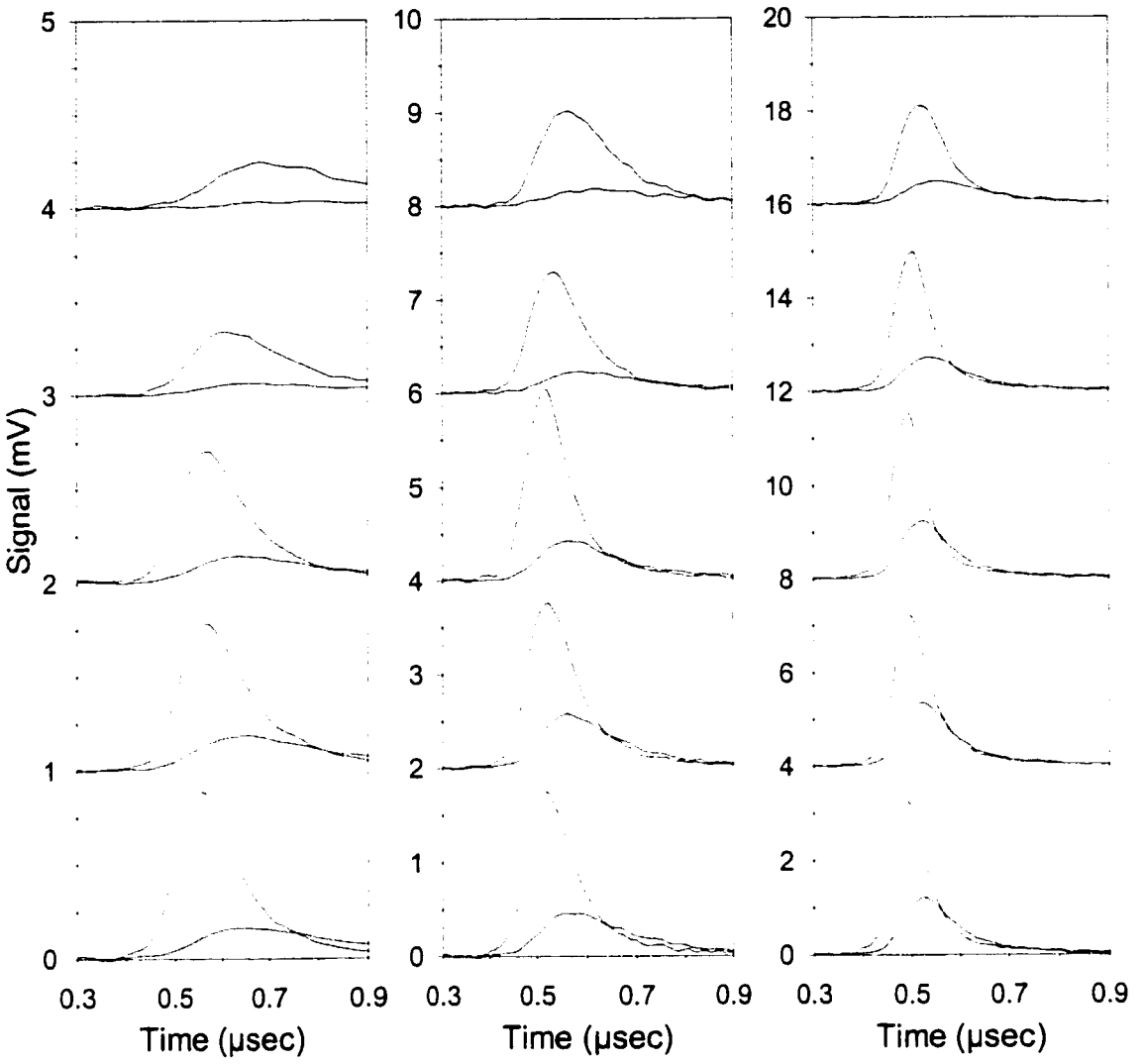

Fig. 41 Excitonic flux from single pulse illumination (λ = 532 nm) with a slit aperture for a 1.97 mm thick Cu_2O crystal at T = 2K. For each pane the laser intensity was (from left to right): $35I_o$, $70I_o$ and $140I_o$. Pairs of traces for five slit separations (from bottom 0.5 mm, 0.75 mm, 1 mm, 1.2 mm and 1.7 mm center to center, slit width 0.3 mm) are shown vertically displaced for clarity. In each pair the smaller amplitude trace is the average of traces A and B (single slit) and the other is trace C (double slit).

apparent amplification seems to grow (up to a factor of ~ 5) as the single slit trace amplitude diminishes. In addition trace C is always faster than trace A or B, a simple sum or sum and amplification can not reproduce the observed signal.

We have seen however an increase in signal amplitude and packet velocity for an increased aperture area in Sec. 3.1.5. Therefore for comparison to Fig. 41, Fig. 42 shows the results for similar intensities but instead of a slit obstruction, pinholes with an area approximately equal to the single and double slit were used. The area of the 0.8 mm diameter pinhole is 0.5 mm^2, nearly equal to the area of two slits: 0.6 mm^2. The three

highest intensity traces ($30I_o$, $60I_o$ and $120I_o$) for the 0.6 mm pinhole in Fig. 42 are very similar to the three corresponding traces ($35I_o$, $70I_o$, $140I_o$) for the smaller slit separations, but for all three intensities the 0.8 mm pinhole result is lower in amplitude than trace C in Fig. 42. We conclude that the enhanced signal is due to a constructive interference between the two packets which leads to the formation in the center of either a larger (in lateral size) or denser packet than the algebraic sum. This conclusion implies that the two packets are coherent, again reinforcing the identification of the ballistic packet with a Bose-Einstein condensate of excitons. As of this writing it is unclear at which point in time after condensate formation the proposed fusion occurs.

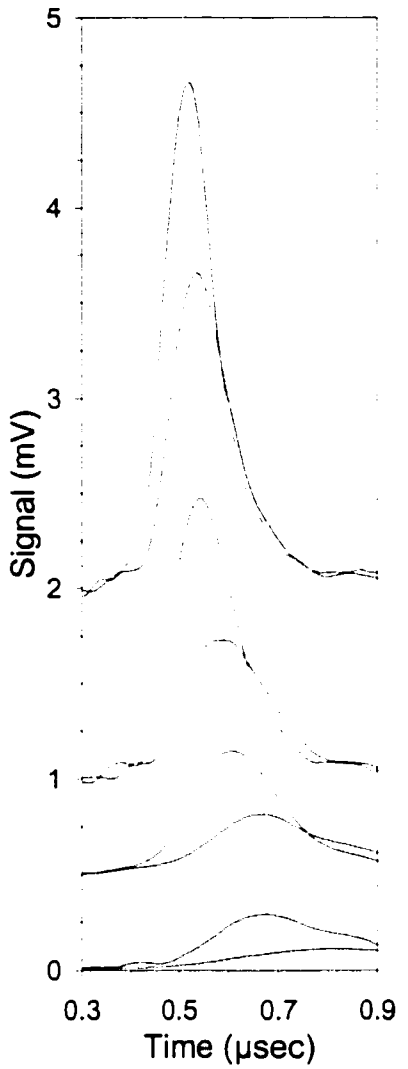

Fig. 42 Excitonic flux from single pulse illumination (λ = 532 nm) through a pinhole for a 1.97 mm thick crystal at T = 2K. For each pair of vertically displaced traces the laser intensity was (from bottom): $15I_o$, $30I_o$, $60I_o$ and $120I_o$. The pinhole diameters were: 0.8 mm (top trace in pair), and 0.6 mm (bottom trace).

The amplitude of trace A or B decreases as the slit separation increases (except for the smallest separation). This drop is due to the intensity variation of the laser beam as a function of radius and has been verified by a calculation not shown here. The slightly lower amplitude than expected for the 0.5 mm separation is most likely due to over masking (i.e. while masking slit A, slit B was also partially blocked). The variation of single slit trace amplitude as a function of separation and the variation of the double slit trace amplification as a function of input amplitude made a detailed analysis of the amplification as a function of slit separation very difficult. By using non-linear interpolation to correct the amplification as function of input amplitude, no significant change in the amplification as a function of separation between the slits was found. This may only means that we are experimentally unable to attain a separation large or small enough to witness a change in the lateral interaction (i.e.

the condensate wave functions always or never overlap). However to indisputably ascertain this conclusion the experiment would have to be repeated with a more even laser beam intensity profile.

The mechanism behind the increase in the amplification as the single trace amplitude is reduced is the non-linear increase in the ballistic propagation as a function of intensity as seen in Sec. 3.1.3 (i.e. a doubling of the number of particles has a different effect depending on the number of particles already present).

3.2 Sequential Collinear Excitation

3.2.1 Longitudinal Interference

In order to further study the interaction between two condensates the experiment described in Sec. 2.4.4.1 was performed. Since our measurement system is time resolved and not spatially resolved the results from this type of experiment are much easier to interpret than the aforementioned lateral interference results, and a theoretical model (Sec. 1.6) was developed to simulate this experiment. Results from the simulation will be shown below to confirm the relevance of the model.

The beam arrangement shown in Fig. 43 produced two identical exciton condensates from pulses A and B, but instead of interacting laterally (i.e. direction perpendicular to propagation) as in Sec. 3.1.6, the condensates interact longitudinally. As explained in Sec. 2.4.4.1 the variable time delay δt between the laser pulses equates to a variable initial distance between the condensates, which would in the absence of any interactions remain constant since the velocities are matched. Therefore signal measured from two non-interacting condensates would be the mathematical sum of traces A and B. However when both pulses sequentially illuminate the sample "trace C" is measured and it is not always simply equal to the mathematical sum indicating that an interaction has taken place between the two condensates while they were propagating across the sample.

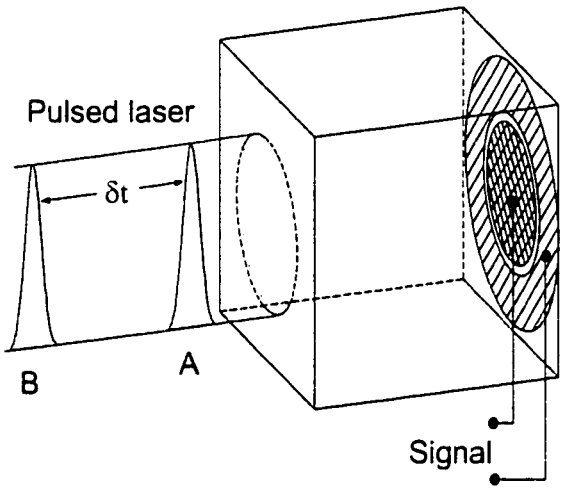

Fig. 43 Illumination configuration for longitudinal interference experiments. For a particular pulsed laser intensity three traces can be recorded: pulse A alone, pulse B alone or trace C when pulse A and B sequentially illuminate the sample.

A subset of the complete results is shown in Fig. 44 to illustrate the main features of the condensate interaction between two packets created by identical $I = 6I_o$ laser pulses. Results for three judiciously chosen time delays of 19 nsec, 56 nsec and 407 nsec show the non-interaction, maximum attraction and repulsion, respectively, of the two condensates. Trace A is obviously identical for all three time delays although it is

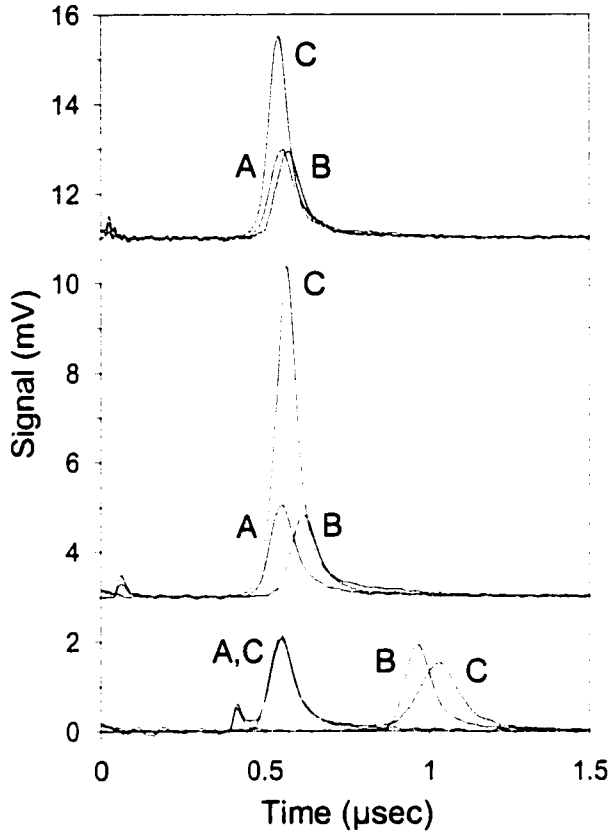

Fig. 44 Excitonic flux from single and double pulse illumination (λ = 532 nm, $I = 6I_0$) for a 2.2 mm thick crystal at T = 2K. For each triplet of vertically displaced traces the time delay was (from bottom): 407 nsec, 56 nsec and 19 nsec. In each triplet: trace A is from the main pulse, trace B from the delayed pulse and trace C from both pulses sequentially.

difficult to distinguish it from trace C in the 407 nsec case. Trace B is nearly identical to trace A except for the shift to later time with respect to the trace A fiducial. Trace C in the 19 nsec case is only slightly faster than trace A and approximately equal to the algebraic sum of A and B. The slightly higher velocity is due to the dependence of the packet velocity on the laser intensity as seen in Fig. 31. Therefore trace C in this case is similar to a trace resulting from a single $12I_0$ pulse.

In the 56 nsec case trace C is much larger than the sum of traces A and B, but arrives at a time between the two individual trace maximums. Since the packet velocity curve grows monotonically as a function of intensity any type of detector malfunction can be ruled out as the signal gain mechanism in trace C. We note that the increase in the number of excitons arriving at the detector does not necessarily violate the law of conservation of particles since as mentioned earlier a larger fraction of the particles do not normally reach the detector.

The final case is the 407 nsec delay; the first packet arrives at the detector undisturbed by the very recent injection of excitons at the opposite end of the crystal as can be seen by the overlap between trace A and the first part of trace C. The small signal (somewhat broadened by the Savitzky-Golay filter) just ahead the main packet is due to scattered light from the delayed pulse hitting the electrodes. The second packet is unmistakably retarded when propagating in the crystal occupied by another condensate.

There seems to have been a long range repulsion between the two condensates. The shape of the delayed packet has also changed to a slightly wider more symmetric shape, very well fitted on both sides of the maximum by a soliton as will be seen later. Incidentally, these results are exceedingly difficult to understand in the phonon wind picture; for example: why would the phonons slow down the excitons and broaden the distribution?

A more complete set of the data collected in this experiment is shown in Fig. 45; in this case only trace C is plotted as function of delay time for clarity. The trend in the data is evident: for small delays the signal is approximately the algebraic sum of the individual components and as the delay is increased the signal increases up to a

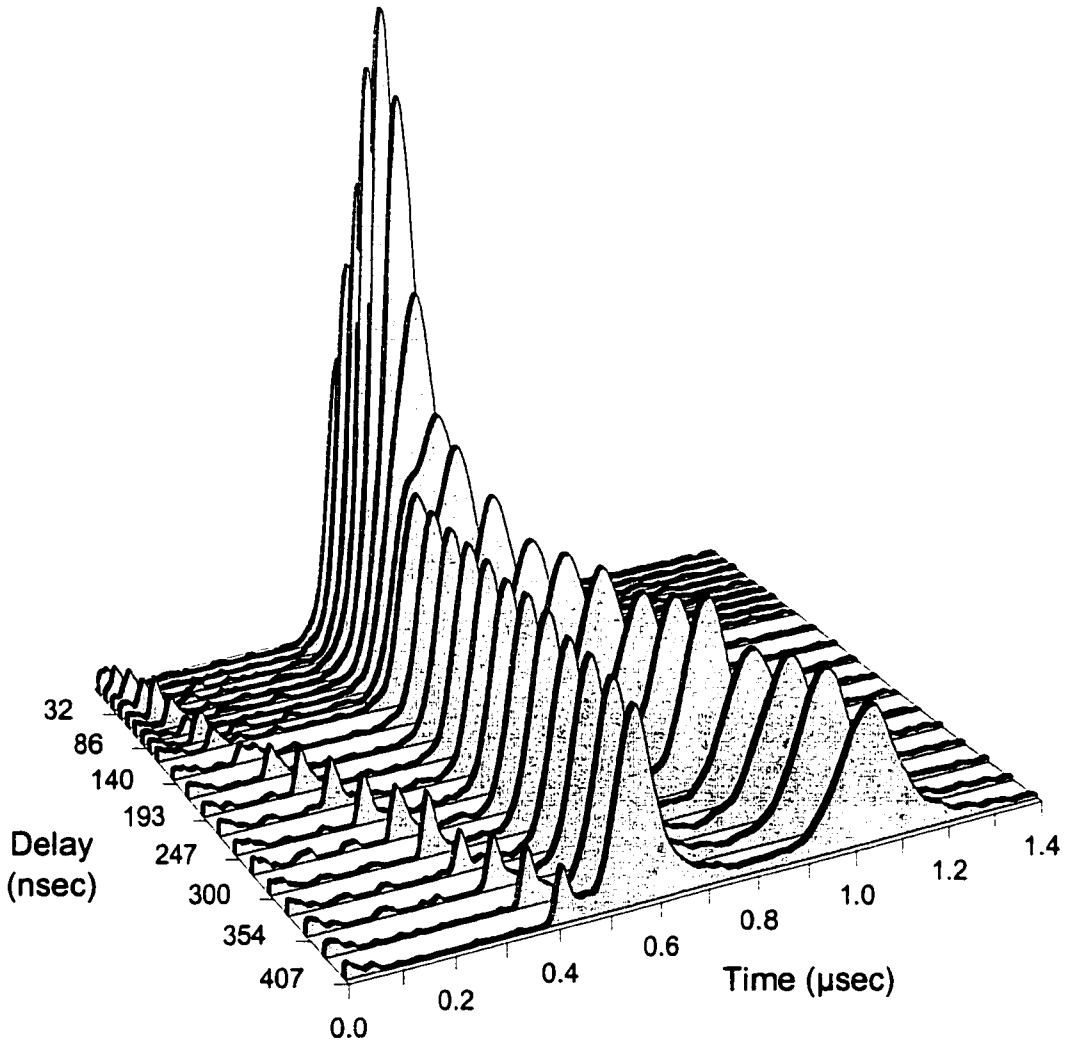

Fig 45 Excitonic flux from double pulse illumination (λ = 532 nm, $I = 6I_o$) for a 2.2 mm thick crystal at T = 2K as a function of secondary pulse delay time.

maximum at about 56 nsec. Afterwards the signal decreases as the two components separate and the second packet eventually spatially widens.

Using the longitudinal interference model described in Sec. 1.6, best fits to the data by χ^2 minimization with the constraints of transit time and pulse duration given by the experimental results (left side of Fig. 46) lead to a signal equal to $|\Psi|^2(x, t)$ plotted on the

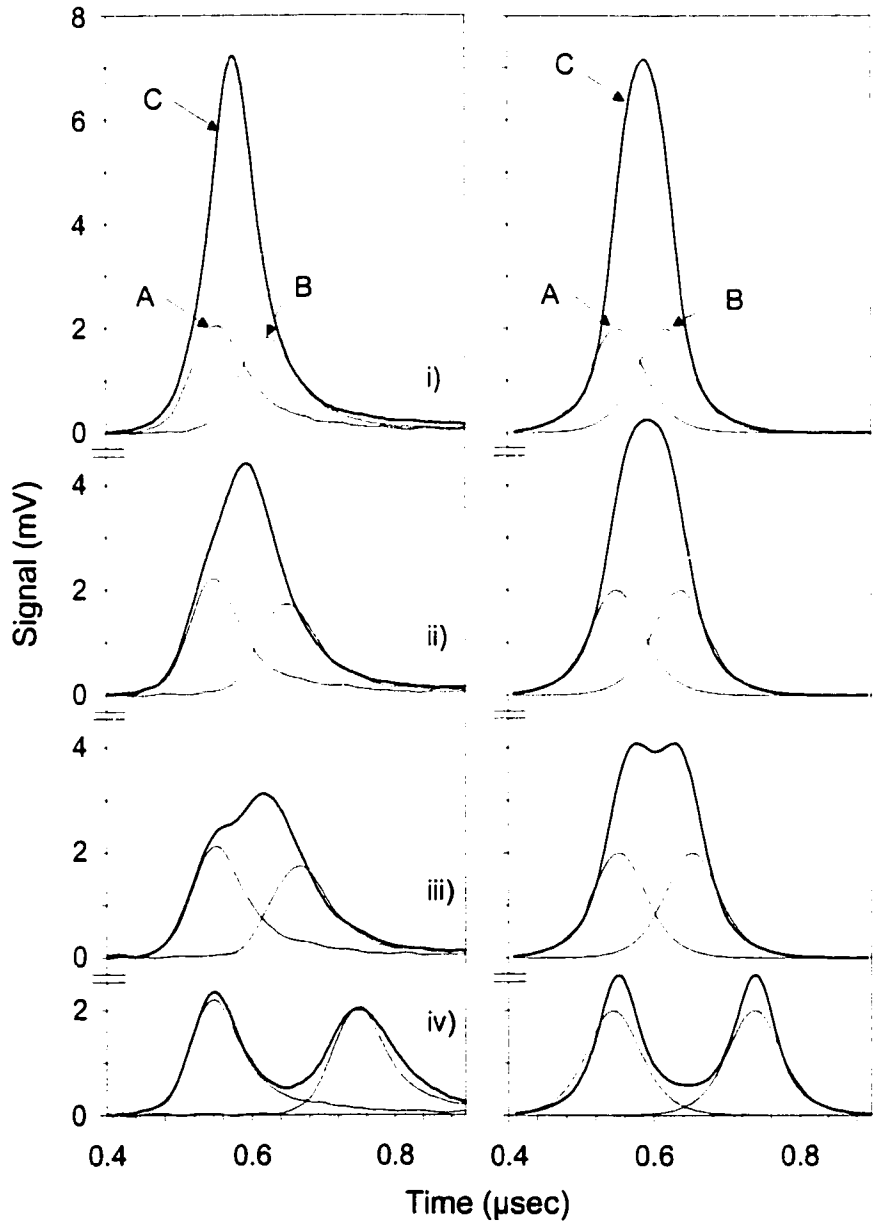

Fig 46 Excitonic flux (left pane) and simulated data (right pane) for single and double pulse illumination (λ = 532 nm, $I = 6I_o$) for a 2.2 mm thick crystal at T = 2K. Results for four time delays (from top): 64 nsec, 86 nsec, 100 nsec and 193 nsec are vertically displaced for clarity. Traces A and B are from single pulse illumination and trace C is from both pulses sequentially.

right side of Fig. 46. As can be seen, the signal obtained by the model resembles the shape of trace C under sequential excitation. The amplitude of the simulated packet and the experimental trace C are plotted in Fig. 47. The fast decrease of the amplitude as a function of delay with δt > 60 nsec is again well fitted by the model. A numerical solution of the NLSE (Eq. (26)) also predicts the spatial fusion of packets after a propagation distance comparable to the sample thickness. However, these simulations are only qualitative (for instance, an excitonic mass 150 times less than the free electron mass was used in Eq. (26)): a proper treatment of the problem would require a three dimensional case, the inclusion of phonon-mediated interactions as well as the contribution due to thermal, non-condensed particles. The simulations nevertheless unravel a key point, that interference between coherent wave functions is essential to reproduce the results. Since the incident laser photons produce hot carriers which relax into n = 1 excitons by dissipating their extra energy (ΔE ~ 340 meV) via cascade emission of a large number of phonons, this coherence is not transferred from the laser to the excitonic ensembles. Coherent excitonic waves can only emerge through a self-organization process such as ingrained in a BEC process.

The essential role of interference between coherent wave functions is further strengthened by inspection of the results between $\delta t = 0$ and $\delta t = 60$ nsec in Fig. 47, a time interval not considered in the numerical model. Here, the magnitude of signal C increases, despite the

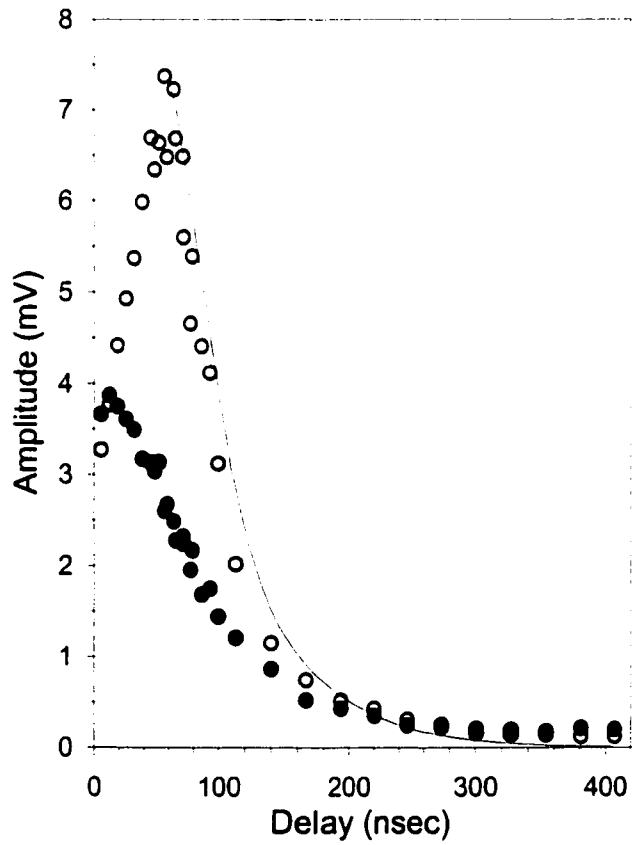

Fig 47. Amplitude of trace C (open circles) and of the sum of traces A and B (closed circles). The signal amplitude in both cases was measured at the time $t_{max} + \delta t/2$ where t_{max} is the maximum of A and δt is the delay. The numerical results from the theoretical model are shown as a solid line.

fact that the overlapping particle density decreases due to packet expansion. This clearly indicates that attractive interactions alone cannot explain the nonlinear signal: coherence is a crucial additional ingredient.

We attribute the rise of the nonlinear signal in the interval 0 - 60 nsec to the build-up of a common phase between the soliton wave functions. As mentioned in Sec. 2.4.2 all of the time resolved exciton flux traces shown in this work correspond to multishot recordings, typically averaged over 100 pulses to improve the signal-to-noise ratio. Thus, no interference signal is expected upon multishot integration if the relative phase between the two condensates fluctuates randomly for each realization.[38] This is what is indeed observed at time $\delta t \sim 0$, where C ~ A + B despite the fact that the particle density is at a maximum. Instead, there is build-up of the signal as the two exciton-phonon solitons gradually assume their stable shape and acquire a common phase via exchange of particles. Complete mutual coherence, implicitly assumed in Eq. (27) is achieved after a time interval comparable to the expansion time of the packet from its initial to its final thickness ($\delta t \sim \delta l / v_s \sim 70$ nsec).

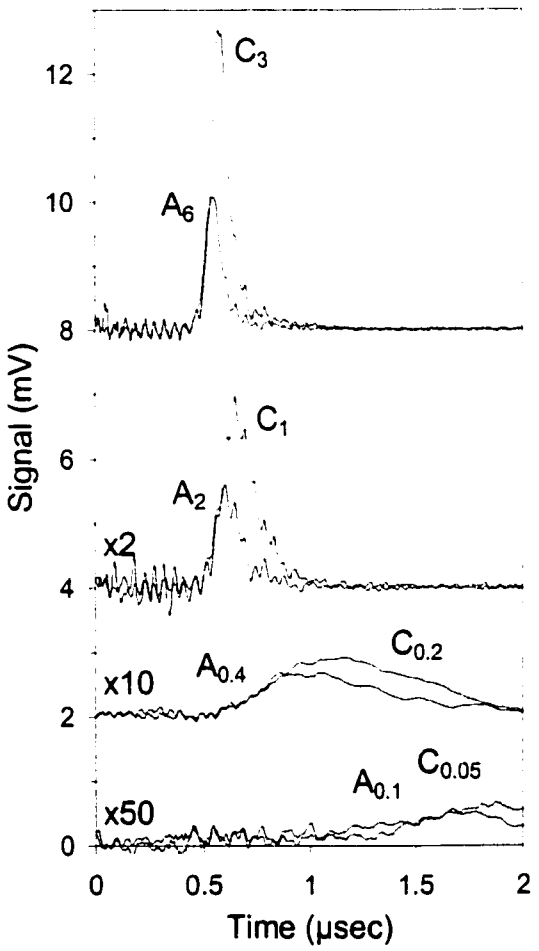

Fig 48 Excitonic flux for single and double pulse illumination (λ = 532 nm, δt = 59 nsec) for a 2.2 mm thick crystal at T = 2K. Each trace is labeled A for single pulse or C for double pulse, the subscript indicates the laser intensity in units of I_o. The bottom three pairs of traces were vertically scaled by the factor indicated on the left.

We have verified the absence of interference effects for low density packets (i.e. non-condensed) created by low intensity laser pulses separated in time by 59 nsec; this time delay corresponds to the maximum seen in Fig. 47. Fig. 48 demonstrates that as the laser intensity is lowered, the difference between the double pulse trace C and a single pulse trace A at double the

intensity, decreases. For the two lower pairs of traces in the figure the difference in amplitude is small or negligible. Comparing trace C to trace A with double the intensity ensures that the number of excitons in the system is equal and any increase in the signal of trace C indicates constructive interference between two condensates. The slight enhancement of trace $C_{0.2}$ as compared to trace $A_{0.4}$ indicates a stable condensate forms approximately at $0.2I_o$; this is consistent with earlier estimates in Sec. 3.1.3.

3.2.2 Weak Delayed Pulse

The results shown in this section will demonstrate the hypothesis put forward in Sec. 3.1.3: that a large number of excitons are left behind the packet in the crystal volume. Here the same pump/probe double pulse experiment described in the preceding section was performed except that the intensity of the delayed beam B was much less than the main beam A.

Results for the three time delays (again aptly chosen) are presented in Fig. 49 to illustrate the three behavioural regimes. In all three cases trace B appears as a flat line since the laser intensity of beam B is 30 times less than beam A; trace A remains constant with the same signal magnitude as in the previous section. Trace C for the 19 nsec delay shows only a small gain of signal over trace A due to the slightly greater total number of particles injected. However for the 56 nsec delay trace C is more than double the amplitude of trace A; the gain in

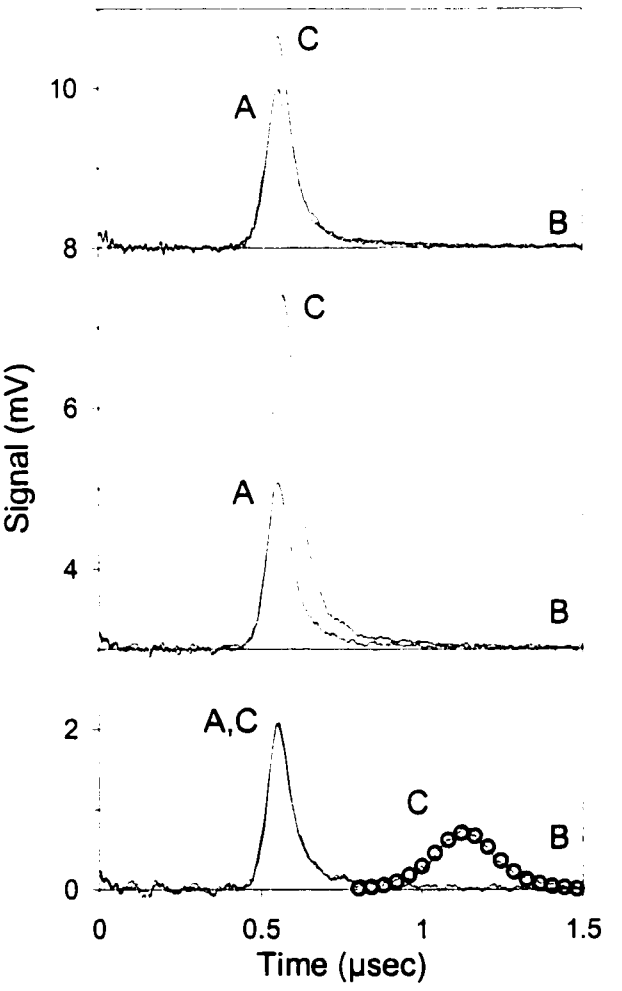

Fig 49 Excitonic flux for single and double pulse illumination (λ = 532 nm) for a 2.2 mm thick crystal at T = 2K. Traces A and B are for single pulse and trace C for double pulse. Three time delays are shown (from top): 19 nsec, 56 nsec and 407 nsec. The laser intensity for beam A is $6I_o$ and for beam B it is $0.2I_o$.

signal can not be accounted for by the additional particles deposited by beam B. We believe that when packet A reaches the detector it may only contain ~ 3% of the total number of excitons injected by beam A. Therefore packet C would contain 3% of beam A and nearly 100% of the particles created by beam B, explaining the large apparent gain.

Since the intensity of beam B is near the lower threshold for condensate formation (i.e. a short lived condensate may be present) we can not determine the exact mechanism behind this apparent gain; it could be the longitudinal interference effect described above, or amplification by stimulated emission of excitons as explained in Sec. 1.7 and to be further explored in Sec. 3.3, or a combination of both.

When the time delay is 407 nsec a second distinct packet of significant amplitude appears. Its shape is that of a soliton traveling at about $0.7v_s$ as demonstrated by the fit (open circles) in Fig. 49. A theory developed by Hanamura and supported by our experimental facts, explains this result [39, 40]. Briefly, the low intensity probe pulse generates a low density cloud of excitons that attracts other non-condensed excitons left

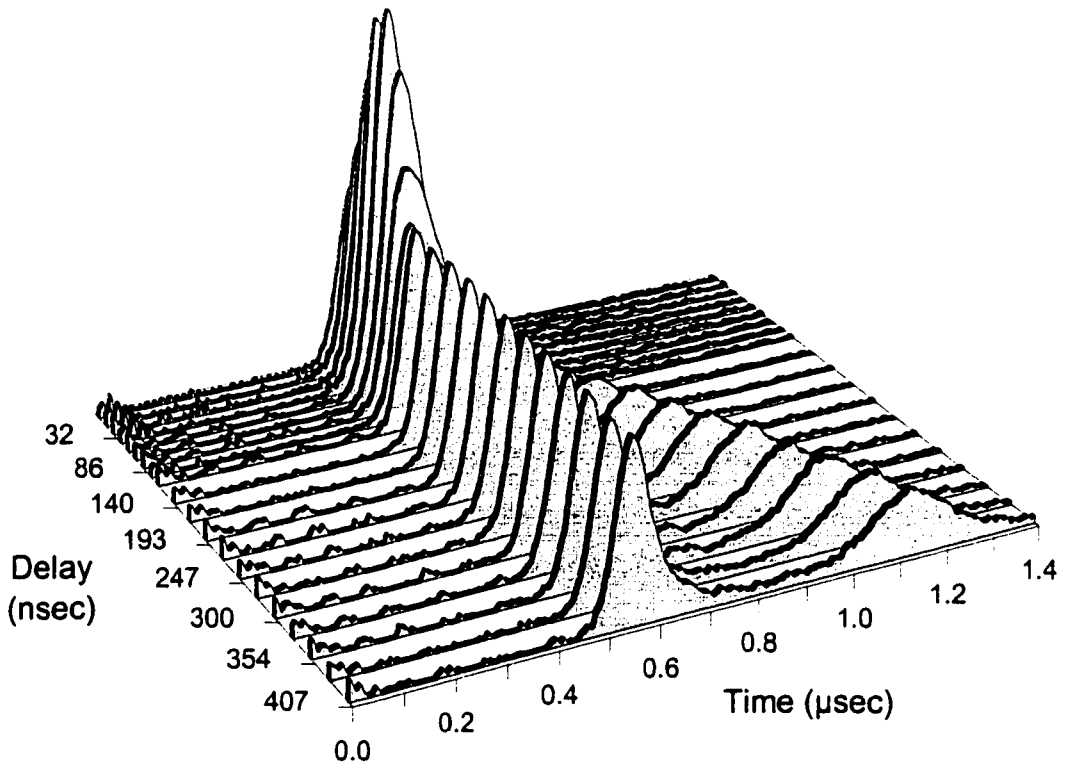

Fig 50 Excitonic flux from double pulse illumination (λ = 532 nm, $I_A = 6I_o$ $I_B = 0.2I_o$) for a 2.2 mm thick crystal at T = 2K as a function of secondary pulse delay time. The vertical scale is identical to Fig. 45.

in the crystal volume by the pump beam and grows into a substantial condensate which under these conditions assumes the shape of a soliton.

The complete set of results for many time delays are shown in Fig. 50. The maximum signal amplitude for this set is plotted in Fig. 51. From Fig. 50 we can see that as the time delay is decreased from its maximum value the soliton approaches the main packet. In Fig. 51 the maximum amplitude tracks the first packet as it is always larger than the soliton amplitude. In both figures we see that for a delay $\delta t \sim 100$ nsec the two packets start to merge into a single entity, and the combined packet amplitude reaches a maximum near 60 nsec. For shorter time delays the combined packet amplitude quickly diminishes to the amplitude of trace A alone. We feel the appearance of the maximum in Figs. 50 and 51, at the same time delay as the maximum in the previous section gives the longitudinal interference explanation an edge over the stimulated emission explanation as the responsible mechanism for the maximum.

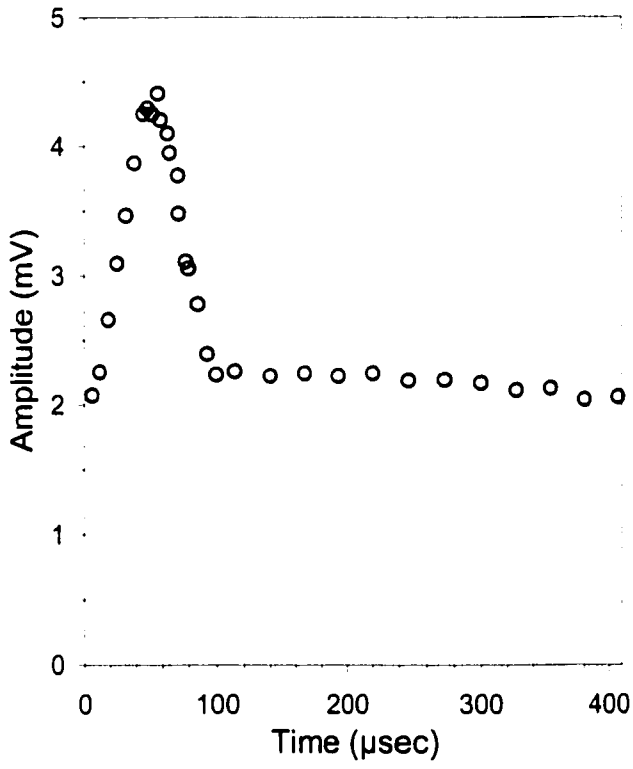

Fig 51 Maximum amplitude of traces shown in Fig. 50 as a function of secondary pulse delay time.

There seems to be an attraction between the two packets since the measured temporal separation decreases faster than the experimentally controlled time delay, or put another way, the velocity of the second packet increases when it is closer to the main packet. This will be graphically displayed in Fig. 57 in the following section.

3.3 Sequential Orthogonal Excitation

3.3.1 Amplification by Stimulated Emission of Excitons

We now investigate the interaction of the condensate with a "cold" population of non-condensed excitons distributed in the path of the traveling packet. Since the cold excitons are created by a pulsed laser the total number of excitons deposited and their density distribution (Eq. 19) are known as accurately as the absorption constant for Cu_2O at the exciting laser wavelength is known. This type of experiment coupled with the results to be presented in Sec. 3.4 will lead to a determination of the paraexciton lifetime.

Figure 52 shows the illumination geometry for the experiment described in Sec. 2.4.4.2. Beam A generates an exciton packet as usual and the smaller orthogonal aperture for beam B allows the center of the crystal to be instantaneously filled with cold excitons from the secondary laser pulse. In this section we will present results from this experiment performed as a function both of laser beam A and laser beam B intensity for a fixed delay time δt = 170 nsec between the two beams. This particular delay was chosen so as to deposit the cold excitons just before the arrival of the packet in the center of the crystal. Most of the results were obtained with a delayed laser wavelength of 605.6 nm, corresponding to the orthoexciton + Γ_{12}^- transition. Other wavelengths used were the orthoexciton quadrupole transition at 609.7 nm and some various wavelengths in the 607 nm to 604 nm region.

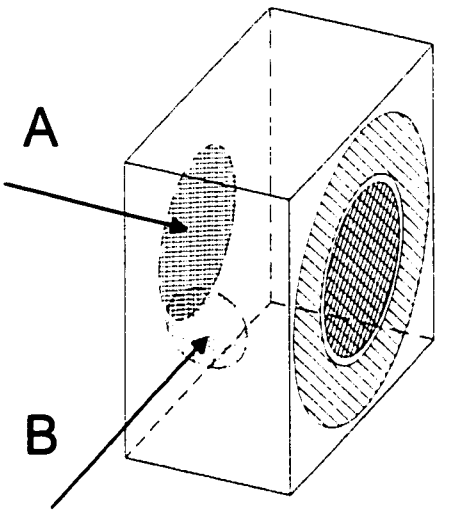

Fig. 52 Illumination configuration for orthogonal double pulse experiments. Pulse A is from the main Nd:YAG λ = 532 nm laser beam, while pulse B is from a variable wavelength dye laser. The arrival time of pulse B can be delayed with respect to pulse A.

A subset of the data collected with the delayed pulse at λ = 605.6 nm is shown in Fig. 53. The three intensities for beam A were chosen so as to be far above, far below and near the upper critical intensity found in Sec. 3.1.3. The traces recorded for beam A illumination only are not shown in the figure. The trace at the lowest intensity ($0.0009I_o$)

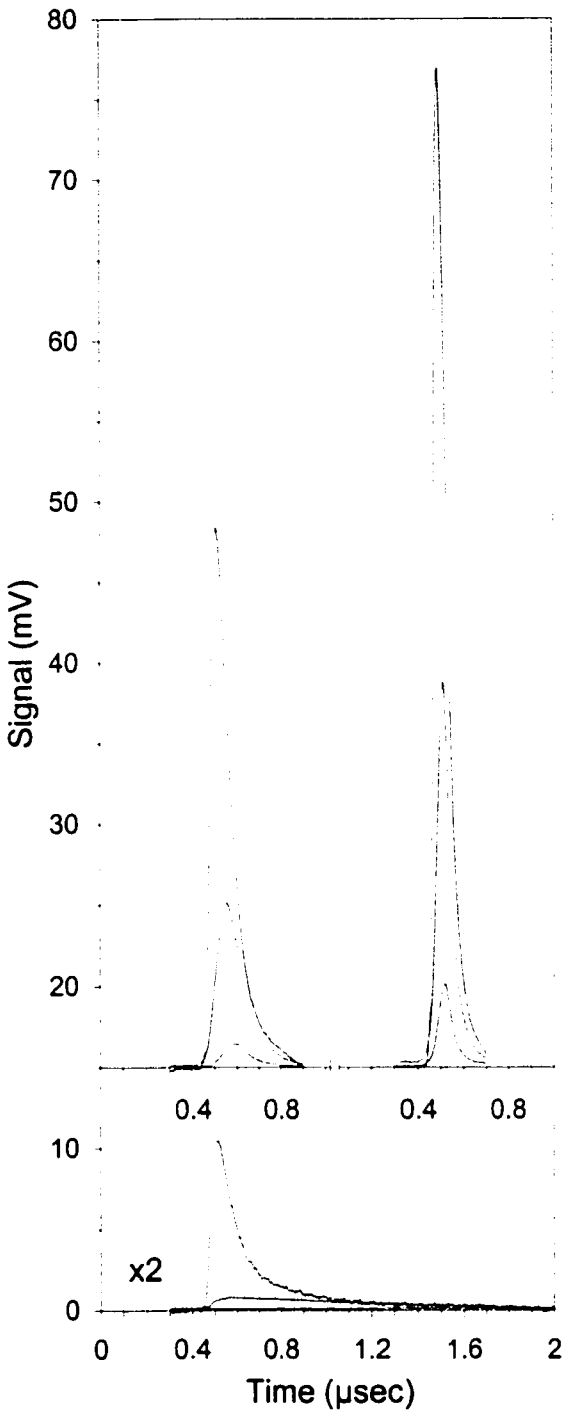

Fig. 53 Excitonic flux from orthogonal double pulse (δt = 170 nsec) illumination for a 1.97 mm thick crystal at T = 2K. Results for three main pulse (λ = 532 nm) intensities, top right: $20I_o$, top left: $4I_o$,and bottom: $0.2I_o$, as a function of orthogonal pulse (λ = 605.6 nm) intensity (from bottom in each set): $0.0009I_o$, $0.09I_o$ and $9I_o$. The bottom set is vertically scaled by a factor of 2, even so the lowest trace is nearly invisible

for the delayed beam B can be used in each set as a baseline substitute since they are nearly identical to the trace measured for beam A illumination only. Many more results at different beam B intensities were recorded but are not shown in the figure for clarity. The main feature that one immediately notices in Fig. 53 is the large effect that a relatively small number of cold excitons has on the packet amplitude (e.g. the $I_A = 20I_o$ trace is amplified by a factor of four in the $I_B = 0.09I_o$ case: this represents an extra exciton input of only 1%). Also in the $I_A = 0.2I_o$ case the orthogonal laser beam has caused the formation of a packet, albeit very asymmetric, where only a diffusive signal is normally found. The condensate which might have been present only for a small fraction of transit has been amplified in this case and easily completes the trek across the sample.

These large amplification effects quickly disappear if the orthogonal beam wavelength is tuned too far from the red absorption edge or off the orthoexciton quadrupole resonance. Later we will see a very similar critical laser wavelength dependence when the

orthogonal pulsed laser is replaced by a CW laser as the secondary exciton source (Sec. 3.4.3).

We believe that the very large gain in signal observed in this experiment is due to the stimulated emission of excitons into the packet as described in Sec. 1.7. However the reservoir of particles that are preferentially scattered apparently consists not only of the cold excitons injected by the orthogonal laser, since there are too few to account for the large signal, but also and maybe more importantly the large number of saturated thermal excitons created by the main pulse. These excitons, the coma and tail in the comet analogy, were never included in the condensate or expelled by it in a bid to maintain chemical equilibrium. However the introduction of another thermal exciton population in front of the condensate seems to invoke the stimulated emission of these excitons back into the condensate wave greatly amplifying it, or from another perspective reducing the losses.

Fig. 54 plots the peak amplitude of the packet for the three beam A input conditions shown in the previous figure as a function of beam B intensity. In the $I_A = 4I_o$ case data

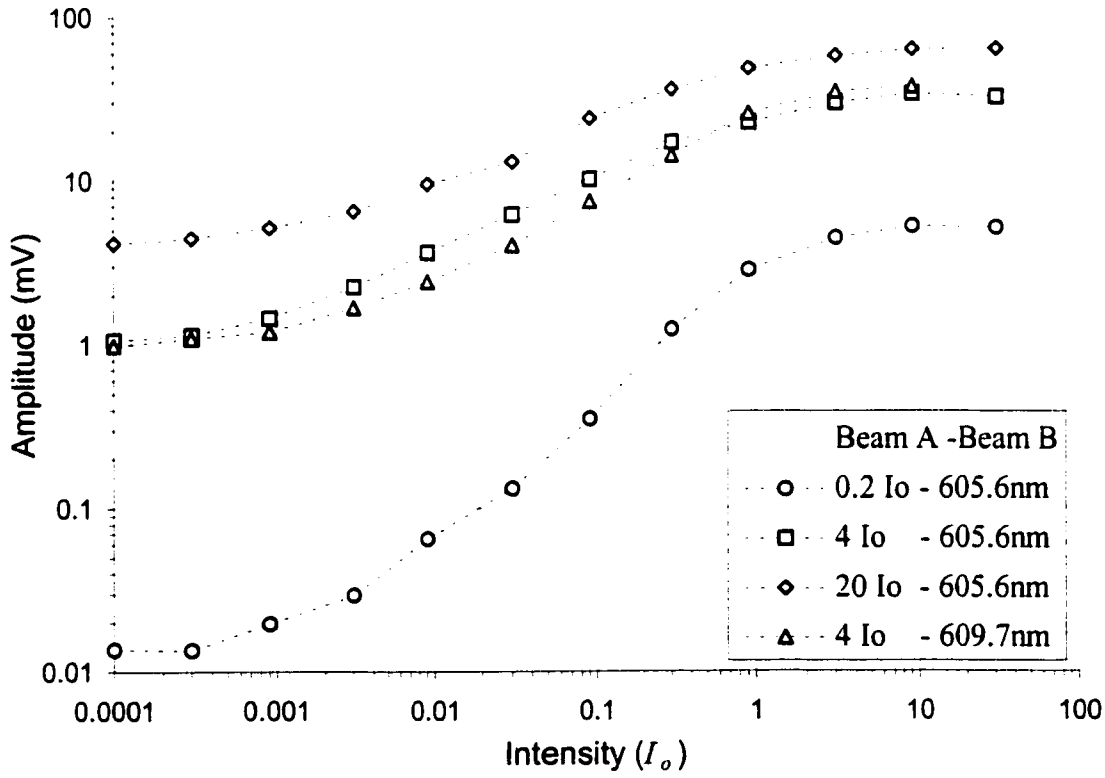

Fig. 54 Trace peak amplitude for orthogonal double pulse illumination as a function of orthogonal pulse intensity for a 1.97 mm crystal at $T = 2$K. The legend indicates the main beam ($\lambda = 532$ nm) intensity and the delayed ($\delta t = 170$ nsec) orthogonal pulse wavelength.

was recorded for two orthogonal beam wavelengths as indicated in the legend. Both data series are very similar indicating that the effective absorption coefficient must be approximately the same for both wavelengths. All the curves strongly saturate at the same I_B, although the maximum gain and saturation amplitude is different for all three input cases. The latter facts imply that the saturation is not due to the exciton detector but due to one of two other reasons. Either the thermal population created by beam A and beam B is exhausted and no other particles are available for stimulated emission, or a fraction of the excitons created by the orthogonal beam gather into a hitherto undetected condensate. We note that three experimental facts support the latter explanation. Firstly since the available number of thermal particles is proportional to the sum of excitons created by beam A and B why does the gain still saturate when beam B creates many more excitons than beam A? (i.e. in the case of $I_A = 0.2I_o$ and $I_B > 1I_o$). Secondly the intensity $I_B \sim 9I_o$ at which all the curves saturate corresponds to a density (see Fig. 6) very close to the critical density for Bose-Einstein condensation at $T = 2$K. Finally a close inspection of the two lower curves in Fig. 53 for the $I_A = 0.2I_o$ case reveals an anomalous tail which disintegrates at about 1.8 μsec. The significance of this tail will be amply clear in Sec. 3.4 where results with the sample simultaneously irradiated by a pulsed and CW laser will be presented.

3.3.2 Delay Time Dependence

In the preceding section we have reported amplification of an exciton packet after it has traveled through a cloud of thermalized excitons. If the delay of the orthogonal pulse is increased and the thermal excitons are deposited behind the packet no amplification should occur. We have measured the packet amplification as a function of time delay and the results are displayed in Fig. 55. As can be seen the packet amplitude slowly increases along with the time delay to a mild maximum coinciding with the arrival of the packet in the center of the crystal where the orthogonal beam deposits the excitons. The nearly constant amplification for smaller time delays is easily understood since the excitons are very long lived relative to the experiments time scale and only diffusion may reduce the density of the secondary cloud. The amplification quickly drops to one as the packet is progressively further afield confirming the initial hypothesis; however for large delays we are served a surprise.

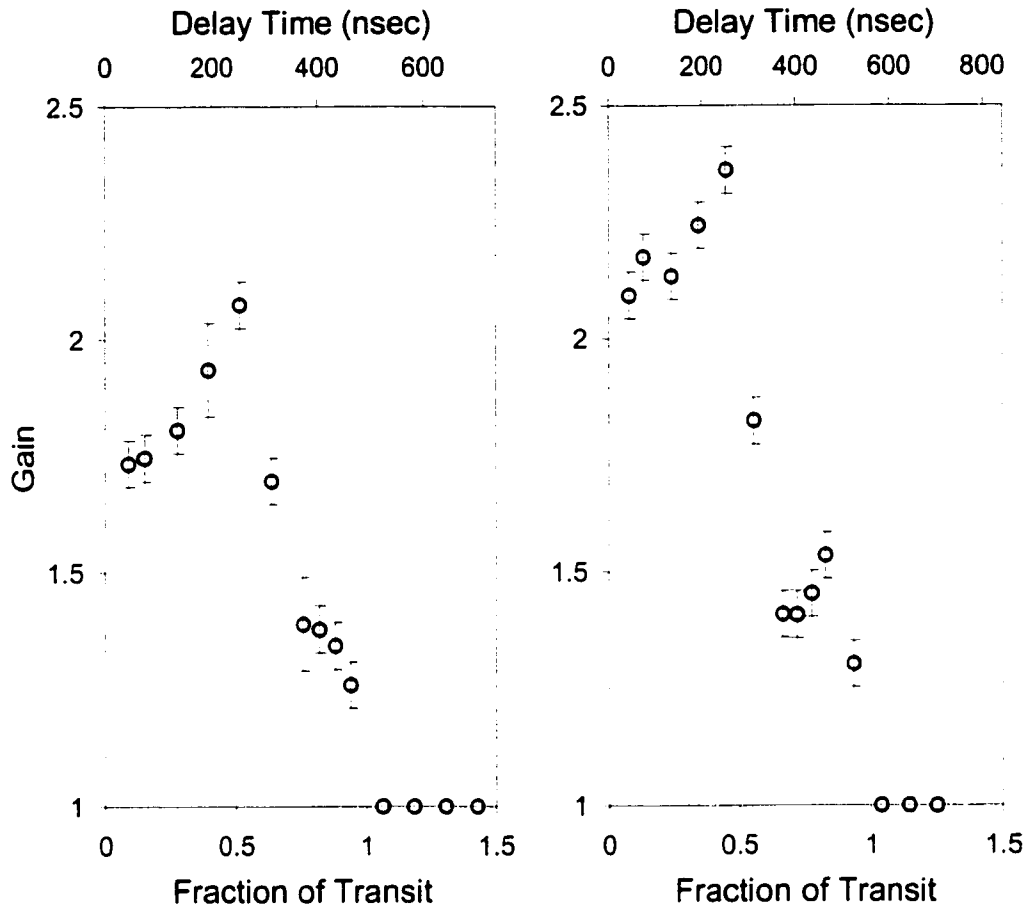

Fig. 55 Packet amplitude gain for orthogonal double pulse illumination as a function of orthogonal pulse delay time for a 1.97 mm thick crystal at T = 2K. The delay time is also expressed as a fraction of transit of the exciton packet. The λ = 532 nm beam intensity was (left pane) $63I_o$ and (right pane) $12I_o$. The orthogonal λ = 609.7nm beam intensity was $0.007I_o$.

A subset of the time resolved data used to construct Fig. 55 is shown in Fig. 56. The top trace in the figure (δt = 253 nsec) is wider than the input packet seen arriving unmodified in the bottom trace at 0.5 μsec. The reason for this broadening is made evident as the time delay is increased. For δt > 253 nsec the main packet diminishes in amplitude and temporal width and a second wider exciton packet emerges from its tail. The secondary packet is indeed a soliton as demonstrated by the fit of open circles in Fig. 56.

The two largest delays shown in the figure correspond to orthogonal laser absorption after the condensate has been measured at the electrode and presumably destroyed. The data indicates that the second soliton forms from the obviously considerable remains of the main packet and travels towards the electrode face. Recent

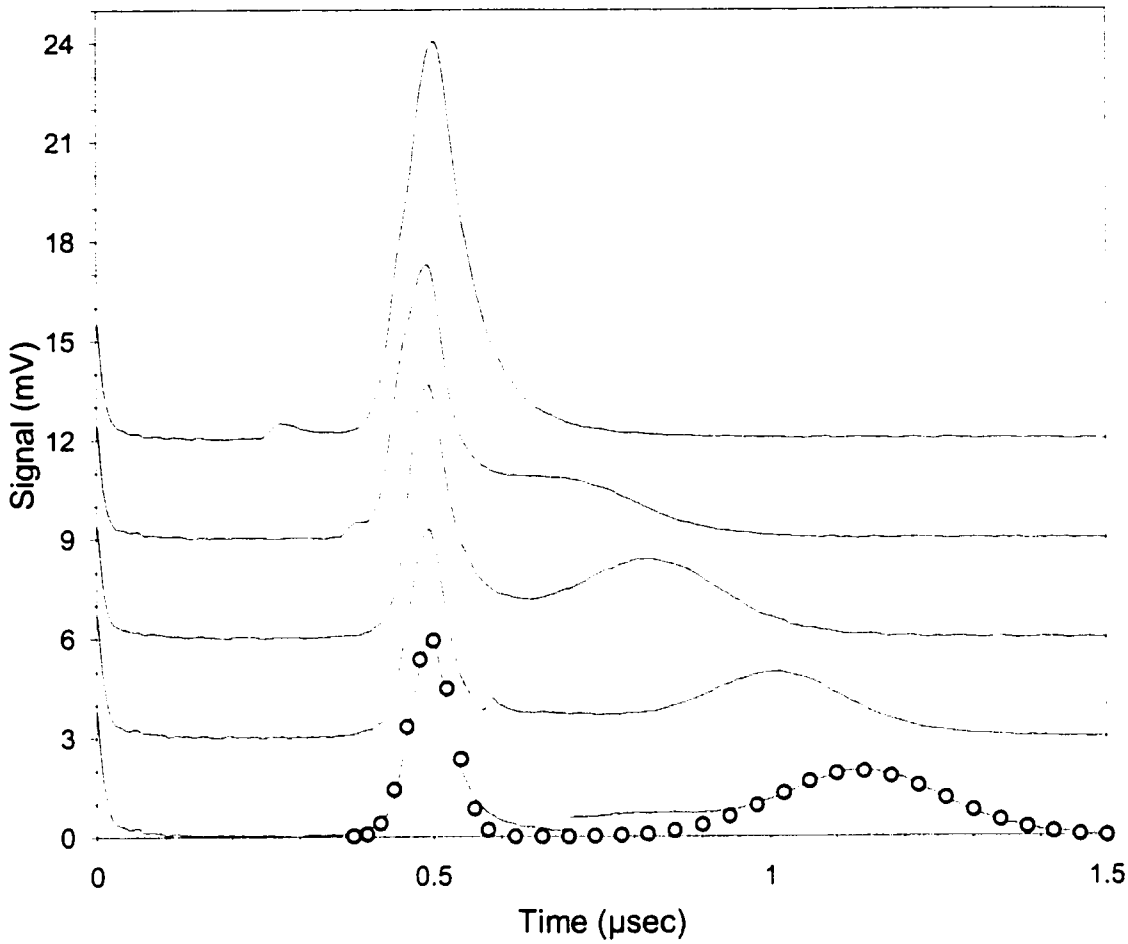

Fig. 56 Excitonic flux from orthogonal double pulse illumination for a 1.97 mm thick crystal at T = 2K as a function of orthogonal pulse delay time (from bottom): 703 nsec, 583 nsec, 463 nsec, 373 nsec and 253 nsec. The main pulse (λ = 532 nm) intensity was $63I_o$ and the delayed pulse (λ = 609.7 nm) intensity was $0.007I_o$. The open circles represent a soliton fits to the two packets.

experimental results not shown here reveal the effect continues for delays of at least 900 nsec. In addition a bridge of excitons seems to extend between the electrode face and soliton. This flux is quasi continuous indicating that it originates from a continuum of positions and ends with arrival of the soliton as if swept up by the packet. A similar behaviour will be observed with combined pulse and CW laser excitations in Sec. 3.4.

Assuming the spatial width in the propagation direction of equal amplitude solitons is constant (see Sec. 1.5), and comparing the temporal widths of the similar solitons from the sequential and orthogonal double pulse experiments, we can calculate the distance traveled by the second soliton in Fig. 56. Using the equations $v = \Delta d / \Delta t$ and $v = d / t_{max}$ where Δd is the spatial extent, Δt is the temporal width and t_{max} is the transit time with the parameters d = 2.2 mm, Δt = 0.22 μsec and t_{max} = 0.72 μsec in the sequential pulse case

(Figs. 45 and 46) we find Δd = 0.67 mm. In the orthogonal case (Fig. 56) with Δt = 0.3 μsec, t_{max} = 0.43 μsec (the arrival time minus the secondary pulse delay time) and using Δd from above we find that the distance traveled by the second soliton to be 1 mm. The second soliton seems to originate from the orthogonal pulse laser axis through the center of the crystal.

Using this distance the soliton velocity was plotted in Fig. 57 as a function of time delay along with data from the sequential double pulse experiment in Sec. 3.2.2. The overlap of the data series from the two types of experiments supports the result of the above calculation. The discontinuity in the data series is coincident with the arrival of the main packet at the detector face. Without the influence of the main packet the secondary soliton propagates at the same velocity nearly independent of the secondary pulse delay time. This indicates the exciton distribution in the crystal volume is unchanging for at least 0.4 μsec, if not much longer, (as mentioned above the effect was verified for a delay of 900 nsec) after packet detection and possible destruction due to the very long paraexciton lifetime. One may notice that the minimum velocity maintained by the soliton is $0.5v_s$, in agreement with LR theory with regard to the stability of a moving condensate.

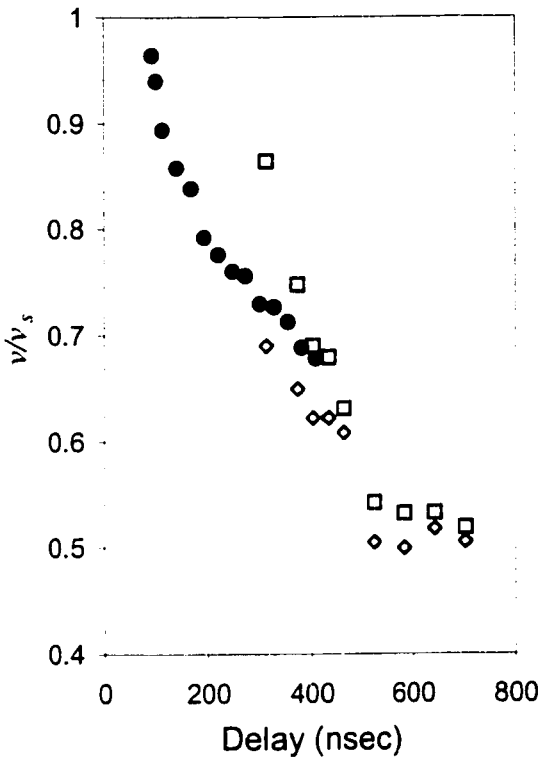

Fig. 57 Soliton packet velocity as a function of secondary pulse delay time. Filled circles were obtained from the data shown in Fig. 50 (collinear geometry, λ = 532 nm, $I_A = 6I_o$ and $I_B = 0.2I_o$). Open markers are from orthogonal double pulse excitation with λ_A = 532 nm, λ_B = 609.7 nm, $I_B = 0.007I_o$ and $I_A = 12I_o$ for the squares and $I_A = 63I_o$ for the diamonds. The distance traveled by the soliton in the orthogonal excitation case is assumed to be 1 mm.

The questions that still remain are: How does the soliton gain a velocity? And why does it propagate towards the electrode face? We note that the down conversion of the initially created orthoexciton (by the orthogonal laser) to a paraexciton principally creates a Γ_{12}^- optical phonon and absorbs a LA phonon due to conservation of energy. Therefore

the paraexciton must have a velocity commensurate with momentum conservation. Under normal circumstances the velocities are randomly distributed in all directions with a very small bias in the laser beam direction due to the small (in this case) photon momentum. But under the influence of an quantum saturated Bose gas leftover from the main pulse and perhaps just nudged over the edge of BEC by the extra influx of particles, the paraexcitons aligned themselves into the same state and hence propagation direction, to form a soliton.

But why towards the electrode? Perhaps the electrode or the exciton bridge mentioned above is seen as an attractive potential well. Or possibly the soliton forms along the main laser beam axis due to a predominance LA phonons from the main beam in this direction. Or solitons propagate in other directions and we do not measure them. Obviously further experiments will be required to answer these questions.

3.4 Pulse and CW Excitation

The results presented in this section will again deal with the interaction of the condensate with a "cold" population of non-condensed excitons distributed in the path of the traveling packet. However the method used for depositing the cold excitons is completely different from Sec. 3.3; in this case a CW laser of much lower intensity was used and to achieve significant excitons densities we rely on the fact the average steady state exciton density n is related to the paraexciton lifetime

$$n = \frac{A I_{CW}}{l^2 d} \frac{\lambda}{hc} (1 - R) \tau \qquad (37)$$

where I_{CW} is the laser intensity, A is the illuminated area, l is the sample lateral dimension, d is the sample thickness, λ is the CW laser wavelength, $1 - R$ is the light loss from reflections and τ is the paraexciton lifetime. We find that in the collinear illumination geometry ($A = \pi/4 \times 0.2^2$ cm^2) for sample 1 ($d = 2.2$ mm)

$$n \cong 2 \times 10^{18} \tau \ [\text{cm}^{-3}] \text{ per W / cm}^2 \qquad (38)$$

The above equations assume that the excitons are mobile enough to evenly distribute themselves in the crystal volume within their lifetime irrespective of their initial distribution. We will see that this is not always the case, but for weak absorption (small values of α) near the red absorption edge and at the orthoexciton quadrupole line, the assumption is valid. We offer experimental evidence to support this assumption in Fig. 58. We delay the interpretation

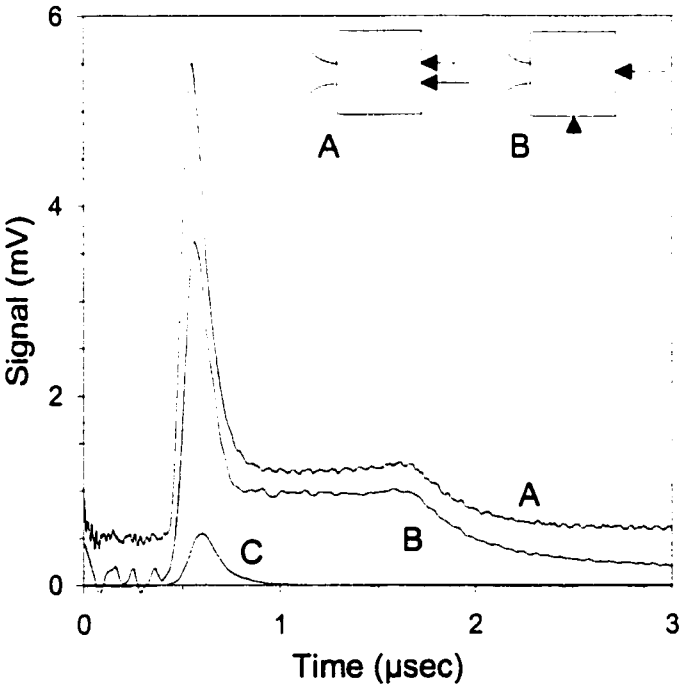

Fig. 58 Excitonic flux from pulse and CW illumination (traces A and B) in the illustrated geometry for a 2.2 mm thick Cu_2O crystal at $T = 2$K. Trace C is from the pulse laser only. The pulsed laser ($\lambda = 532$ nm) intensity was $2I_o$, the CW laser ($\lambda = 605.5$ nm) power was ~ 45 mW.

of the packet amplification and subsequent quasi DC signal (from now on dubbed the "plateau") seen in the figure to the following sections. However we remark on the similarity of the pulse and CW illumination results obtained in different illumination configurations (ignore the vertical shift, it is explained below). The similarity of the experimental results indicates that the excitons deposited by the CW laser during the packet transit are far fewer in number than the steady state population. The steady state population generated irrespective of the CW laser orientation is the cause of the spectacular amplification of the packet observed in Fig. 58.

The collinear CW and pulse lasers illuminated the sample through a 2 mm diameter aperture on the face directly opposite the electrodes as seen in inset A of Fig. 58. The orthogonal CW laser illuminated a 1 mm diameter aperture on the side of the sample as depicted in inset B. The intensity of the orthogonal CW laser was ~ 4 times that of the collinear CW laser (which was ~ 1.5 W/cm^2), but the laser light power entering the sample was approximately 45 mW in both cases. The CW wavelength was chosen to give the maximum signal, this occurred at λ = 605.5 nm which is near the red absorption edge of Cu_2O as described in Sec. 1.3. Similar results are obtained for CW illumination at λ = 609.7 nm on the orthoexciton quadrupole transition.

The trace obtained under collinear excitation is vertically shifted by ~ 0.5 mV whereas in the orthogonal case the shift is barely visible (~ 30 μV). We believe this DC signal is nearly entirely due to light from the CW laser creating excitons directly in the depletion width nearest the Au electrode. These excitons do not need to diffuse any distance to be gathered as an external current and hence produce an extraordinarily large signal for a small amount of light input. The orthogonal CW beam produces a small DC signal from internally and externally scattered light striking the electrode.

To further support this argument we have modulated the CW beam with a light chopper and have found that the DC signal almost exactly follows the expected modified square wave profile (the chopper is obstructing a circular aperture therefore the square wave has "rounded corners"). We therefore conclude that the diffusive exciton flux is very weak due to the lack of a preferential drift velocity, and that the presence of a DC signal does not significantly amplify the signal produced by the exciton packet. In fact

we have some experimental evidence that a DC signal in some cases will actually decrease the efficiency of the exciton detector.

3.4.1 Packet Amplification

We now explore the behaviour of the packet amplification as function of both pulse and CW laser intensities in the collinear geometry; the important trailing plateau will be dealt with in the next section. The time resolved exciton flux data (with the DC background subtracted) displayed in Figs. 59a to 59e was collected over 2 orders of magnitude in pulse laser intensity and 3 orders of magnitude in CW laser intensity.

a)

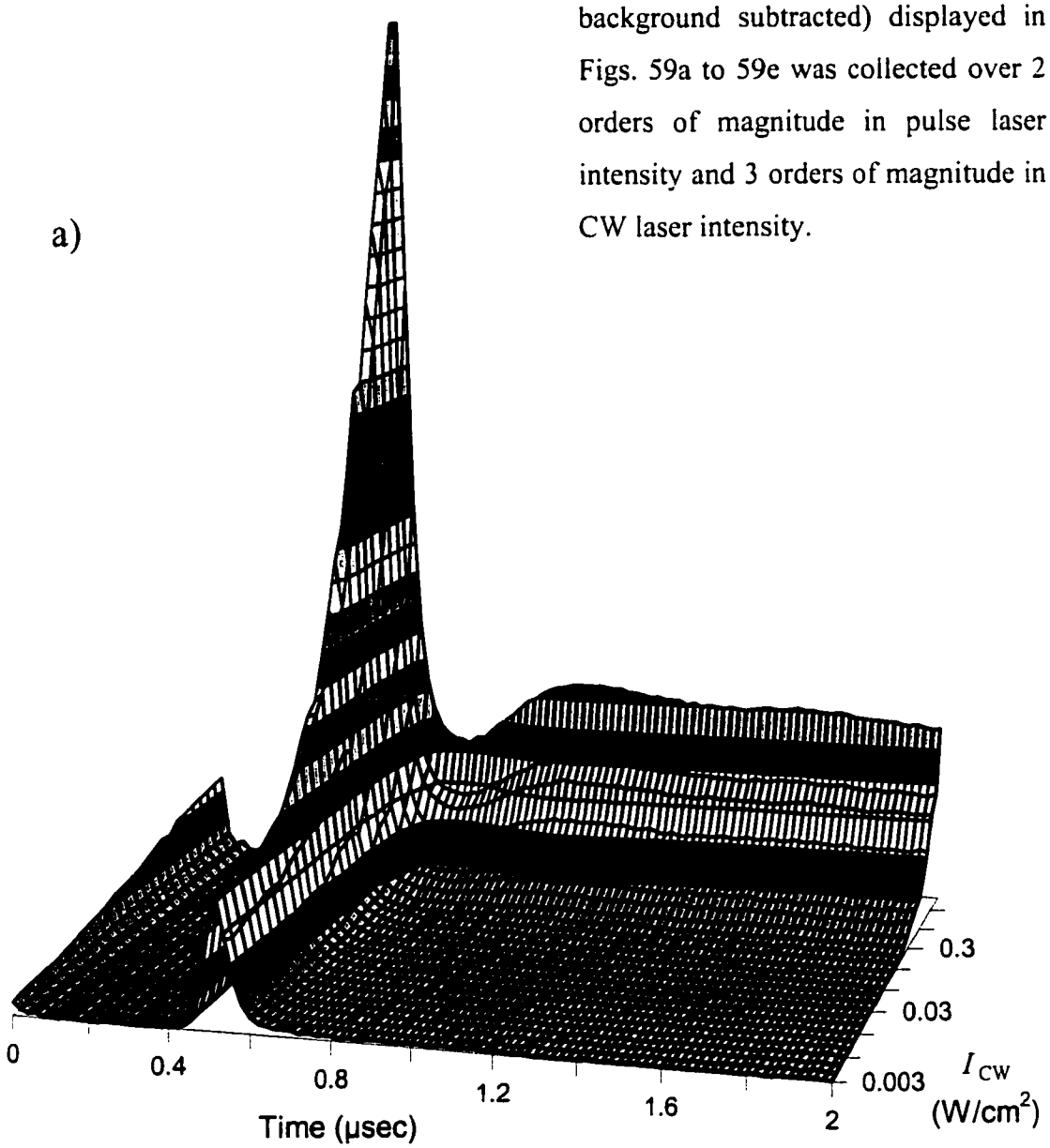

Fig. 59 a) b) c) d) e) (figures b) to e) are on the following pages) Excitonic flux for collinear pulse and CW illumination of a 2.2 mm Cu_2O crystal at T = 2K. The intensity of the pulse laser (λ = 532 nm) is constant for each figure with values of $20I_o$, $6I_o$, $2I_o$, $0.6I_o$, and $0.2I_o$ respectively. In all the figures the wavelength of the CW laser is 605.5 nm and the maximum vertical scale is 30mV. The contour levels for each figure are 1 mV, 1 mV, 0.5 mV, 0.25 mV and 0.1 mV respectively.

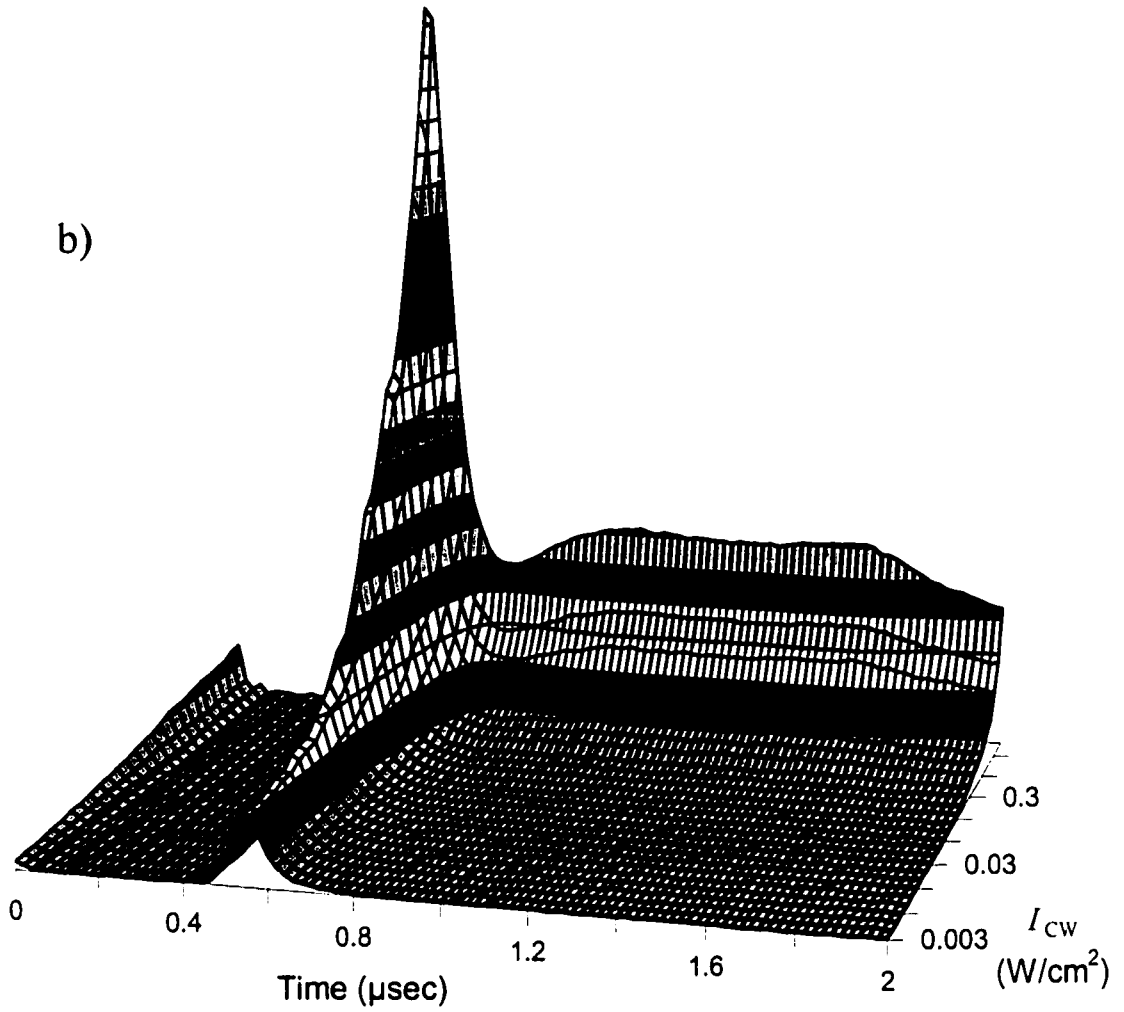
b)
0
0.4
0.8
1.2
1.6
2
Time (μsec)
0.3
0.03
0.003
I_{CW}
(W/cm^2)

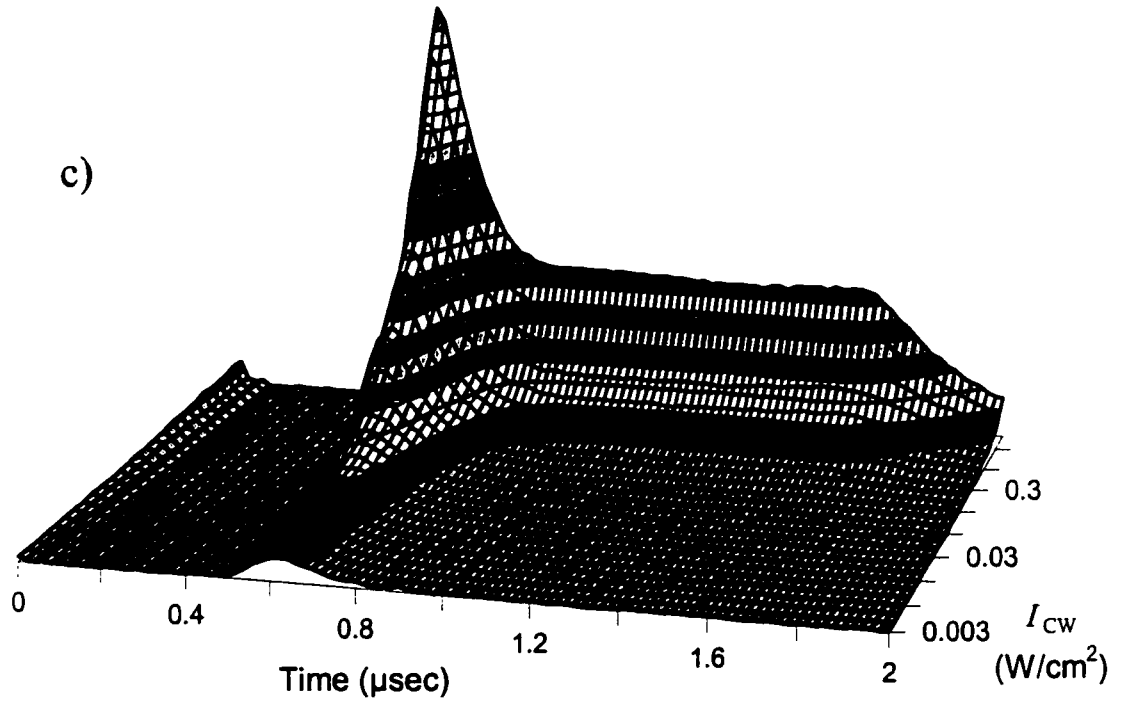
c)
0
0.4
0.8
1.2
1.6
2
Time (μsec)
0.3
0.03
0.003
I_{CW}
(W/cm^2)

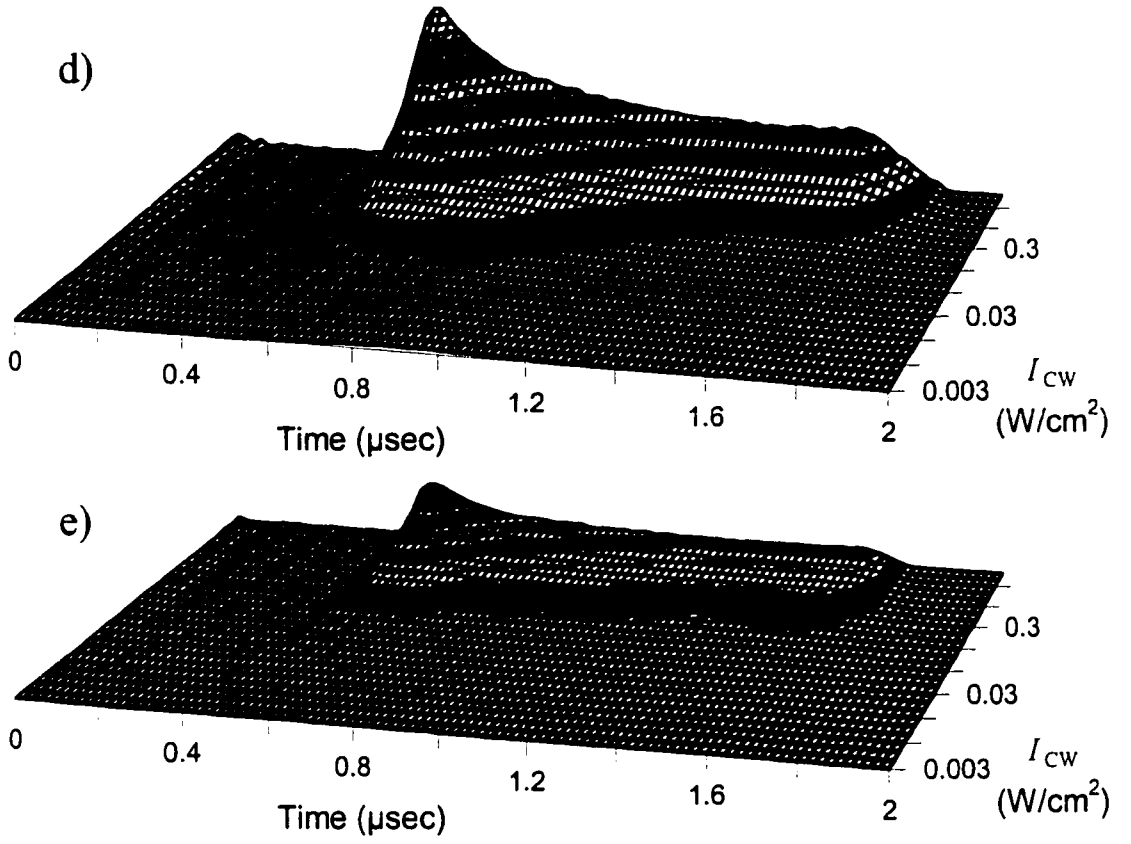

As can be seen in the figures for very low CW laser intensity the packet, or diffusive cloud, travels nearly undisturbed by the weak exciton background permeating the crystal. As the CW laser intensity is increased the signal arriving for a velocity greater than about $0.8v_s$ (i.e. corresponding to the approximate arrival time of the packet) in all cases is amplified. However it is apparent that the CW threshold intensity for a noticeable change in the packet amplitude decreases as the pulse laser intensity increases.

For the three upper pulse laser intensities, where a packet is formed by the pulse laser only, the addition of the CW laser increases the packet amplitude without greatly affecting the packet width or velocity. However for the pulse intensities far below the upper critical intensity (i.e. $0.6I_o$ and $0.2I_o$) the wide diffusive cloud is transformed into a fast moving compact packet.

We attribute the amplification of the already formed packet and formation of a packet from a diffusive cloud to the stimulated emission of excitons into the packet from the background of excitons. This is the same effect seen in Sec. 3.3 and described theoretically in Sec. 1.7. The formation of the packet from a diffusive cloud is really an

extension of the normally short condensate "lifetime" at these low pulse intensities. With no background of excitons to feed the weak condensate as it propagates, the condensate evaporates into the volume (see Sec. 3.1.3). But with the stimulated emission of excitons into the condensate it can survive the transit and register a ballistic signal at the electrode. One could view the apparent gain as a reduction of the losses.

To quantitatively measure the amplification, Fig. 60 was constructed using the data shown in Figs. 59a - e and other time resolved traces not shown here. The left pane of the figure displays the packet amplitude as a function of CW laser intensity for the five pulse laser intensities used in the experiment. In the right pane a fraction of the same data is plotted as a function of pulse laser intensity along with a reference series obtained under pulse illumination only.

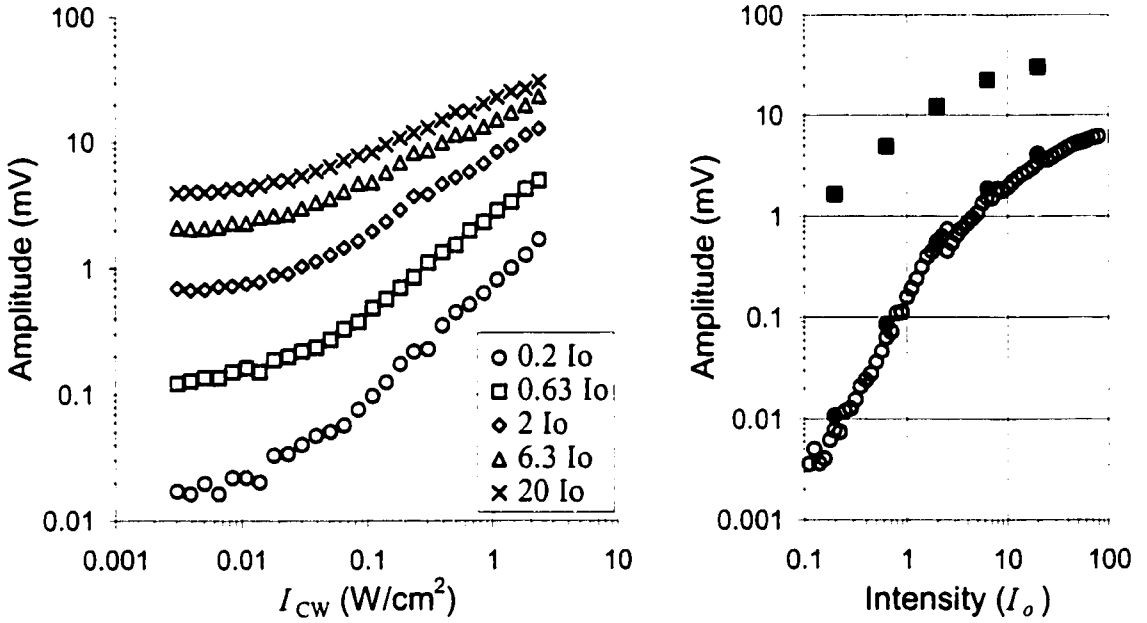

Fig. 60 Left: Amplitude of packet as a function of CW laser (λ = 605.5 nm) intensity in the collinear pulse and CW illumination geometry for a 2.2 mm crystal at T = 2K. The λ = 532 nm pulse laser intensity is indicated in the legend. Right: Amplitude of packet as a function of pulse laser intensity under identical conditions. Open and filled circles: pulse laser only, from different experimental runs. Filled squares: pulse and CW laser (I_{CW} ~2.5 W/cm^2) illumination.

The resemblance of the left pane of Fig. 60 to Fig. 54 in Sec. 3.3.1 is uncanny. If one considers the smaller dynamic range for the background exciton level in Fig. 60, all the curves have the same qualitative behaviour. The gain has three regions: at low background levels the gain is nearly flat, then it increases rapidly, and for the upper curves we seem to have reached the saturation level. The right pane shows the saturation

of the packet created by pulse illumination alone as a function of pulse intensity, and the even stronger saturation of the packet propagating in the dense exciton background. The change in the gain as a function of pulse intensity reveals the greater effect the background excitons have on the partly diffusive transport as alluded to above.

If we compare the amplified signal obtained under identical primary (Nd:YAG) pulse laser conditions for the orthogonal delayed pulse (Sec. 3.3.1) and CW laser illumination at the same wavelength (~ 605.5 nm) we can calculate the paraexciton lifetime. We will assume that the density of excitons in the central volume of the sample that causes the same amplification is equal in both the double pulse and pulse + CW experiments. Using Eqs. (19) and (37) we obtain

$$n = \frac{A\, I_{CW}}{l^2 d}\frac{\lambda}{hc}(1-R)\,\tau = \alpha e^{-\alpha z}\frac{\lambda}{hc}(1-R)\,\delta t\, I_p \qquad (39)$$

For the $0.2I_o$ main pulse laser case, a packet with a 1.2 mV amplitude is obtained from a $0.3I_o$ orthogonal pulse or a 1.7 W/cm^2 CW laser. Substituting the relevant parameters into Eq. (39) we obtain a paraexciton lifetime of 0.3 msec. The same calculation performed for the $20I_o$ main pulse laser nets a lifetime of 0.1 msec. Clearly some of the estimates of the paraexciton lifetime in the literature are undervalued, but with good reason as explained in Sec. 1.4 and [11].

The very large amplifications seen here and in Secs. 3.2 and 3.3 beg the question: Are there enough excitons to account for the increase in signal? If we only considered the background excitons created by the CW laser the answer is definitely no. However as mentioned before we know that a large fraction of the primary pulse generated excitons are not in the packet when it reaches the detector but distributed in the crystal volume as a background of excitons. We now estimate the fraction of excitons in the ballistic packet and as a corollary calibrate our exciton detector.

We will make two assumptions which are supported by experimental evidence: Firstly that the density in the packet is the critical density for BEC when we illuminate the sample with a pulse laser of intensity $I_c \sim 4I_o$, and secondly that the packet is an ellipsoid or spheroid with an average radius of ~ 250 μm (see Secs. 3.1.3 and 3.1.5). The number of excitons in the packet is given by

$$N = n_c \frac{4\pi}{3} r^3 \cong 8 \times 10^{16} \cdot 4 \cdot 0.025^3 \cong 5 \times 10^{12} \qquad (40)$$

We know that the number of photons entering the sample in the $4I_o$ pulse is 1.7×10^{14}, therefore the fraction of excitons in the packet is 1.5%. The resulting flux of excitons which gives 1 mV of signal (the amplitude of the packet created by the λ = 532 nm laser at $4I_o$) is the number of excitons in the packet divided by the temporal width of the packet

$$\frac{N}{\Delta t} \cong \frac{5 \times 10^{12}}{0.1\,\mu\text{sec}} \cong 5 \times 10^{19} \text{ exc / sec} \Leftrightarrow 1 \text{ mV} \qquad (41)$$

As an aside we can also calculate the detector efficiency for excitons arriving from the interior of the crystal (as opposed to excitons deposited in the depletion width). A 1 mV signal for 1 sec (1 mV sec) across 50 Ω gives 20 μA s = 20 μC. Since one exciton produces two free carriers: 1 exc = 3.2×10^{-19} C, we have 1 mV sec = 6×10^{13} exc. Therefore if a flux of 5×10^{19} exc/sec gives 1 mV the detector efficiency is ~ 10^{-6}. The much smaller efficiency as opposed to the value quoted in Sec. 2.2.2 is not surprising since the majority of the signal in the direct illumination case would come from excitons created in the most efficient area likely on the sample surface between the Cu and Au electrodes.

Concluding, the small fraction of excitons in the packet at the upper critical intensity is consistent with the evaporating comet model and the large gains witnessed for propagation through a cold exciton background.

3.4.2 Filament

We now turn our attention to the plateau after the packet. We note that such a plateau was also observed for orthogonal pulse illumination as noted in Sec. 3.3.1 although it was very weak. The abrupt collapse of the plateau for low pulse laser intensities at ~ 1.7 μsec in Sec. 3.4.1 provides us with a clue to its origin. This arrival time coincides with exactly 3 packet transits across the sample. To prove this without a doubt we have measured the plateau in three different thickness samples as seen in Fig. 61. The arrival time of the main packet is plotted in the inset, the slope of the straight line fit through the points is the velocity of the packet ~ $0.88v_s$. The "collapse" time of the plateau is also plotted in the inset with a slope exactly 1/3 that of the packet velocity. Either the excitons in the plateau are moving with a drift velocity of exactly 1/3 the

packet velocity following the packet while the packet completes one transit, or the plateau excitons are moving at some unknown but substantial drift velocity, again behind the packet, while it completes three transits across the sample before the plateau excitons abruptly stop. We favor the latter argument since we cannot find any reason why the excitons would travel over a large distance at a constant velocity of 1.32×10^5 cm/s. We note that the TA phonon mode which interacts very weakly with paraexcitons has a velocity of 1.2×10^5 cm/s. We dismiss the TA phonons as the source for the drift since the 10% difference in velocity would be distinguishable.

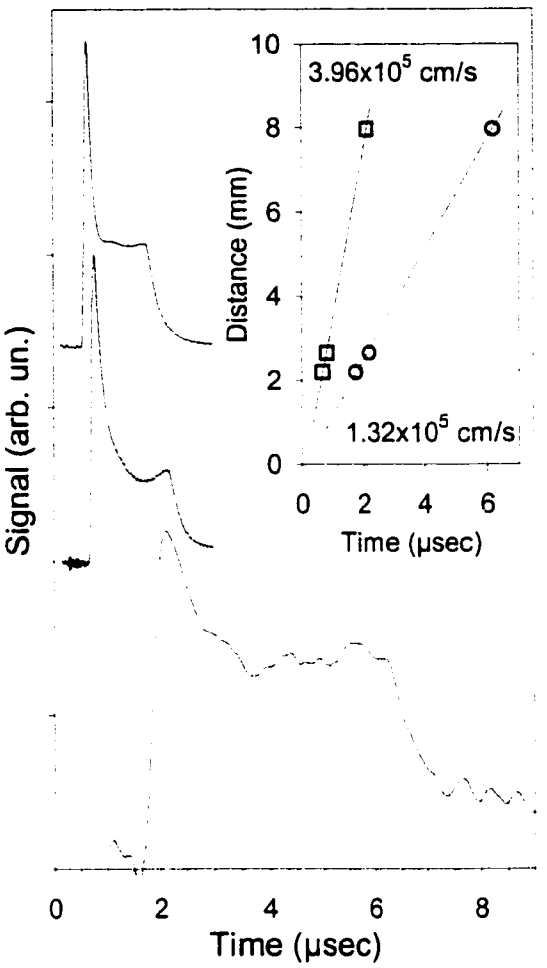

Fig. 61 Excitonic flux for collinear pulse and CW illumination at T = 2K as a function of sample thickness. The traces (from bottom) were obtained in sample 4 (d = 8 mm), sample 2 (d = 2.65 mm) and sample 1 (d = 2.2 mm). The intensity of the pulse laser (λ = 532 nm) was ~ $4I_o$ and the intensity of the CW laser (λ = 605.5 nm) was ~ 4 W/cm^2. The traces have been vertically displaced for clarity. Inset: The sample thickness is plotted versus the packet arrival time (squares) and the falling edge of the plateau (circles). The slope of a linear fit is indicated.

We postulate that the plateau is a BEC filament of excitons linking two faces of the crystal, one of which is the detector face the other the pulse laser illuminated face (see Fig. 62). Excitons in the filament are propagating ballistically at a velocity near $v_o \sim v_s / 2$ on an axis perpendicular to these faces in both directions and are reflected by the crystal faces. The arrival of excitons of the same velocity from all points between the detector and illuminated faces produces the nearly constant signal seen in the figures. The filament is fed by the stimulated emission of excitons from the background exciton sea permeating the crystal which in turn is stocked by excess pulse created excitons and CW laser created excitons.

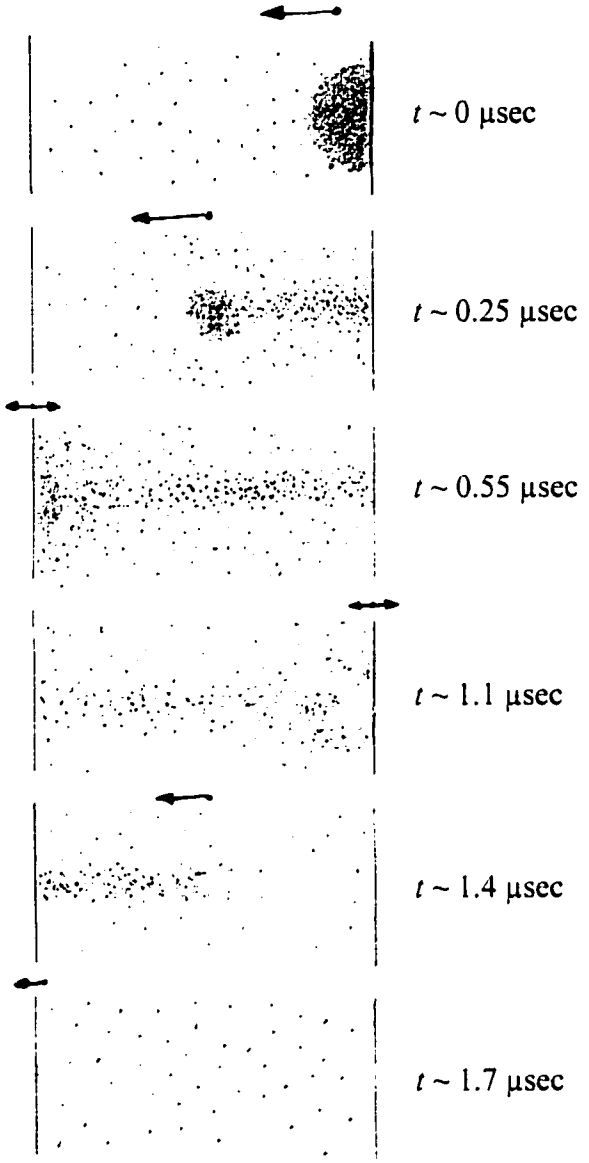

Fig. 62 Sketch of condensate and filament at various times after pulse illumination in a 2.2 mm thick Cu_2O crystal at T = 2K. The sample is illuminated from the right by a pulse and CW laser, the electrodes are on the left face. The dark cloud is the condensate, the thin trail across the sample is the filament and the background exciton population is represented by the random specks. The arrow above each frame indicates the condensate propagation direction.

It seems the filament is formed by the passage of a condensate through the sample, perhaps it is the "tail" in the comet model, greatly amplified just as the "nucleus" is. As mentioned above the lifetime of the filament is linked to the presence of a condensate in the sample in the case where the condensate must steal particles from the background to regenerate its losses and remain a condensate while propagating. This occurs for pulse laser intensities of less than $4I_o$ as seen in Figs. 59c - e where the plateau collapses after three packets transits. We postulate that in these cases the condensate effectively depletes the background during the transits and is destroyed on the third reflection. The filament is either "reeled in" on the third transit as depicted in Fig. 62, or it cannot sustain itself alone and simply disintegrates after the destruction of the condensate. For higher pulse intensities ($I > 4I_o$) we always observe a long lived filament, even for low CW laser intensities. We believe that in these cases the pulse laser always supplies enough excitons to replenish the "stolen" background excitons (stimulated into the packet giving the observed packet amplification) in addition to bolstering the background population itself.

The small bump arriving just before plateau collapse in Fig. 61 (the same phenomena may also be seen in Figs. 59a - e) may be the remnant of the condensate arriving for a second time at the detector face ($t \sim 1.7$ μsec). In all the results we have gathered we have never seen a packet arriving after three transits much larger (in amplitude) than those shown in the figures above indicating that the condensate mostly is dissolved after three transits. Packets arriving at 5, 7, etc. transits are very weak and will be shown in Sec. 3.5. Perhaps the condensate cannot completely regenerate itself from the loss of coherence (excitons scattered out of the condensate and into the background) from a reflection at a likely imperfect boundary. Or possibly, once the filament is formed it severely depletes the condensate traveling through it. If a larger CW laser input, producing a denser exciton background, was available perhaps the packet could recover from the reflections losses and a collapse at 5, 7, 9, etc. transits would be observable.

The exact origin of the fairly wide second peak arriving at ~ 1 μsec after the laser pulse in Figs. 59a and b is unknown. It is only present under intense pulse laser excitation. The arrival time does somewhat coincide with a trajectory at 45 degrees from the incident face reflecting off a side face back towards the detector (i.e. for sample 1 with dimensions 3.8 x 3.8 x 2.2 mm $d \sim 2(1.1^2 + 1.9^2)^{1/2} = 4.4$ mm which gives $v/v_s = d / (t\ v_s) \sim 0.98$). An alternative explanation is an interaction between the main packet and the filament causing a local fluctuation in the density of the filament behind the main packet. However the most likely explanation is that the peak is caused by the arrival of a secondary soliton (as observed in Sec. 3.3.2) propagating at just above the critical velocity v_o ($\sim v_s/2$).

We have plotted the plateau amplitude (an average of the signal from 1.2 μsec to 1.6 μsec) as a function of pulse laser and CW laser intensities in Fig. 63. There seems to be a threshold for amplification at low intensity ($I_{CW} \sim 0.03$ W/cm^2 and $I \sim 0.6I_o$) just like in the packet amplification case. The gain (in packet amplitude) as a function of CW laser intensity is approximately linear for large pulse input, and sub-linear for the two smaller inputs ($0.2I_o$ and $0.6I_o$). The magnitude of the signal reveals the amount of exciton flux produced by the filament if we assume the detector calibration in Sec. 3.4.1 is accurate (1 mV s = 5×10^{19} exc). In turn if the plateau signal is mostly from the CW

exciton contribution the exciton flux from the plateau leads to another independent approximation of the paraexciton lifetime using

$$Flux = \frac{N_f}{\Delta t} = \frac{n_f A d}{\Delta t} = \frac{2 \times 10^{18} \tau A d}{\Delta t} \tag{42}$$

where N_f is the number of excitons in the filament per W/cm^2 of CW laser illumination, n_f is the filament density, A is the filament cross section (equal to the detector and beam areas) and d is the filament length (equal to the sample thickness). According to the proposed filament model the temporal width to be substituted into Eq. (42) is the transit time of the excitons across the sample at half the speed of sound ($\sim v_o$). This gives all the excitons in the filament a chance to strike the detector once. In the low intensity pulse

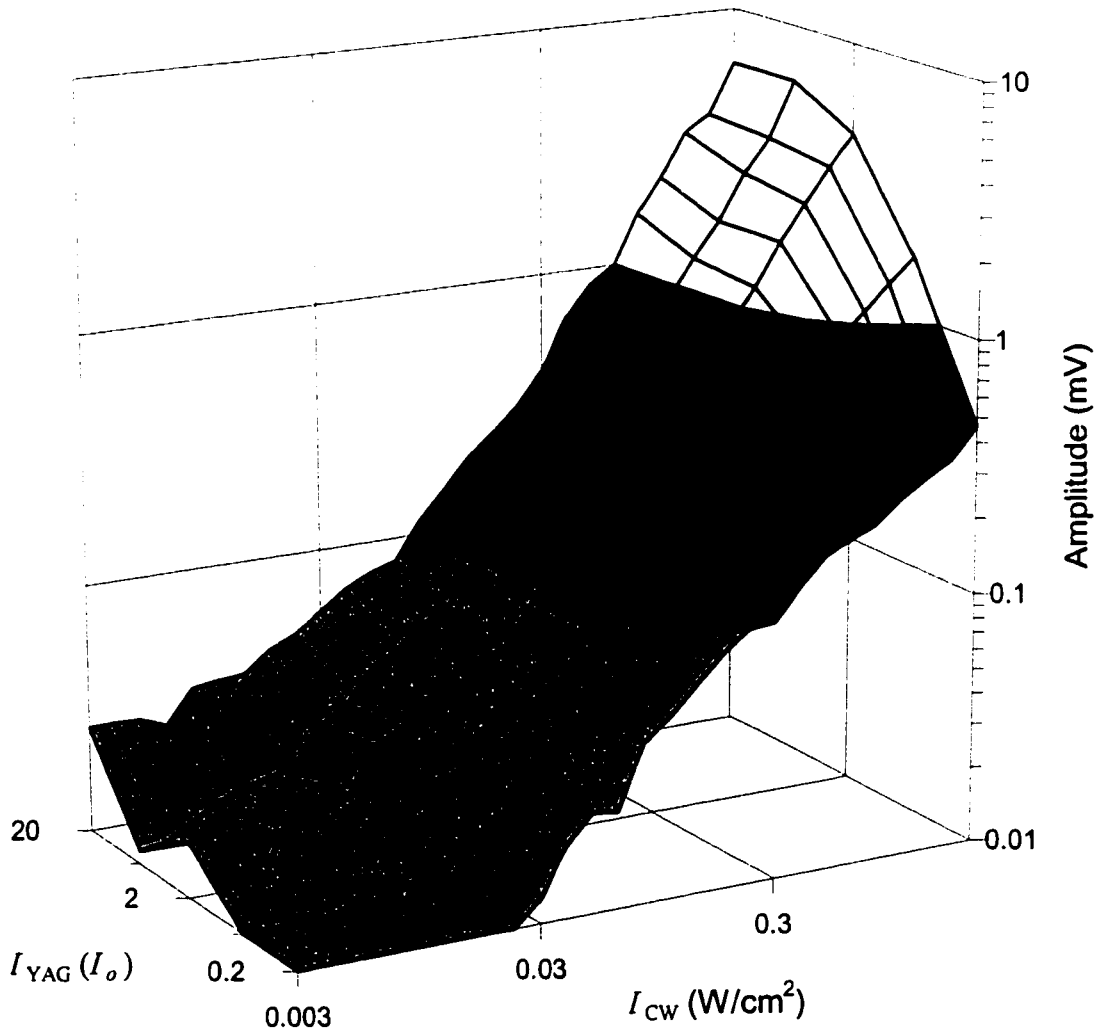

Fig. 63 Amplitude of plateau as function of pulse (λ = 532 nm) and CW (λ = 605.5 nm) laser intensities for a 2.2 mm thick crystal at T = 2K using the collinear illumination geometry.

laser ($0.2I_o$) and high intensity CW laser (1 W/cm^2) instance we have measured a plateau signal of ~ 0.3 mV. According to the calibration this gives a flux of 1.5×10^{19} exc/s which leads to a paraexciton lifetime of ~ 1 msec. This calculation agrees with the result derived from Eq. (39) which was based on the comparison of data from the delayed orthogonal pulse and CW laser experiments.

We note that the magnitude of the plateau flux is not very sensitive to the pulse laser intensity indicating that the plateau behaviour is mostly controlled by the number of CW background excitons present. However there still is a very strong saturation of the plateau amplitude as a function of pulse laser intensity at high CW laser intensity. This was also apparent in the packet amplification (see. Fig. 60 right pane), so what effect do the extra pulse excitons have at these high intensities? The answer to this question lies in Fig. 64: here we see that the plateau lifetime increases substantially for large pulse laser input. With an even more intense pulse laser and λ = 609.7 CW laser illumination (n = 1

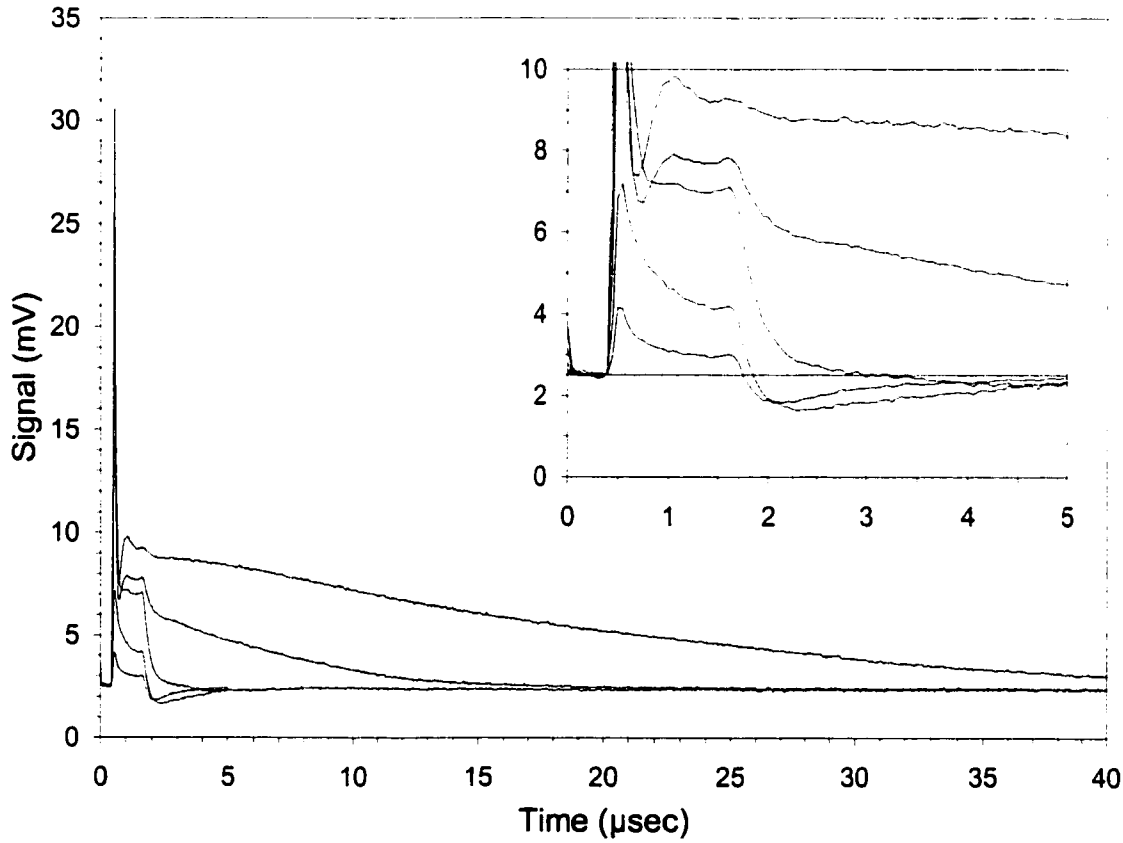

Fig. 64 Excitonic flux for collinear pulse (λ = 532 nm) and CW (λ = 605.5 nm) illumination of a 2.2 mm Cu_2O crystal at T = 2K. The intensity of the pulse laser was (from top): $20I_o$, $6I_o$, $2I_o$, $0.6I_o$, and $0.2I_o$. The CW laser intensity was ~ 3 W/cm^2. The inset is a close up of the traces at early times.

orthoexciton) a plateau lasting up to ~ 100 μsec has been observed.

The inset shows a close-up of the time resolved signal in the first few microseconds: the signal for the two lowest pulse intensities drops below the DC level caused by direct electrode illumination. We cannot currently explain this observation but we offer two possibilities: The detector could be overreacting to the large, quick drop of the plateau signal or the drop is due to light being *absorbed* by the collapsing filament and/or packet.

We believe that the packet and filament interaction is a symbiotic relationship. Thus attributing a particular effect exclusively to the packet or filament is very difficult if not impossible. In addition we cannot make a quantitative analysis of the filament behaviour with only the time resolved flux data available. For example, we cannot establish the cross section of the filament and the obviously related density of excitons in the filament due to our "one pixel" detector. From the estimated flux produced by the filament (see Eq. (42)) we find an exciton density of 3×10^{15} cm^{-3} for a 1 mV plateau amplitude. However this assumes the filament is as large as the detector and laser beam cross section. If the filament has a cross section on the order of the packet cross section (~ 400 μm), the density is near the critical density for BEC. The large range of values reflect the lack of spatially resolved data.

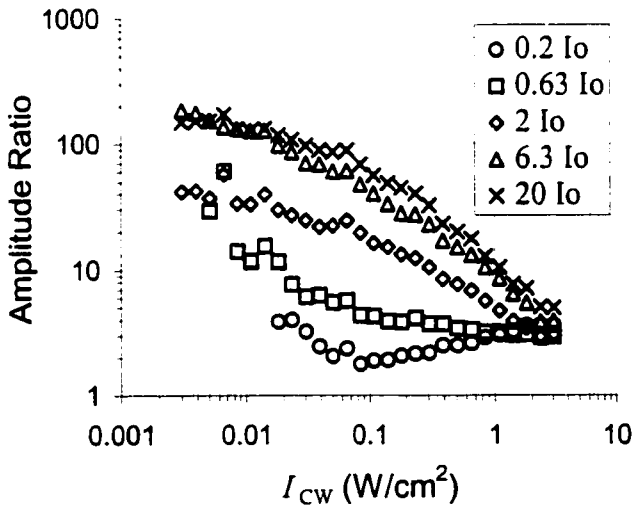

Fig. 65 Ratio of packet amplitude over plateau amplitude as a function of CW laser (λ = 605.5 nm) intensity in the collinear pulse and CW illumination geometry for a 2.2 mm crystal at T = 2K. The λ = 532 nm pulse laser intensity is indicated in the legend.

In support of the above assertion of a symbiotic relationship between the filament and packet, we present Fig. 65. The ratio of the packet amplitude and plateau amplitude is plotted as a function of CW laser intensity for five pulse laser intensities. The ratios seems to converge to common point above 2 W/cm^2. The mechanism behind this behaviour is beyond the scope of this work and a different

experimental approach may be necessary to fully resolve the complex interaction taking place in the Cu_2O crystal.

3.4.3 CW Wavelength Dependence

We have measured the dependence of the packet amplification and plateau amplitude as a function of CW laser wavelength. As a an additional benefit we also were able to simultaneously determine the absorption coefficient near the red absorption edge from the DC offset of the time resolved data. This type of measurement is very difficult to perform without a very thick sample due to the very weak absorption in this region.

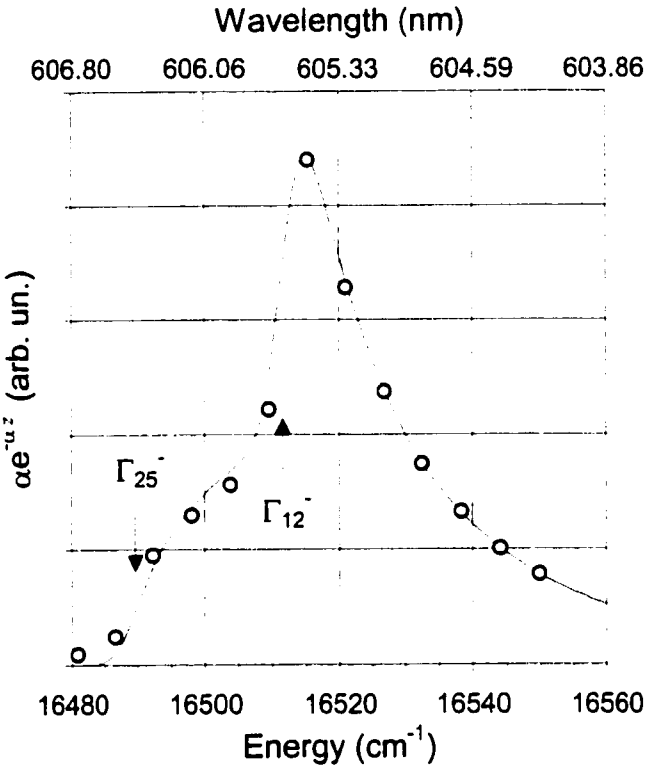

Fig. 66 DC signal amplitude (circles) for CW illumination of a 2.2 mm crystal at T = 2K as a function of CW laser energy. The solid line is a fit described in the text. The arrows indicate the energy of relevant phonons.

As mentioned earlier the majority of the DC signal is attributed to excitons being created in the most sensitive detector volume very close to the sample surface. Thus the local exciton density is proportional to Eq. (19) ($n \propto \alpha e^{-\alpha z}$) as opposed to Eq. (37) ($n \propto \lambda\tau$) since the effective exciton lifetime in the aforementioned volume may be an order of magnitude or more lower due to surface recombination and a much higher relative detector efficiency. The DC signal as a function of CW laser wavelength is plotted along with a fit proportional to the local exciton density in Fig. 66. The value of α used to fit the data was calculated from

$$\alpha = k_1\sqrt{(E-(X_o+\Gamma_{25}^-)} + k_2\sqrt{(E-(X_o+\Gamma_{12}^-)} \qquad (43)$$

where $k_1 = 0.16$, $k_2 = 3$, $\Gamma_{25}^- = 88$ cm^{-1} and $\Gamma_{12}^- = 110$ cm^{-1} and $X_o = 16401.5$ cm^{-1}. Note that the photon to phonon coupling coefficients k_1, k_2 and an overall scaling of n(cm^{-3}) to

S(mV) are the only fitting parameters since the phonon and exciton energies were taken from the literature [6, 7]. The fitted line was also convoluted with the laser line (spectral width ~ 0.18 nm). The absorption coefficient as a function of energy near the red edge calculated from the fit was plotted in Fig. 5; the results are in agreement with published data [19, 20] as are the relative strengths of k_1 and k_2 [11].

The effect of the CW laser wavelength on the packet amplification is dramatic as witnessed by comparing the top three traces in Fig. 67. Not shown in the figure is the limiting case, obtained by using an Ar^+ gas laser (λ = 514 nm, $\alpha > 3000$ cm^{-1}) as the CW laser source, where the gain is almost imperceptible [37]. We draw the conclusion that the additional phonons, created by the excess photon energy, are detrimental to the stimulated amplification mechanism. In other words the CW created excitons in this case are not "cold" (i.e. near equilibrium with the lattice phonon population) and do not scatter preferentially into the condensed state. In addition the mobility of the "hot" excitons may not be large enough to create an even distribution throughout the crystal. The mobility of excitons was shown to vary with $T^{-5/2}$. [4, 5] and as mentioned in Sec. 1.4 the effective temperature of excitons increases for higher densities and larger excess photon energy. The exact dynamics of the exciton distribution as a function of sample temperature, input wavelength and laser intensity is a daunting problem

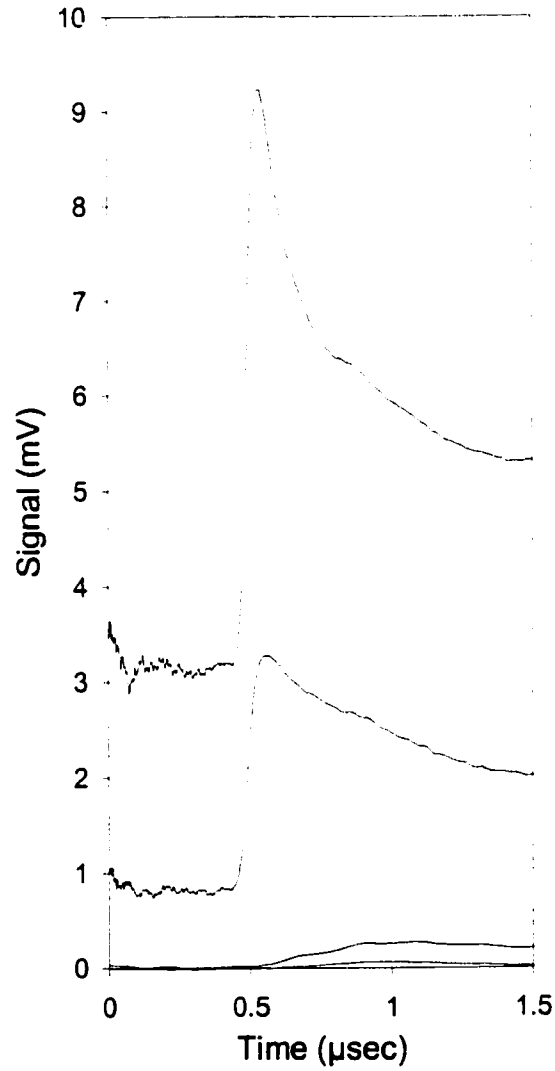

Fig. 67 Excitonic flux for collinear pulse and CW illumination of a 2.2 mm Cu_2O crystal at T = 2K. The intensity of the pulse laser (λ = 532 nm) was $0.6I_o$, the CW laser was ~ 4 W/cm^2. The CW laser wavelength was (from top): 605.5 nm, 604.2 nm and 585 nm; the bottom trace is from the pulse laser alone.

that has not be solved yet. However if the excitons are not evenly distributed the overlap between the traveling exciton cloud and a significant CW exciton background would be diminished to only the early times when the cloud is close to the illuminated face as opposed to the transit time across the entire sample.

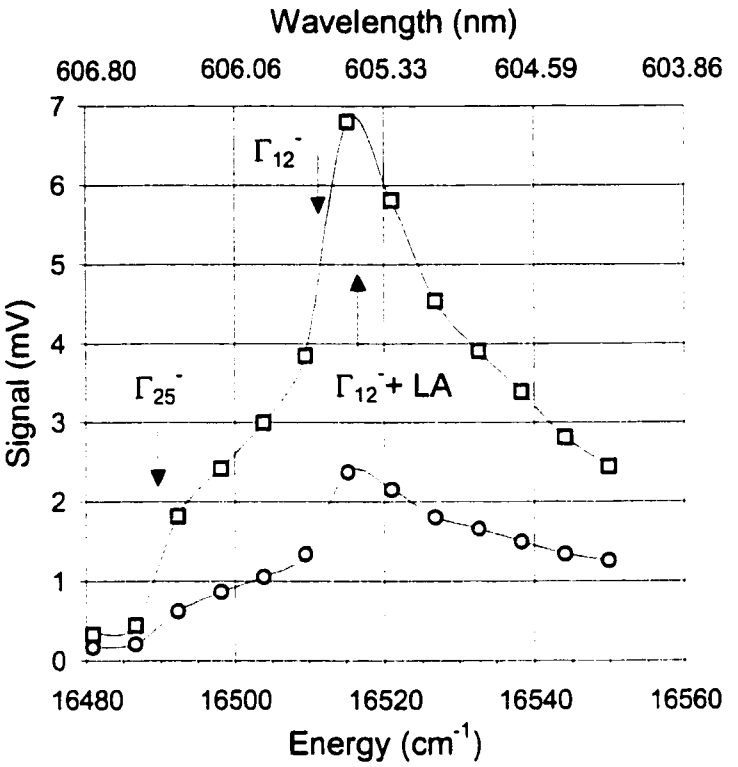

Fig. 68 Packet (squares) and plateau (circles) amplitude for collinear pulse and CW illumination of a 2.2 mm crystal at T = 2K as a function of CW laser energy. The illumination conditions are identical to those in Fig. 67. The solid lines are cubic spline interpolations to help guide the eye. The arrows indicate the energy of relevant phonons.

For the two reasons mentioned above the variation of the packet and plateau amplitude near the red absorption edge shown in Fig. 68 is complicated. At photon energies less than the $X_o + \Gamma_{12}^-$ transition (~ 16510 cm^{-1}) the signals follow the same trend the DC signal displayed in Fig. 66 as a function of CW laser wavelength. In this region the photons are very weakly absorbed (see Fig. 5) and the average exciton population declines as a result (as if the laser intensity was attenuated). In light of the approximately linear dependence of the packet and plateau amplitudes in the given experimental conditions (see Figs. 60 and 63) the observed correlation between the DC signal and packet/plateau amplitude is expected in this region.

The rapid rise of the signal amplification near the $X_o + \Gamma_{12}^-$ transition corresponds to the increase of the absorption coefficient and subsequent increase in average exciton density in the Cu_2O crystal. Due to the accuracy of the wavelength calibration and laser line width (Sec. 2.1.3) we cannot exclusively identify the peak of the amplification (~ 605.5 nm = 16515 cm^{-1}) with the $X_o + \Gamma_{12}^-$ (~ 16511.5 cm^{-1}) transition or the $X_o + \Gamma_{12}^- +$

LA phonon (~ 16516.5 cm^{-1}) transition. The peak of amplification for the orthogonal pulse laser, which has a considerably narrower laser line width, was found to be at ~ 605.6 nm (= 16512 cm^{-1}), although an accurate scan of the region was not performed. However, beyond these photon energies the trend is clear, the signal amplitude decreases due to increased phonon production and CW exciton spatial inhomogeneity. We note that both the plateau and the amplitude curves in Fig. 68 decrease slower than the DC signal curve of Fig. 66. This reinforces the distinction between the simple exciton absorption effect causing the DC signal variation and the more complex stimulated emission effect postulated to be the source of the large signal amplifications. From Figs. 68 and 67 it also seems that the additional phonon population has a greater effect on the packet amplification than on filament formation. This may be understood be the fact that the packet redistributes the excitons into the sample volume and the filament "sees" a more homogeneous distribution.

3.4.4 Temperature Dependence

In order to confirm our interpretation of the aforementioned amplification we have measured the time resolved exciton flux for pulse and CW laser illumination at different sample temperatures. A small fraction of the results are shown in Fig. 69 where the data obtained at constant pulse and CW laser intensity for three temperatures, 2K, 4K and 6K is plotted. The inset shows the pulse only data from the same experimental run. The experimental traces demonstrate that a small change in sample temperature causes a significant change in the packet and plateau measured by the detector. The results shown here have put to rest the suspicion that the large packet and plateau amplifications we have measured were due to some kind of detector malfunction or artifact. It is extremely unlikely that any kind of change occurs in the exciton detector between 2K and 6K. However the measured signal does change substantially in this temperature range (the packet nearly disappears and the plateau is reduced by a factor of 5 for a change in temperature of 4K) as expected from Bose-Einstein theory.

By comparing the results in Fig. 69 we notice that the packet amplitude seems to be more susceptible to a change in temperature than the plateau amplitude, reinforcing the argument in the previous section that the spatial distribution of CW excitons is affected by the temperature.

Several experimental factors made measuring the signal precisely as a function of temperature difficult. The lower cooling power of the normal liquid and gaseous He shortened the length of time the sample could be illuminated by an intense CW laser beam without heating the sample. The bubbles in the liquid He changed the effective laser intensity reaching the sample, and having the temperature sensor connected for the duration of the experiment increased the noise recorded along with data. Nevertheless the signal was measured from 2K to 6K for five pulse laser intensities. The normalized plateau amplitude is plotted in Fig. 70 along with a theoretical calculation of the condensate fraction. The plateau amplitude was normalized to compensate for fluctuations in the CW laser intensity. The relative scale of the laser intensity and exciton density is based upon the fact that the packet density is approximately equal to n_c (at T = 2K) for a pulse laser intensity of $4I_o$. Unfortunately an indisputable calibration of the scale is impossible at this time since the density in the filament is unknown. The calibration of the temperature scales however is very reliable.

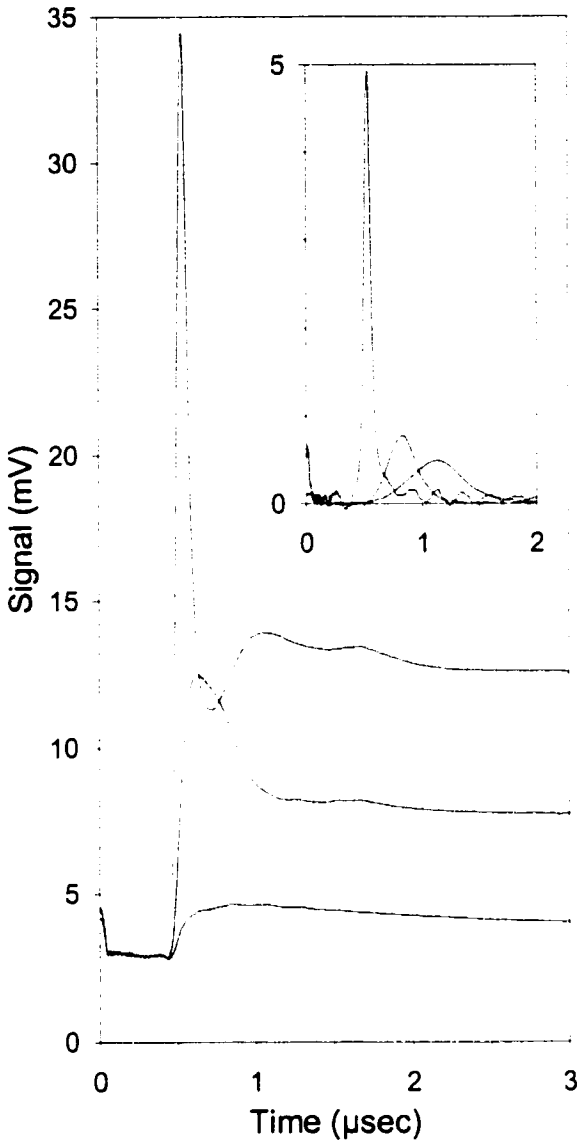

Fig. 69 Excitonic flux for collinear pulse and CW illumination of a 2.2 mm Cu_2O crystal as a function of temperature. The intensity of the pulse laser (λ = 532 nm) was $40I_o$, the CW laser (λ = 605.5 nm) was ~ 4 W/cm^2. The sample temperature was (from top): 2K, 4K and 6K. Inset: Traces from pulse illumination only for the above temperatures.

The qualitative agreement between the experimental results and the theoretical calculation lends credence to the interpretation put forward in the previous section: The plateau signal is due to a stationary Bose-Einstein condensate (although the constituent

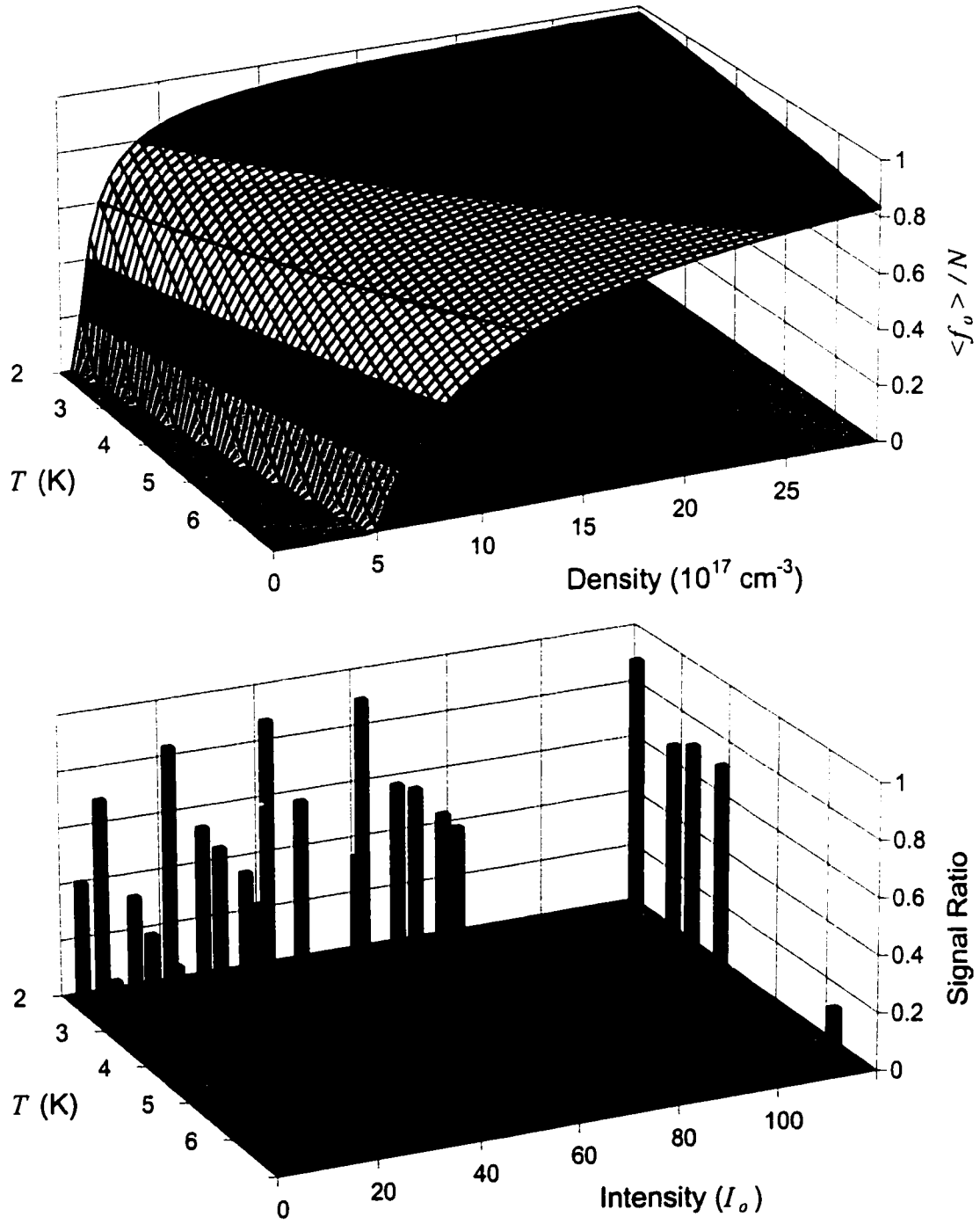

Fig. 70 a) Calculation of condensate fraction (top) and b) normalized plateau amplitude (bottom) as a function of temperature and exciton density (top) or pulse laser intensity (bottom). The data was obtained from collinear pulse (λ = 532 nm) and CW (λ = 605.5 nm) illumination of a 2.2 mm thick crystal with a CW intensity of ~ 4 W/cm^2.

excitons are moving at a velocity < v_o) for which the ratio of normal to condensed particles varies with the temperature. Due to the limited number of data points, the small temperature range and experimental difficulties we cannot say for certain that the drop of the signal exactly follows Eq. (15). However the direction and magnitude of the change is approximately correct.

3.4.5 Other Effects

At very high pulse and CW laser intensities we have recorded a modulation of the plateau signal. The largest modulation amplitude was obtained by using a pulsed dye laser at λ = 585 nm and a CW laser tuned to the orthoexciton quadrupole transition at λ = 609.7 nm. The traces shown in Fig. 71 were obtained under such conditions and clearly show that the modulations are periodic. The first two arrows on the left in the figure inset denote the arrival time at the detector of excitons traveling at the speed of sound (solid

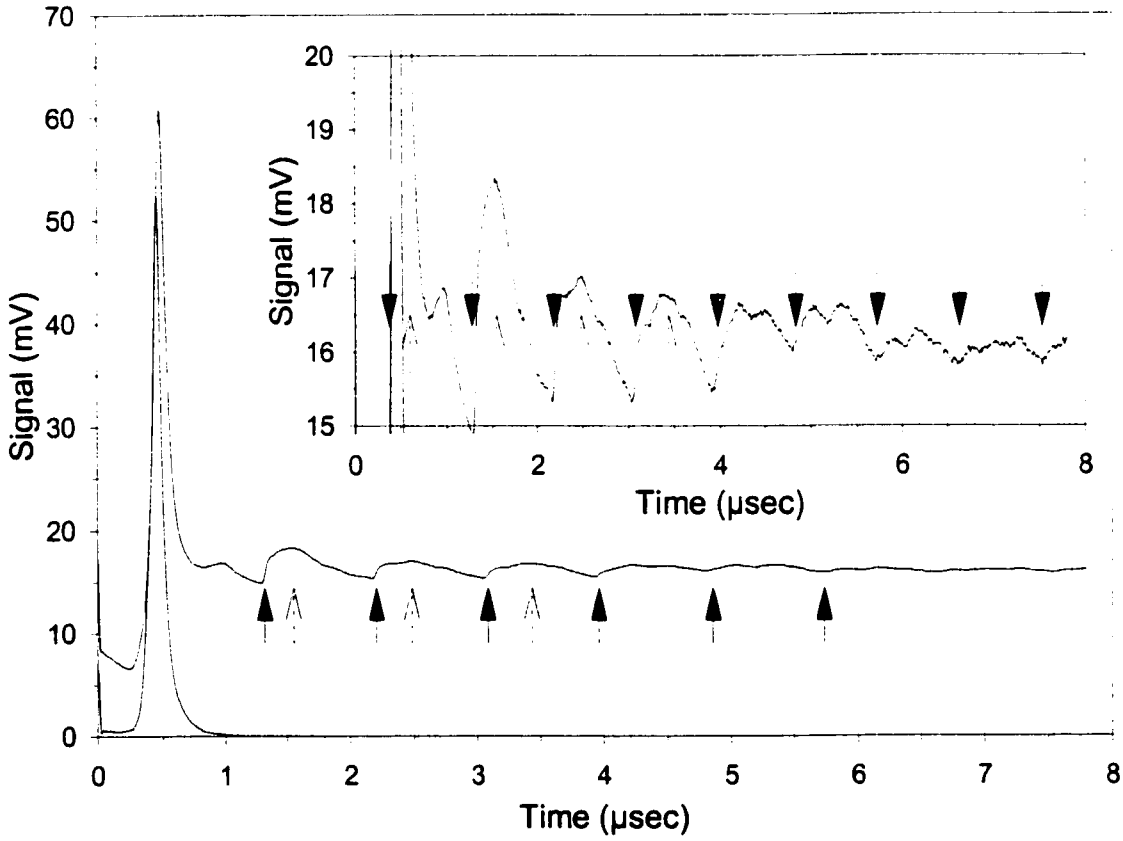

Fig. 71 Excitonic flux for collinear pulse and CW illumination of a 1.97 mm Cu_2O crystal at T = 2K. The intensity of the pulse laser (λ = 585 nm) was $150I_o$, the CW laser (λ = 609.7 nm) was ~ 6.5 W/cm^2. The vertical arrows denote the arrival times for $t = (2n + 1)\, d / v_s$ (solid line) and $t = (2n + 1)\, d / 0.88v_s$ (dotted line) where d is the crystal thickness, v_s is the velocity of sound and n is a positive integer. The inset is a close up of the traces.

arrow) or at the packet velocity ~ $0.88v_s$ (dotted arrow). The subsequent arrows correspond to a sharp increase of the plateau signal (solid arrows) or a peak superimposed on the plateau signal (dotted arrows). The periodicity of the solid arrows is related to the crystal thickness divided by the speed of sound times an odd integer number of transits. The dotted arrows follow the same series except the velocity is $0.88v_s$, the packet velocity.

We attribute the peak denoted by the dotted arrow to the arrival the condensate at the detector face after an odd number of transits. The amplitude of the packet seems to diminish exponentially. After nine transits the packet seems to cause a dip in the plateau signal, or one can view the structure as two separate peaks. The fairly sharp rise in the plateau signal denoted by the solid arrows is either due to excitons traveling at the speed of sound (due to stimulated emission), LA phonons influencing the detector by a piezoelectric effect [41], or both.

We note that the extremely large packet amplitude produced by the pulse laser alone is not amplified by the presence of the CW laser as was evident in earlier results with a λ = 532 nm pulse laser. We believe this is because the packet has reached the saturation point shown in Fig. 60 with the pulse laser alone. The moderate absorption coefficient at λ = 585 nm as compared to λ = 532 nm, and high pulse intensity causes a substantial number of excitons to be deposited in a low density cloud in front of the main exciton packet. The condensate, created in the high density volume close to the crystal face, travels through this cloud and is amplified, only in this case the cloud is created by the pulse laser itself. This "self amplification" may explain the discrepancy in the packet amplitude produced by equal intensity but different wavelength pulse lasers as discussed in Sec. 3.1.2.

3.5 Exciton Polariton Oscillations

In this section we report on an effect not directly related to Bose-Einstein condensation but nonetheless of considerable interest. As discussed in Sec. 1.3 the exciton dispersion crosses the photon dispersion curve and as a result a mixed mode can exist. Such a mode is called an exciton polariton, where a photon travels in the crystal and suddenly transforms into an exciton which may diffuse somewhat before returning to photon entity. This transformation may take place many times over in a single passage through the crystal.

Since the coupling of the photon and quadrupole exciton branches automatically leads to two quantum states, quantum beats may be observed in the propagation of the polariton. In addition since the polaritons can propagate over large distances observation of the beats is a sign of coherence over a macroscopic distance. The coherent propagation and quantum beats of quadrupole polaritons have been observed in Cu_2O [9] but for only

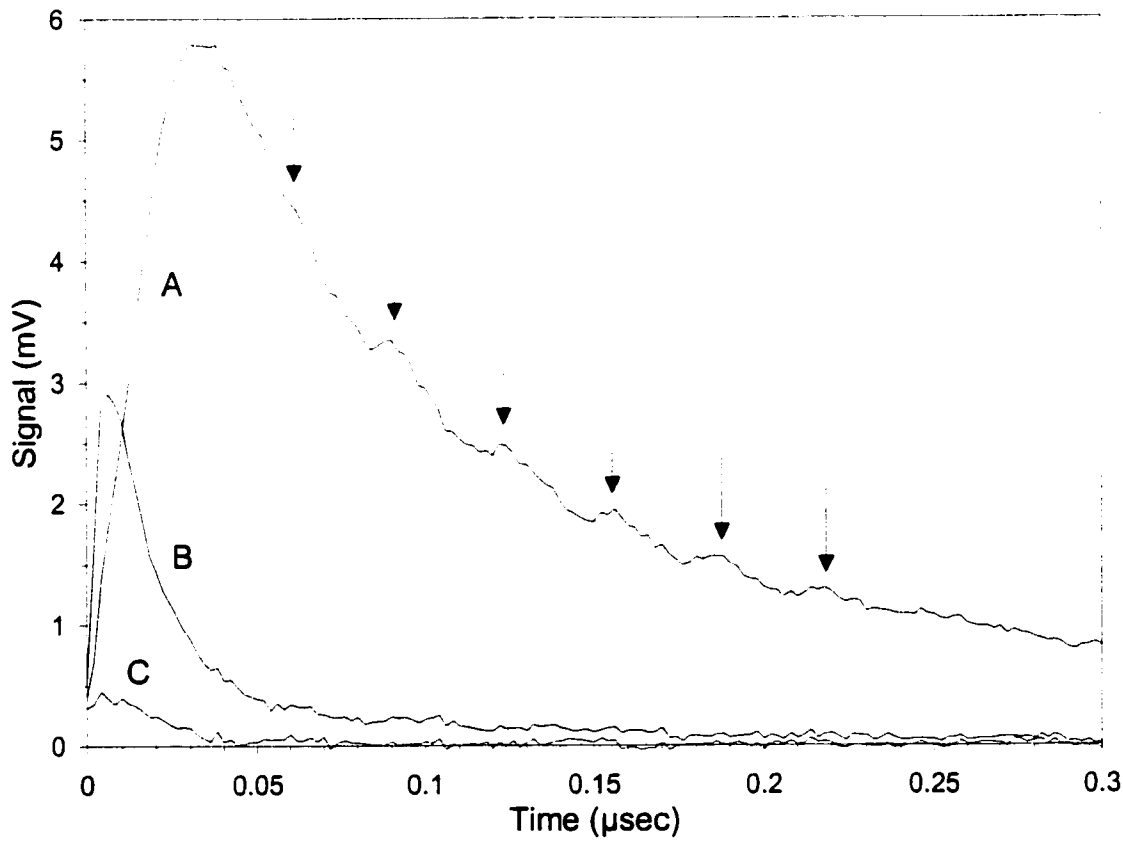

Fig. 72 Photon flux from scattered laser light impinging the electrode on a 1.97 mm Cu_2O crystal at T = 2K. For trace A the intensity of the pulse laser (λ = 532 nm) was $2I_o$, on the surface opposite the electrode. Traces B and C are for a pulse dye laser (λ = 609.76 nm and 609.7 nm respectively with line width of ~ 0.005 nm) impinging on a side surface with an intensity of $0.004I_o$.

a few nsec, we will offer evidence of exciton polariton quantum beats lasting ~200 nsec.

Figure 72 displays the time resolved signal generated by scattered light hitting the electrode on sample 1. Three cases are shown: Trace C is from the usual Nd:YAG laser at moderate intensity and displays nothing unusual, the signal follows the temporal profile of the laser intensity. Trace B is from a pulse dye laser striking the side sample surface (so as not to completely overwhelm the detector) tuned to a wavelength very near the orthoexciton quadrupole resonance; again the signal is not unusual considering the intensity and laser wavelength. The experimental configuration for trace A is identical to that of trace B except that the wavelength is precisely tuned to the n = 1 orthoexciton quadrupole resonance. The resulting signal is much different, the laser pulse has been broadened and small oscillations are now visible on the tail of the pulse.

The broadening of the pulse may be due to one of two reasons (or both). The injected photons create orthoexcitons which can recombine to emit photons which may not be reabsorbed before creating a free carriers at the electrode. The broadening is then possibly due to the inherent lifetime of the orthoexciton τ_{ortho} however τ_{ortho} is known to be at least an order of magnitude shorter than the width of the broadened pulse. Another explanation is given in [42] (and observed in [9]) where the authors predict a broadening and distortion of the laser pulse due to the propagation of the exciton polariton in a dispersive medium. Our results can not distinguish the two explanations because we do not have access to spectral data with our detector.

The small amplitude peaks on the tail of the laser pulse are believed to be exciton polariton oscillations of extremely long duration. The frequency of the modulation gives an energy difference between the two interfering states of ~ 0.13 μeV. This value is the same order of magnitude as the homogeneous line width of the quadrupole resonance (~ 0.65 μeV) [9, 43]. The oscillations we have observed are of much longer duration than previously measured and imply an extremely long coherence time for the exciton polariton. However the mechanism responsible for the long duration of the oscillations is unknown.

Conclusion

This thesis has described in detail the experimental apparatus and procedures used for the time resolved transport measurements of excitons in the semiconductor Cu_2O. From the analysis of the experimental results we have reported an unusual propagation regime for excitons in Cu_2O. Above a critical density and below a critical temperature the excitonic particles propagate together ballistically at nearly the speed of sound of the medium in the form of a stable packet over unusually large distances. The estimated particle density and temperature required for this effect to occur agree with the conditions required for a gas of bosons to undergo Bose-Einstein condensation. This behaviour reflects the motion of an excitonic superfluid which takes the form of a soliton with little spatial dispersion. The temperature behaviour of the packet is concordant with the theoretically predicted $T^{3/2}$ variation of the critical density, and the increase in packet size is also explained in terms of the condensed/normal particle fraction. In addition we have predicted and subsequently verified that a large number of the excitons initially in the packet are distributed throughout the crystal volume by the moving packet. From an analysis of results from the variable aperture experiments we have estimated the lateral size of the exciton condensate.

We have discussed the lateral and longitudinal interaction of exciton packets and have observed positive interference between two packets. The longitudinal interference experimental results were in agreement with our theoretical model which was solved numerically with the appropriate parameters. These observations reveal the coherent wavelike nature of the exciton packets which emerged from a random excitation source in accordance with the formation of a Bose-Einstein condensate.

We have also observed the stimulated emission of excitons (without participation of radiation). In our case the "matter laser" stems from the creation and/or amplification of an excitonic condensate by stimulated exciton scattering of a population of "cold" excitons generated by a secondary pulse laser or a CW laser. In addition we have also discovered that in the presence of an amplified packet and ample background exciton population, a stable stationary condensate is created. It takes the form of a filament following the path of the moving packet and linking two crystal faces. The collapse of the filament in some cases was found to be associated with the second arrival of the packet at

the detector face. The temperature dependence of the filament was found to conform to the Bose-Einstein model. The comparison of the amplification of the packet from a CW and a pulsed laser source and the calibration of the exciton flux in the filament both lead to two independent estimates of the paraexciton lifetime which were in agreement. The DC offset signal was attributed to the local exciton density in the detector vicinity due to its variation as a function of wavelength. From those results we have independently determined of the absorption coefficient in Cu_2O near the red edge.

Some anomalous effects were also reported such as multiple condensate reflections and very long duration exciton polariton oscillations.

We hope that the sum of this opus leads to an overall better understanding of Bose-Einstein condensation, matter wave interference and coherent energy transfer in solids.

References

1. K. Huang, *Statistical Mechanics*, Wiley, 1987.
2. G. M. Kavoulakis, G. Baym and J. P. Wolfe, Phys. Rev. B 53, 7227 (1996).
3. A. Mysyrowicz, D. Hulin and A. Antonetti, Phys. Rev. Lett. 43, 1123 (1979).
4. D. P. Trauernicht, J. P. Wolfe and A. Mysyrowicz, Phys. Rev. Lett. 52, 855 (1984).
5. D. P. Trauernicht, J. P. Wolfe and A. Mysyrowicz, Phys. Rev. B 33, 8506 (1986).
6. A. Compaan and H. Z. Cummins, Phys. Rev. B 6, 4753 (1972). N.B. The fitting parameters in Eq. (1) of this article are misprinted, they are actually 100 times larger than indicated.
7. Y. Petroff, P. Y. Yu and Y. R. Shen, Phys. Rev. B 12, 2488 (1975).
8. P. Y. Yu and Y. R. Shen, Phys. Rev. B 12, 1377 (1975).
9. D. Fröhlich, A. Kulik, B. Uebbing, A. Mysyrowicz, V. Langer, H. Stolz, and W. von der Osten, Phys. Rev. Lett. 67, 2343 (1991).
10. N. Peyghambarian, S. W. Koch and A. Mysyrowicz, Introduction to Semiconductor Optics, Prentice-Hall, 1993.
11. *Bose-Einstein Condensation*, Cambridge University Press, edited by A. Griffin, D. W. Snoke and S. Stringari, 1995.
12. N. Caswell, J. S. Weiner and P. Y. Yu, Solid State Commun. 40, 843 (1981).
13. D. W. Snoke, A. J. Shields and M. Cardona, Phys. Rev. B 45, 11693 (1992).
14. A. I. Bobrysheva and S. A. Moskalenko, Phys. Status Solidi B 119, 141 (1983).
15. F. Bassani and M. Rovere, Solid State Commun. 19, 887 (1976).
16. N. Peyghambarian, L. L. Chase and A. Mysyrowicz, Phys. Rev. B 27, 2325 (1983).
17. D. W. Snoke, J. P. Wolfe and A. Mysyrowicz, Phys. Rev. Lett. 64, 2543 (1990).
18. J. L. Lin and J. P. Wolfe, Phys. Rev. Lett. 71, 1222 (1993).
19. P. W. Baumeister, Phys. Rev. 121, 359 (1961).
20. I. Pasternyak, Soviet Phys. Solid State 1, 888 (1959).
21. *Handbook of Optical Constants of Solids II*, Acamedic Press, edited by Edward D. Palik, 1991.
22. V. Gregor, J. Chem. 66, 1645 (1962).
23. D. W. Snoke, J. P. Wolfe and A. Mysyrowicz, Phys. Rev. B 41, 11171 (1990).
24. I. Loutsenko, D. Roubtsov, Phys. Rev. Lett. 78, 3011 (1997).
25. E. Hanamura and H. Haug, Phys. Rep. C 33, 209 (1977).
26. A. Imamoglu, R. J. Ram, S. Pau, Y. Yamamoto, Phys. Rev. A 53, 4250 (1996).

27. K. Bennett and R. L. Byer, Appl. Opt. 19, 2408 (1980).

28. E. Tselepis, E. Fortin and A. Mysyrowicz, Phys. Rev. Lett. 59, 2107 (1987).

29. E. Fortin and W.M. Sears, Can. J. Phys. 60, 901 (1982).

30. L. C. Olsen and R.C. Bohara, Appl. Phys. Lett. 34, 47 (1979).

31. J. Bardeen, Phys. Rev. 71, 717 (1947).

32. A. A. Berezin and F. L. Weichman, Phys. Stat. Sol. A 71, 265 (1992).

33. L. C. Olsen, F. W. Addis, and W. Miller, Solar Cells, 7. 247, (1982-1983).

34. E. Bulatov and S. G. Tikhodeev, Phys. Rev. B 46, 15053 (1992).

35. E. Fortin, S. Fafard, A. Mysyrowicz, Phys. Rev. Lett. 70, 3951 (1993).

36. E. Benson, E. Fortin, A. Mysyrowicz, Phys. Stat. Sol. B 191, 345 (1995).

37. E. Benson, E. Fortin and A. Mysyrowicz, Solid State Commun. 101, 313 (1997).

38. M. Naraschewski, H. Wallis, A. Schenzle, J. I. Cirac, P. Zoller, Phys. Rev. A 54, 2185 (1996).

39. E. Hanamura, Solid State Comm. 91, 889 (1994).

40. A. Mysyrowicz, E. Fortin, E. Benson, S. Fafard and E. Hanamura, Solid State Commun. 92, 957 (1994).

41. A. Shields, S. Tamura and J. P. Wolfe, Phys. Rev. B 6, 4966 (1991).

42. A. Puri and J. L. Birman, Phys. Rev. A 27, 1044 (1983).

43. S. Kono, N. Naka, M. Hasuo, S. Saito, T. Suemoto and N. Nagasawa, Solid State Commun. 97, 455 (1996).